Dissertation
submitted to the
Combined Faculties for the Natural Sciences and for Mathematics
of the Ruperto-Carola University of Heidelberg, Germany
for the degree of Doctor of Natural Sciences

presented by

Diplom-Physikerin Julia Telsemeyer

Born in: Hamburg, Germany

Oral examination: July 4$^{\text{th}}$, 2012

Investigation of an Amorphous Silicon Flat-Panel Detector for Ion Radiography

Referees: Prof. Wolfgang Schlegel, PhD

Prof. Oliver Jäkel, PhD

Zusammenfassung

Der Gebrauch von Schwerionen in der Radiotherapie ermöglicht gezielt Tumore zu bestrahlen und gesundes Gewebe weitgehend zu schonen. Theoretisch besteht die Möglichkeit, die Besonderheiten der Wechselwirkung von Ionen mit Materie zur Bildgebung mit hohem Bildkontrast bei niedriger Dosis zu nutzen. Allerdings wurde der ideale Detektor für diese Art von Bildgebung noch nicht gefunden.

In dieser Arbeit wurde das Verhalten eines Flachbild-Detektors aus amorphem Silizium in der radiographischen und tomographischen Bildgebung mit Ionen untersucht.

Es konnte gezeigt werden, dass nach Anwendung einer entwickelten Bildkorrektur, der Weichteilgewebekontrast in den Ionen-Radiographien besser gegenüber konventionellen Photonen-Radiographien ist. Weiterhin wurde der Flachbild-Detektor zum Messen von wasseräquivalenten Dicken (WET) verwendet. Dafür wurde ein spezielles Verfahren entwickelt bei dem die Energien des Ionenstrahls variiert werden und somit eine Korrelation des Detektorsignals zur primären Energie der Teilchen zustande kommt. Diese Technik erlaubt eine Messgenauigkeit von 1.5 mm WET, was einer Verbesserung des klinischen Standards um einen Faktor 2 gleich kommt. Darüber hinaus wurde diese Messmethode zur Messung von wasseräquivalenten Weglängen (WEPL) durch Kohlenstoff-Computertomographie eingesetzt.

Auf Grund der relativ hohen Ionendosen, die zur Messung von WET- und WEPL-Verteilungen benötigt werden (Größenordnung: WET: 0.05 Gray, WEPL: 8 Gray), ist dieses Messprinzip, in der hier präsentierten Form, nicht für die Anwendung am Patienten geeignet.

Die in dieser Arbeit entwickelten Verfahren haben großes Potential zur Verifikation des Bestrahlungsplanungssystems, da zweidimensional berechnete Verteilungen von wasseräquivalenten Dicken und Weglängen mit hoher Genauigkeit gemessen werden können.

Abstract

Using heavy ions in radiotherapy offers a good potential for targeted radiation of tumors and the ability to spare healthy tissue. Their characteristic interaction with matter holds the potential to employ ions for high-contrast radiographic imaging at a decreased dose in comparison to conventional X-ray imaging; however, it lacks simple detectors suitable for this purpose.

In this study the performance of an amorphous silicon flat-panel detector, originally designed for photon imaging, was investigated for radiographic and tomographic imaging with ions.

After the application of a newly-developed image correction routine, the flat-panel detector is capable of ion-radiographic imaging with high soft-tissue contrast. Further, the flat-panel detector was exploited to measure the water equivalent thickness (WET) of phantoms. To do so, the ambiguous correlation of detector signal to particle energy was overcome by active carbon ion beam energy variation and measurement of the signal-to-energy correlation. Using this method has enabled the study to determine the WET of the imaged object with an accuracy better than 1.5 mm WET. It is an improvement by a factor of about 2 with respect to the standard clinical method. Finally, the study has shown the feasibility of this imaging technique for high-resolution carbon ion computed tomography and determination of water equivalent path length (WEPL) accordingly.

The developed imaging techniques present a method to measure the two-dimensional maps of WET and WEPL of complex phantoms with a simple and commercially available detector. The required doses in this configuration are too high (e.g. WET: 0.05 Gray, WEPL: 8 Gray) to be used for patient imaging, but this method presents a powerful tool to evaluate the performance of the treatment planning algorithm by studying range uncertainties.

Contents

1 Introduction

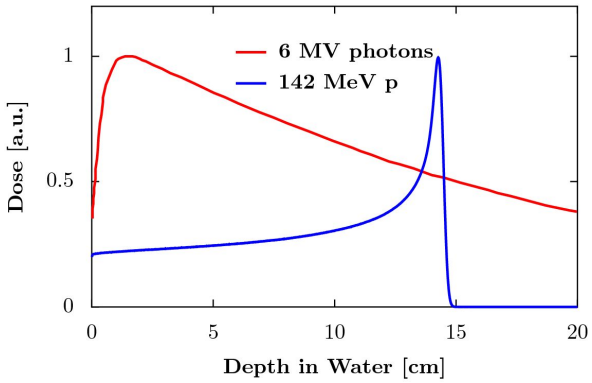

Figure 1.1: Depth-dose curve of a 6 MV photon beam in contrast to 142 MeV proton beam simulated with the Monte Carlo code FLUKA (courtesy of R. Herrmann).

The use of heavy ions in radiotherapy offers a potential for improving the protection of healthy tissue in comparison to conventional photon radiotherapy. This is due to the characteristic dose deposition of ions in matter described by the so-called Bragg curve: see figure 1.1. A low dose of radiation is deposited in the entrance region followed by a high-dose peak at the end of the ion range. The changing of ion energy positions the Bragg peaks in different depths in the target volume. A homogeneous dose coverage of the target is formed by superposition of monoenergetic Bragg peaks, called spread out Bragg peak (SOBP). The result is a highly conformal dose deposition with a characteristic narrow dose penumbra in contrast to photon irradiation. Thus, accurate prediction of the position of the Bragg peak is crucial as it has a direct influence on the treatment's outcome.

Presently, X-ray computed tomography (CT) images are used to extract quantitative anatomical data for the calculation of the ion dose distribution for heavy ion treatment planning. Due to the different nature of physical interactions of ions and photons with matter, there is no unambiguous relationship between the CT image information and the ions' energy loss. Therefore, the CT gray values are converted into ion stopping power with an empirically derived function. The currently used procedure (Schneider et al., 1996) provides accurate calculation of an ion's range in the order of 2-3 % only (Jäkel et al., 2001). Furthermore, metal implants (Jäkel, 2007) and changes in CT

protocols (Engelke, 2009) do introduce uncertainties in the beam range calculation of the treatment planning process.

The inherent high dose gradients, and thus high sensitivity of ion therapy to discrepancies between planned and delivered dose distributions, makes critical an accurate knowledge of the physical properties of matter such as ion stopping power. One proposed method to increase accuracy is to directly measure the ion stopping power by ion radiography.

In ion radiography, an image is formed either measuring the energy loss of the particles or the residual range of the ions in a detection system behind the imaged object. Imaging with ions has already been proposed in the mid 1940s (Wilson, 1946). In the 1970s, experimental ion radiographs showed image contrast superior to that of X-ray imaging at comparable doses (Sommer et al., 1978). However, facilities offering ion beams with sufficiently high energies were rare, and the development of two-dimensional digital detectors was just starting. The current availability of modern ion beam facilities and innovative detector technologies has made ion radiography technically feasible. Recent approaches to perform ion radiography and computed tomography include very complex and expensive detector designs that focus mainly on proton imaging (Sadrozinski et al., 2003; Ohno et al., 2004; Ryu et al., 2008; Muraishi et al., 2009; Amaldi et al., 2010; Rinaldi, 2012).

This study investigated the suitability of an amorphous silicon flat-panel detector for heavy ion radiographic and tomographic imaging. Since the beginning of this millennium, flat-panel detectors are commercially available and routinely used in clinical operations for photon imaging. Their compact size and weight makes them easy to handle, and they have been characterized extensively in regard to their behavior in photon beams (e.g. Partridge et al. (2002)). However, these detectors have not yet been used for radiographic imaging with ion beams.

2 Ion Radiography

Ion radiography refers to an imaging method in which an object is penetrated by highly energetic ions, with energies in the order of several 100 MeV/u (figure 2.1). A radiographic image is formed, when either the energy loss of the particles or the residual range of the ions can be measured in a detection system behind the imaged object.

Imaging with ions is very different from conventionally used X-rays. Unlike X-rays where attenuation is exponentially dependent on the object thickness, most ions traverse through the object constantly loosing energy. Further when measuring the energy loss of particles in a detection system, the steep gradient of the Bragg peak can result in higher contrast in comparison to the decreasing amount of energy lost by the photons, see figure 1.1. Therefore, the proposed advantages of imaging with ions over X-rays are:

- High soft tissue contrast and spatial resolution for diagnostic imaging at a low dose with a factor 50-100 smaller than a comparable X-ray radiograph (Schneider et al., 2004).
- Direct measurement of the water equivalent thickness of an object penetrated by particles for ion therapy treatment planning algorithm verification and improvement.
- Ion computed tomography as a basis for ion therapy treatment planning, eliminating the need for a conversion of conventional X-ray CT numbers to water equivalent path length.

2.1 Physical Background

Ion radiography is based on the passage of charged particles through matter. Unlike individual photons, ions gradually deposit energy in matter. Two interaction processes between ions and matter are of major importance: the collision of ions with atomic electrons and the scattering from atomic nuclei, which dominate the ions' energy loss and scattering, respectively. Other processes such as inelastic nuclear reactions play a role in the production of secondary particles. The production of Bremsstrahlung and Čerenkov radiation is negligible for dose deposition at therapeutic energies.

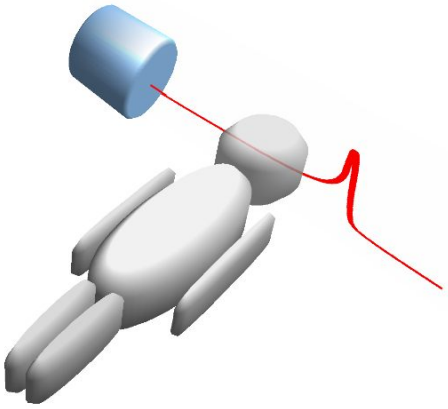

Figure 2.1: Schematic drawing of a patient ion radiography. High energies are used to irradiate through the patient. In the end either the residual range or residual energy of the particles are detected to form the radiograph.

2.1.1 Electronic Energy Loss

In the relevant therapeutic range of 1-400 MeV/u the ion energy is sufficiently high to excite or ionize atoms in the stopping medium. The mean energy loss of a charged particle in matter, also referred to as stopping power SP, is described by the Bethe theory (Bethe and Ashkin, 1953):

$$\mathrm{SP}(E) = -\frac{dE}{dx} = 4\pi \cdot r_\mathrm{e}^2 \cdot m_\mathrm{e}c^2 \cdot N_\mathrm{A} \cdot \frac{Z}{A} \cdot \frac{z^2}{\beta^2} \cdot \rho_\mathrm{e} \left[\ln\left(\frac{2\, m_\mathrm{e}c^2\beta^2}{I(1-\beta^2)} \right) - \beta^2 - \frac{C}{Z} - \frac{\delta}{2} \right], \quad (2.1)$$

where E is the particle kinetic energy, r_e the classical radius of the electron, $m_\mathrm{e}c^2$ the electron rest mass energy, N_A the Avogadro constant, Z and A the charge and atomic weight of the target atoms, z the particle charge, β the particle velocity, ρ_e the electron density and I the average excitation potential of the atoms of the medium.

The last two terms are the shell correction C and the density correction δ. These corrections become important at low and high energies, respectively. The shell correction takes into account that the electrons of the atomic shell are not stationary. It is important at velocities which are lower than the orbital velocity of the electron. For protons between 1-100 MeV it is at maximum 6 % (Ziegler, 1999). The density effect accounts for dielectric polarization of dense media and is of minor importance for therapeutic energies.

To calculate the stopping power for compound media, like tissue, Bragg's additivity rule (Bragg and Kleeman, 1905) is an important concept. It can be written in the form

$$\mathrm{SP}_\mathrm{media} = \sum_\nu n_\nu \, \mathrm{SP}_\nu, \quad (2.2)$$

where n_ν and S_ν are the mass fraction and stopping power of the atom species ν, respectively.

Dose

In radiation therapy, dose D is a macroscopic quantity describing the mean energy $d\bar{\varepsilon}$ imparted to matter of mass dm:

$$D = \frac{d\bar{\varepsilon}}{dm} \quad \left[\frac{\mathrm{J}}{\mathrm{kg}}, \mathrm{Gray}\right]. \tag{2.3}$$

However, for the same amount of dose the biological effect depends on the type of radiation, because of the variation of energy transfer mechanisms. The relative biological effectiveness (RBE) expresses the relative amount of dose of a radiation type R on biological tissue compared to the reference photon radiation ^{60}Co needed to cause the same effect:

$$\mathrm{RBE_R} = \left.\frac{D_{\mathrm{ref}}}{D_{\mathrm{R}}}\right|_{\mathrm{isoeffect}}. \tag{2.4}$$

The RBE can be determined experimentally in cell and small animal studies for special cell lines and irradiation types. These experiments are the basis for models used to predict clinically relevant RBEs. During the last decade a track-structure model was developed at the Helmholtzzentrum für Schwerionenforschung GmbH (GSI). The so-called Local Effect Model (LEM) predicts the RBE for different ions and cell lines starting from the corresponding experimental photon data and an amorphous track structure model (Elsaesser and Scholz, 2007). This model is implemented in treatment planning for carbon ion therapy at HIT.

Linear Energy Transfer

The linear energy transfer (LET) is a measure of ionization density on a microscopic level. For charged particles the restricted LET is given by:

$$\mathrm{LET}_\Delta = \frac{dE_\Delta}{dl} \quad \left[\frac{\mathrm{J}}{\mathrm{m}}, \frac{\mathrm{keV}}{\mu\mathrm{m}}\right]. \tag{2.5}$$

The LET_Δ is the energy transferred in a material volume around the particle track defined by the maximal energy transfer of secondary electrons dE_Δ. LET_∞ for $\Delta = \infty$ is equal to the electronic stopping power SP of the particles. Typically, LET is used to quantify the effects of ionizing radiation on biological specimens or electronic devices.

The energy loss of ions via collision with electrons leads to production of secondary electrons. The energy of these electrons determines the radius of the volume around the track, in which the energy is imparted to the medium. The energy Q that is transferred at a distance h from the particle trajectory can be written as (Tubiana et al., 1920):

$$Q = K\frac{1}{h^2} \cdot \frac{Z^2}{\nu^2}, \tag{2.6}$$

with ν being the speed and Z the charge of the particle. The energy transfer Q increases with the charge Z of the particles. At the same velocity higher charged particles transfer more energy to the medium. The energy loss of a carbon ion having an energy resulting in the same range in water as for a proton, is about 25 times larger than for protons.

Particle Range

The range of the ions in a particular material can be calculated by integrating the inverse of the stopping power over the energies ranging from the initial to the rest energy:

$$R_{\mathrm{CSDA}} = -\int_{E_{\mathrm{init}}}^{0} \left(\frac{dE}{dx}\right)^{-1} \mathrm{d}E. \tag{2.7}$$

This approach is called continuous slowing down approximation (CSDA). It approximates the mean range along the path when range straggling due to statistical fluctuation in the energy loss and particle scattering process can be neglected.

However, not all particles with an initial energy E_{init} will have the same range in matter due to statistical fluctuation in the energy loss process. The probability distribution of energy loss depends on the number of interactions. In case of a thick absorber (large number of collisions) the probability distribution for the energy loss Δ is Gaussian shaped (Leo, 1994):

$$f(\Delta) \propto \exp\left(\frac{-(\Delta - \overline{\Delta})^2}{2\sigma^2}\right), \tag{2.8}$$

with the mean energy loss $\overline{\Delta}$ and the standard deviation σ.

In an non-relativistic approximation, σ depends only on the penetrated path length R_0, the density ρ and Z/A of the traversed matter:

$$\sigma \propto \rho \cdot \frac{Z}{A} \cdot R_0. \tag{2.9}$$

This variance in the energy loss (energy straggling) causes a variance in the ion range (range straggling). To a first approximation, particle ranges are also distributed normally around a mean range.

Water Equivalent Pathlength

In heavy ion therapy treatment planning the scaling of particle ranges is used to account for inhomogeneities in the beam path. In this step the density information from the CT image is converted into a water equivalent range of the ions.

Computed tomography is based on photon attenuation over a range of energies in which multiple effects (Compton scattering, photoelectric effect) contribute to the beam

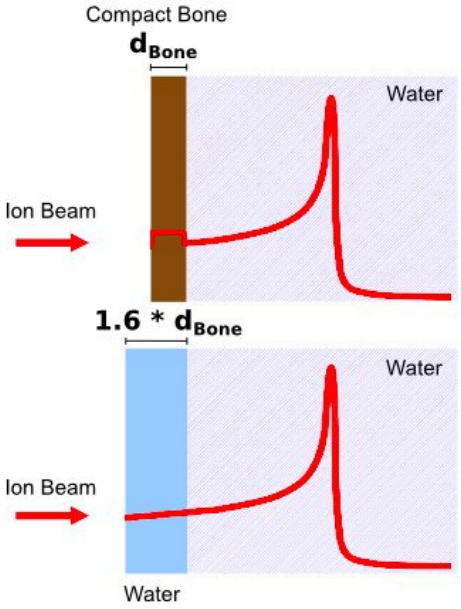

Figure 2.2: Schematic drawing of the WEPL concept. In terms of particle range a slab of compact bone with a thickness of d_{Bone} has the same impact as water with a thickness of $1.6 \times d_{\mathrm{Bone}}$ with 1.6 being the WEPL value for bone.

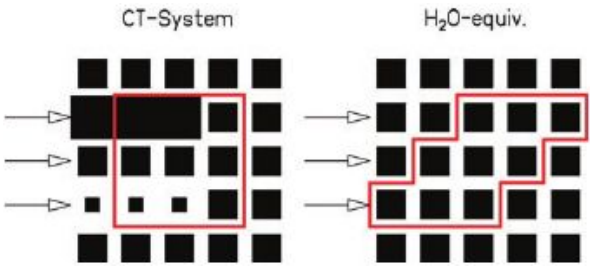

Figure 2.3: Transformation from the CT to a water-equivalent system (Krämer et al., 2000).

attenuation. The photoelectric effect has a strong dependence on the atomic number $Z^{3\text{-}4}$. Thus, if a significant amount of high Z elements is present the stopping power SP for heavy ions can only be determined indirectly from the CT numbers.

To account for this, the CT image information needs to be converted. Therefore, a code system dedicated to the planning of radiotherapy with energetic ions named treatment planning for particles (TRiP) was developed at GSI. It's basic idea to account for density variations in the beam path is to apply the concept of a water-equivalent path length (WEPL) when an ion traverses a CT voxel (Krämer et al., 2000). In this, the water equivalent path length scales the range of ions in a material to an equivalent range in water, see figure 2.2. High-density CT voxels correspond to ion path lengths larger than that for water, low-density voxels to shorter ion path lengths. This way the trajectory of an ion through tissue (visualized in the CT image) is transformed from the CT system into a water equivalent system (figure 2.3). In good approximation the

WEPL of a certain medium is given by:

$$\mathrm{WEPL} \propto \frac{\rho_{\mathrm{e}}^{\mathrm{medium}}}{\rho_{\mathrm{e}}^{\mathrm{water}}} \cdot \frac{\left[\ln\left(\frac{2\,m_{\mathrm{e}}c^2\beta^2}{I_{\mathrm{medium}}(1-\beta^2)}\right) - \beta^2\right]}{\left[\ln\left(\frac{2\,m_{\mathrm{e}}c^2\beta^2}{I_{\mathrm{water}}(1-\beta^2)}\right) - \beta^2\right]}. \tag{2.10}$$

For materials like tissue the mean ionization energies are comparable to water ($I_{\mathrm{medium}} \approx I_{\mathrm{water}}$). Further it was shown, that the relative stopping power to water $\frac{\mathrm{SP}_x}{\mathrm{SP}_{\mathrm{H_2O}}}$ is, to a good approximation, a constant which is independent of the nature of the charged particle and dependent primarily on the electron density (Tobias et al., 1980). This approximation is valid over the particle energy range of 10-1000 MeV/u (Köhler et al., 1965). This was confirmed by measurements of the WEPL value of muscle slabs, which showed an independence for carbon ions of energies greater then 50 MeV/u (Jacob, 1997). Thus, equation 2.10 can be written in the following form:

$$\mathrm{WEPL} = \frac{\overline{\mathrm{SP}}_{\mathrm{medium}}}{\overline{\mathrm{SP}}_{\mathrm{water}}}. \tag{2.11}$$

One proposed application of ion radiography is to validate treatment plans with direct measurements. The detector behind the irradiated object can only measure the energy loss of the particles, which is depending on the integrated stopping power along the beam path through the object. Therefore, the integrated stopping power along the beam path through the imaging object is measured and compared to the estimation of the treatment planning algorithm. This integrated stopping power is expressed in water equivalent thickness (WET) of the object. For any heterogeneous object dissected into volume elements (voxels), the WET is given by

$$\mathrm{WET}_{\mathrm{Object}} = \int_0^L \mathrm{WEPL}_{\mathrm{voxel}}\,\mathrm{d}l, \tag{2.12}$$

which is the thickness of a water body d_{water} that has the same effect on the particle range as the object (with thickness d_{object}).

2.1.2 Multiple Coulomb Scattering

When passing through matter, an ion experiences deflection caused by the Coulomb and hadronic field of the nucleus. These phenomena affect the quality of ion radiographic images in limiting the maximum spatial resolution.

The process of elastic scattering off the nuclei is called Coulomb scattering. Ignoring spin effects and screening, these collisions are individually governed by the Rutherford cross section:

$$\frac{\mathrm{d}\sigma}{\mathrm{d}\Omega} \propto \frac{Z_1^2 Z_2^2}{E^2} \cdot \frac{1}{\sin^4(\frac{\Theta}{2})}, \tag{2.13}$$

with Θ being the deflection angle, Z_1 and Z_2 the atomic number of the target and projectile and E the kinetic energy of the projectile. The cumulative effect of many scattering events in small-angle ($<30°$) approximation is more generally described by the multiple scattering theory of Molière (1947). For ions the scattering angles are small and the probability distribution is nearly Gaussian:

$$P(\Theta) \approx \frac{2\Theta}{\langle\Theta^2\rangle} \exp\left(\frac{-\Theta^2}{\langle 2\Theta^2\rangle}\right), \tag{2.14}$$

with the polar angle Θ and $\langle\Theta^2\rangle$ representing the mean square scattering angle. The width of the Gaussian distribution of scattering angles can be calculated in good approximation with the empirical formula of Highland (1975):

$$\langle\Theta\rangle = [20\,\mathrm{MeV/c}]\,\frac{Z}{p\beta}\sqrt{\frac{x}{L_{\mathrm{rad}}}}\left(1+\frac{1}{9}\log_{10}\left(\frac{x}{L_{\mathrm{rad}}}\right)\right), \tag{2.15}$$

with $\langle\Theta\rangle$ being the mean scattering angle, x the penetration depth, Z and p the projectile charge and momentum and L_{rad} the radiation length of the material. Due to the small scattering angles for ions, the projection of the angular deflection onto a perpendicular plane containing the incident trajectory, e.g. a detector, is still approximately Gaussian.

In this approximation, the ratio of scattering angles for protons and carbon ions with energies that result in the same range in water is:

$$\frac{\langle\Theta^2_{^{12}\mathrm{C}}\rangle}{\langle\Theta^2_{^{1}\mathrm{H}}\rangle} \approx \frac{1}{3}. \tag{2.16}$$

Therefore, it is preferable to carry out ion radiography with heavier particles like carbon ions since spatial resolution is improved due to less scattering of the particles in matter.

Another limiting factor for ion radiography resolution besides the particle scattering in matter is the distance between the imaging object and the detector device. Geometrical beam divergence in air leads to image distortion with blurred edges. Hence, air gaps in the imaging setup should be minimized to gain high resolution images.

Further, major deformations of the Bragg curve may occur due to object inhomogeneities perpendicular to the beam. In the absence of scattering, the penetration of particles through different material would only shift the Bragg peak by a distance equal to the integrated WEPL along its path, preserving the peak shape. However, multiple Coulomb scattering allows many different trajectories for particles with identical entry and exit points. This results in degradation of the Bragg peak and range uncertainties in presence of inhomogeneities. The shape of Bragg peaks behind geometrical phantoms has been measured for protons and heavy ions by Urie et al. (1986). Figure 2.4 shows an example for a neon radiograph of a patient's head. Three paths with increasingly complex and fine structures have been investigated (path A to C).

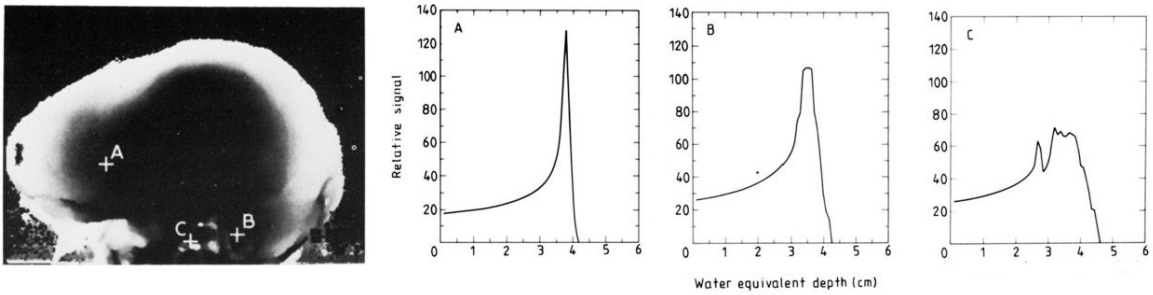

Figure 2.4: Neon radiograph of a patient's head. The depth-dose distributions were derived behind the respective anatomic points in the radiograph on the left (reprinted from Urie et al. (1986)).

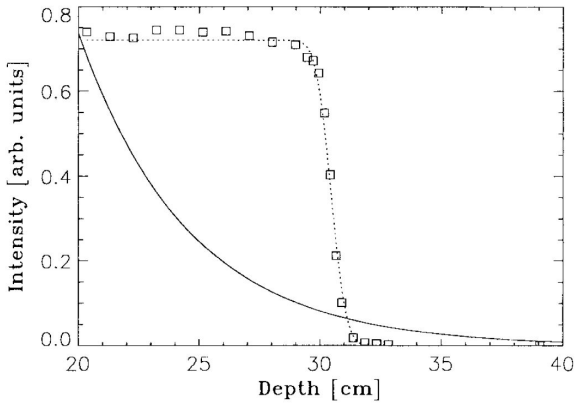

Figure 2.5: Measured intensity of 219 MeV protons (dotted line) and 50 keV photons (solid line) passing through water. Reprinted from Schneider and Pedroni (1995).

At path C the peak is degraded severely. This phenomenon of Bragg peak degradation due to multiple Coulomb scattering is not accounted for in currently used ion therapy treatment planning algorithms.

2.1.3 Inelastic Nuclear Interactions

The fluence of (primary) particles is reduced through inelastic nuclear reactions, in which secondary particles can be produced (figure 2.5). In the CSD approximation, the fluence of ions Φ at a depth x can be expressed as

$$\Phi(x) = \Phi_0 \exp(-\kappa x) \tag{2.17}$$

where κ is the total nonelastic macroscopic cross section for ions in a material. This cross section can be calculated with an empirical model as described in Tripathi et al. (1997) and Karg et al. (2010). The macroscopic reaction cross section for carbon ions of 250 MeV/u on water is $\kappa_{H_2O} = 0.047\,\mathrm{cm}^{-1}$. For example, the fluence of these particles in depth of 5 cm water reduces to 80 % and to 62 % in depth of 10 cm, respectively.

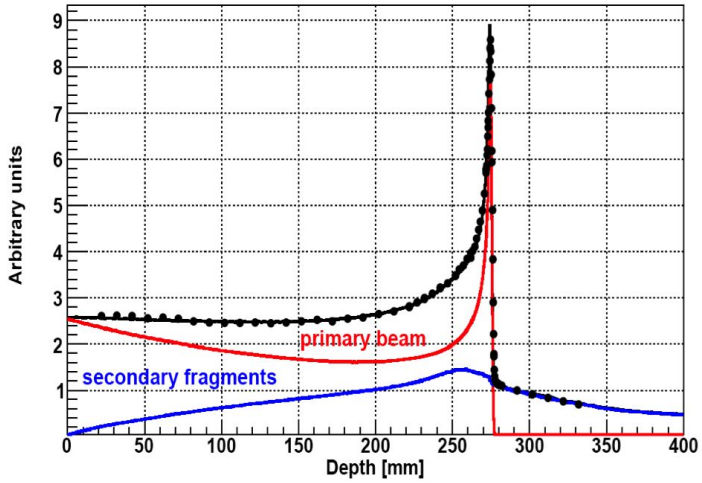

Figure 2.6: 400 MeV/u carbon ion depth dose curve in water. The solid lines represent the simulated contribution from primary ions and secondary fragments (Mairani, 2007), while the black dots correspond to experimental data (Haettner et al., 2006).

Primary particles can be broken apart into several daughter particles in collisions with target nuclei, a process referred to as ion fragmentation. The contribution of those light fragments to the total dose deposition increases with depth and is at maximum close to the Bragg peak, see figure 2.6. While primary particles come to the end of their range at the Bragg peak, some fragments have a greater range and lead to a dose deposition beyond the Bragg peak. This tail becomes more pronounced for heavier ions. The target nucleus may also break apart, but these fragments have relatively low energy and therefore a short range. The dose is generated by a complex mixed radiation field with secondary fragments like hydrogen, helium and boron.

Since inelastic nuclear reactions of heavier particles contribute to the depth dose distribution and the range of particles accordingly, particle range measurements by ion radiography are affected. The CSDA range of the charged particles in matter is then given to be the depth at which the maximum dose dropped to around 82 % of the maximum value beyond the Bragg peak (Bichsel et al., 2000).

2.2 Historical Review

First suggestion using ions for radiographic imaging dates back as far as the mid 40s (Wilson, 1946). More than twenty years later pioneering work was carried out at the Harvard University cyclotron where the idea of using protons for high contrast radiographic imaging was experimentally explored (Köhler, 1968). In the following years, proton radiography was further investigated and finally proposed as a diagnostic tool at the AAPM winter Meeting in November 1972 (Steward and Koehler, 1972). At the same time, proton tomography was discovered by a number of studies by Goitein

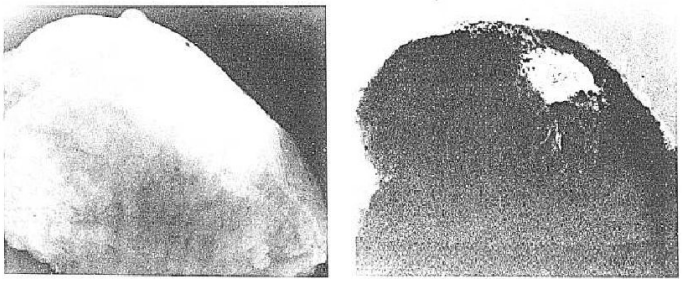

Figure 2.7: Left: Conventional X-ray radiograph. Right: Corresponding oxygen-ion radiograph (Sommer et al., 1978)

(1972); Crowe et al. (1975); Cormack and Koehler (1976). Exploring heavy ions for imaging, Sommer et al. (1978) carried out measurements at Lawrence Berkeley Laboratory. The substitution of protons by heavy ions significantly reduced image distortion caused by particle scattering. The obtained results showed that heavy-ion radiography is the supreme imaging modality for imaging of low contrast tumors at low radiation dose levels. Figure 2.7 illustrates how an infiltrating ductual carcinoma in a breast has considerably higher contrast in an oxygen radiograph than in a conventional X-ray radiograph.

Due to the scarcity of ion accelerators at the time and subsequent high costs, the development of radiographic imaging was not pursued at a fast pace. Rapidly, it was overtaken by the development of X-ray CT scanners for diagnostic imaging. The topic of imaging with ions totally disappeared from the scene until new developments in the 1990s led to an introduction of particle therapy in a number of treatment facilities around the world, where suitable beams were available. Furthermore, new detector systems were developed making charged particle measurements much easier. Soon, Schneider and Pedroni (1995) proposed to use proton radiography as a tool for quality control in proton therapy. Their work sparked revision and further development in ion radiography and tomography. Up to now, ion radiography and tomography research focuses mostly on protons, since heavy ions (e.g. carbon ions) continue to be scarcely available.

2.3 Recent Developments

Proton Radiography

Recent developments in proton radiography include Monte Carlo-based feasibility studies and investigations of suitable detector systems. Mumot et al. (2010) investigated the possibility of using a range probe for proton range verification in an extensive MC study. A low-dose, high-energy proton pencil beam is used to pass through the patient

and the integral Bragg peak was suggested to be measured at the exit side using a multi-layer detector. The obtained ranges can than be used to verify the ion beam treatment planning system. Based on this work, the concept of proton range verification with a range telescope and two position sensitive detectors in front and behind the imaging object was experimentally tested by Schneider et al. (2004) for a dog patient. Further, MC calculations were employed to investigate the feasibility of proton radiography with time-resolved proton range telescope measurements. This would allow to detect intrafractional and interfractional motions of lung tumor as presented in Han et al. (2011). Furthermore, a MC sensitivity study of proton radiography vs. kV and MV X-ray imaging was carried out recently (Depauw and Seco, 2011). Under the assumption of a perfect detector system, proton radiography was found to reveal excellent density resolution at poorer spatial resolution compared to photon radiography.

Proton Computed Tomography

Besides proton radiography, extended research in the last years was devoted to tomographic imaging with ions. Motivated by earlier studies by Goitein (1972); Koehler et al. (1975); Hanson et al. (1978) and Hanson et al. (1982), Zygmanski et al. (2000) investigated a detector system consisting of a intensifying screen viewed by a CCD camera for proton cone-beam computed tomography. A broad scattered proton beam was energy modulated to measure the WET in one orientation of an object. Shortly after publication, this technique was employed at HIMAC modified to suit heavy ion imaging (Abe et al., 2002). Further, the density resolution of proton computed tomography was investigated in 2005 by a Monte Carlo study (Schulte et al., 2005). It showed that reasonable density resolution can be achieved with a relatively small dose, which is comparable to or even lower than that of X-ray CT. Additional efforts in the field of ion tomography involve image reconstruction, which is especially important for light particle imaging since they undergo multiple Coulomb scattering. Iterative projection reconstruction algorithms for proton imaging are currently the preferred reconstruction method. However, more complex algorithms like the total variation superiorization schemes are suggested to further enhance image quality in proton computed tomography (Penfold et al., 2010).

Heavy Ion Computed Tomography

Over the last years several different approaches were tested for heavy-ion CT imaging at the heavy-ion medical accelerator in Chiba, Japan (HIMAC). Residual range distribution was measured with a film stack in combination to energy modulation with a range shifter (Nishimura et al., 1999). Based on this work and the achievements of Zygmanski et al. (2000), Abe et al. (2002) presented a heavy ion CT system consisting

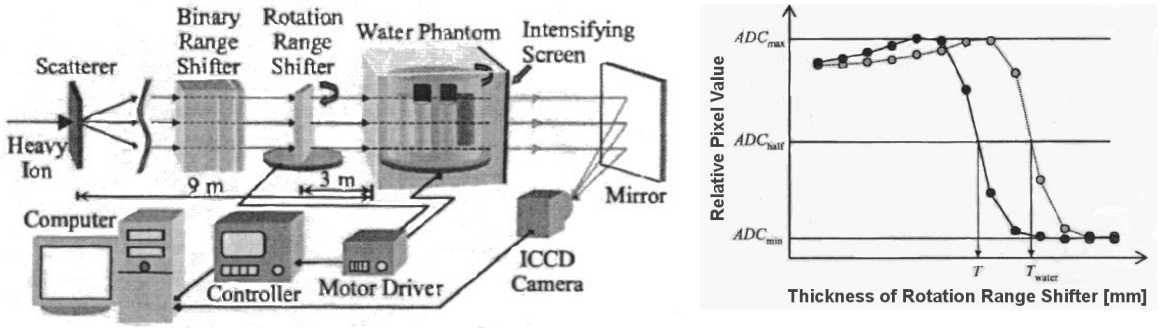

Figure 2.8: Left: Schematic view of the IonCT system as presented in Murashi et al. (2007). Left: two range shifter are used to modulate the energy of the carbon ion beam. The particle energy loss is measured with an intensifying screen viewed by a CCD camera. Right: Transition of the pixel values when changing the thickness of the rotation range shifter (reprinted from (Murashi et al., 2007)). The T value given by the thickness at 50 % of the maximum signal, can be correlated to a measured water equivalent thickness of the imaging object.

of an X-ray intensifying screen and a CCD video camera. Characterization of a more complex detector system based on two position sensitive detectors, an energy detector and two gate scintillators was carried out by Ohno et al. (2004). They obtained projection data not only for carbon ions but also for helium and neon ions. This detection system was also used to measure animal tissue samples in comparison to standard X-ray CT images (Shinoda et al., 2006). The obtained results were used to verify the accuracy of the conversion table from CT value to relative stopping powers as implemented in the treatment planning system. Meanwhile the heavy ion CT system based on the measurement of residual ranges (Abe et al., 2002) was improved by Murashi et al. (2007). The energy modulation was carried out by a binary and rotation range shifter, see figure 2.8 (left). This allows to measure the resulting detector signal depending on the energy of the primaries in a detector signal energy distribution similar to the shape of a Bragg curve. The amount of material in the range shifter needed to measure the maximal signal in the detector gives the residual range of the particles and water equivalent thickness of the object accordingly (figure 2.8 (right)). With high spatial resolution of the optical system, they were able to resolve rods with a diameter of 1 mm in the reconstructed images. As presented at the IEEE medical imaging meeting in 2011, they were furthermore able to achieve heavy-ion CT acquisition speeds of only 14 min per rotation (Murashi, 2011). In Heidelberg (Germany) Rinaldi (2012) investigated a heavy ion CT system based on parallel-plate ionization chamber stacks. The reconstruction of an anthropomorphic head phantom was strongly affect by noise, but it allowed to identify anatomical structures characteristic for a human head. Their future work will concentrate on improvement of the read out electronics and slight modification of the detection system to increase the resolution in the reconstructed images.

Despite the tremendous effort of the particle imaging community, until now, none of the ion radiography systems nor ion tomography systems have been applied to real patient imaging. One reason for this is the remaining issue of finding the optimal detection system, which allows high image quality at high speed acquisition and low imaging dose.

Detection Systems

Several different approaches in terms of detector technology are currently competing for ion imaging:

- silicon strip detectors, which measure the energy loss and position of individual particles (Sadrozinski et al., 2003),
- complementary metal oxide semiconductor (CMOS) active pixel sensors (Seco and Depauw, 2011), which measure the energy deposition of the particles in the active detector layer
- scintillating screens for proton (Ryu et al., 2008) and carbon ion radiography (Muraishi et al., 2009) viewed by CCD cameras,
- plastic scintillator in combination with a photomultiplier tube (Ohno et al., 2004) and even more complex systems like
- parallel-plate ionization chamber stacks together with multi-wire proportional chambers (MWPCs) for beam position information (Rinaldi, 2012),
- a combination of 4 XY planes of Si tracker and a CsI hodoscopic calorimeter (Sadrozinski et al., 2011) or
- scintillator slabs in combination with a position-sensitive detector (Amaldi et al., 2010).

The ideal detection system has high spatial resolution, a large sensitive area and high contrast. At the same time it should be efficient in terms of installation time, cost-effective and provide reliable, stable measurements. The conflicting requirements allow a wide variety of compromises, which is the reason why finding the optimal detection system is still an open issue.

3 Materials and Methods

3.1 Radiation Facilities

3.1.1 Heidelberg Ion-Beam Therapy Center

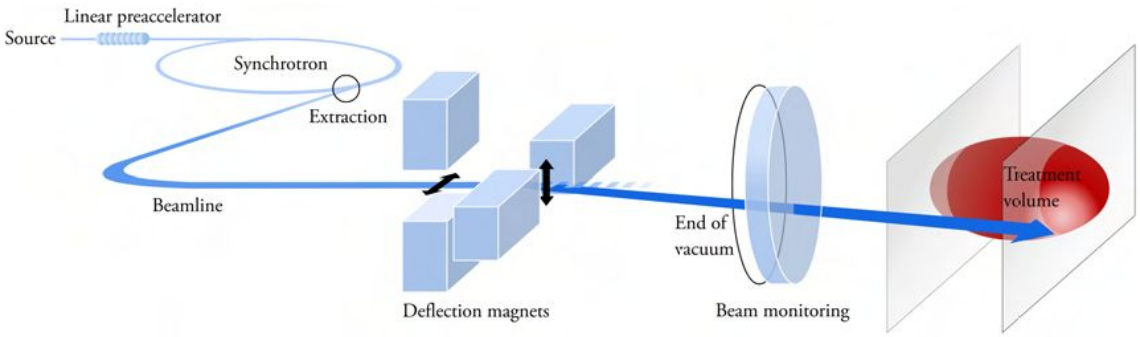

Figure 3.1: Schematic drawing of the beam production and application system at HIT from Huber (2011).

All reported measurements with ion beams have been carried out at the Heidelberg Ion-Beam Therapy Center (HIT) in Heidelberg, Germany. The hospital-based ion facility was built in 2005 and started its clinical operation in November 2009. The synchrotron installed at HIT is designed to accelerate charged particles ranging from protons up to oxygen ions. As of today, two ion sources are available for proton and carbon ion irradiation. The beam extracted from the sources is pre-accelerated in a linear accelerator before being injected into the synchrotron. In the synchrotron the ions are then accelerated to their final energy and extracted in "bunches" which are called spills. Each extraction spill with a maximum duration of 5 sec is followed by a break of roughly the same length used for acceleration of new particles. Particle ranges in water from 20-300 mm are provided in 255 energy steps. For proton and carbon ions these energy intervals correspond to energies of 48-221 MeV and 89-430 MeV/u, respectively (Haberer et al., 2004). Another distinctive feature of the facility is the beam delivery system. It allows conformal irradiation of the target volume by deflecting the beam laterally and vertically by perpendicular magnets. At the isocentre, which is defined as the beam focus, an area of $200 \times 200\,\mathrm{mm}^2$ can be covered. The pencil beam has, depending on the particle type and energy, a FWHM of 4-20 mm and is

approximately normally distributed in fluence and energy.

The features of the beam delivery system that are most important for particle radiography are the available energies, the energy spread and the angular divergence. The available energies at the HIT facility are sufficiently high to image structures with a water equivalent thickness of up to 30 cm. To reach high resolution in the radiographic images it is beneficial to have a beam with possibly small energy spread after the particles emerge from the beamline. The momentum in a single pulse at HIT is normally distributed with a momentum uncertainty dp/p at a FWHM of 0.1 % (Gross and Pavlovic, 1998). Most of the beams extracted from accelerators show, in addition to energy spread, angular convergence or divergence. It is desirable to minimize the non-uniformity in the direction of the particles. At the HIT accelerator, the optics are chosen to have dispersion and its derivative close to zero at the isocentre. In order to have "quasi-parallel" beam scanning, the scanner magnets are located at a distance of about 7 m upstream from the isocentre (Lazarev et al., 2011).

3.1.2 Photon Radiation Source

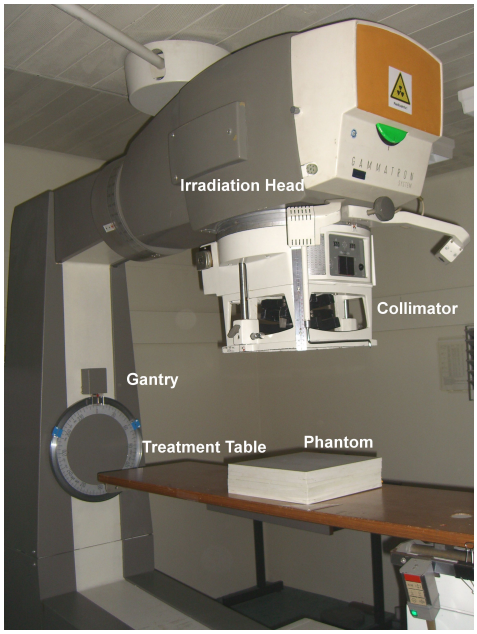

Figure 3.2: *Gammatron S unit* at the German Cancer Research Center, reprinted from Hartmann (2010).

The *Gammatron S teletherapie unit* (distributed by Siemens) at the German Cancer Research Center, formerly used for patient treatments, is a experimental photon source (figure 3.2). A synthetic radioactive isotope of cobalt, $^{60}_{27}$Co with a half life of 5.2 years is embedded in a irradiation head mounted on a gantry. The irradiation head shields the source to the outside. Upon irradiation request the head is mechanically opened.

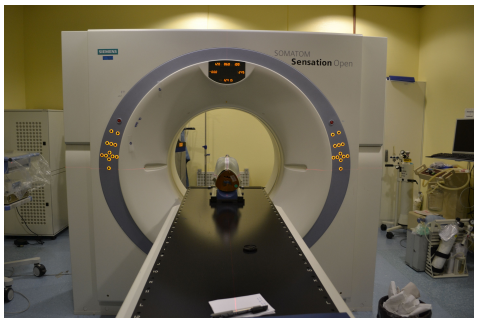

Figure 3.3: Picture of the *Siemens Somatom Sensation Open* CT Scanner at the Heidelberg University Hospital in Heidelberg. One of the imaging objects, an anthropomorphic phantom, is positioned on the table couch.

The cobalt decays to the stable ${}^{60}_{28}\mathrm{Ni}$ isotope in a two step process emitting two γ rays with energies of 1.17 and 1.33 MeV.

$$ {}^{60}_{27}\mathrm{Co}_{33} -> {}^{60}_{28}\mathrm{Ni}_{32} + e^{-} + \overline{\nu_e} $$

In the first step ${}^{60}\mathrm{Co}$ decays via a beta decay into activated nickel.

$$ {}^{60}_{28}\mathrm{Ni}_{32} -> {}^{60}_{28}\mathrm{Ni}_{32} + \gamma_1 + \gamma_2 $$

In the second step the activated nickel nucleus decays under emission of two gamma rays into stabile nickel.

3.2 Diagnostic Facilities

3.2.1 X-ray Computed Tomography

X-ray computed tomography (CT) is a medical imaging method that reconstructs three-dimensional images from large series of two-dimensional projections from all sides. The radiographic density of the images is proportional to the integral photon attenuation. After the three dimensional reconstruction, the photon linear attenuation coefficient μ is known for each voxel of the object. For practical reasons, the attenuation coefficients are transformed in CT values expressed in Hounsfield units (HU):

$$ \mathrm{CTvalue}_x = \frac{\mu_x - \mu_{\mathrm{H_2O}}}{\mu_{\mathrm{H_2O}} - \mu_{\mathrm{Air}}} \times 1000\ [\mathrm{HU}]. \tag{3.1} $$

By definition, the radiodensity of distilled water at standard temperature and pressure (STP) is defined as 0 HU, while the radiodensity of air at STP is defined as -1000 HU. Computed Tomography used for clinical diagnostics employs energies between 80 keV and 120 keV. The *Siemens Sensation Open* (figure 3.3), which is used as an imaging device for the heavy ion therapy at the Heidelberg University Hospital, is a 24 slice

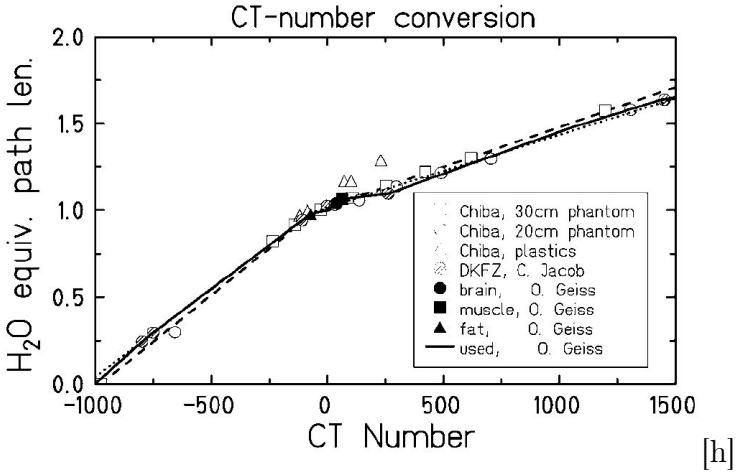

Figure 3.4: Empirical correlation between the CT numbers and the water-equivalent path length (Krämer et al., 2000).

spiral CT with a STRATON X-ray tube. It allows high resolution imaging with an isotropic spatial resolution up to 0.4 mm at a fast scan speed. Two protocols are available for the heavy ion therapy, one for body scans, the other one for head and neck imaging. Imaging was carried out with a resolution of 1 mm slice thickness and $0.605 \times 0.605\,\mathrm{mm}^2$ pixel resolution within the slice.

Table 3.1: Hounsfield look-up table currently in use at HIT for the Sensation Open head protocol.

CT value [HU]	WEPL
-1025	0.0001
-1000	0.001
-200	0.8
-116	0.94
-40	0.995
0	1.000
78	1.075
201	1.11
1584	1.7
1974	1.778
3096	2.077

In addition to the application of CT images for diagnostic purposes, CT images are used as well for treatment planning in heavy ion therapy. Therefore, the CT Hounsfield values are transformed into WEPL via a Hounsfield look-up table (HLUT). Presently, either an empirical approach or a stoichiometric calibration (Schneider et al., 1996) is used for setting up the calibration. The empirical approach is based on measuring the water equivalent path length of tissue or tissue equivalent material and their

Hounsfield values accordingly. The stoichiometric calibration relies on measurement of the Hounsfield values for specific materials with known chemical composition and calculation of their physical attenuation parameter. These parameter are used for calibration, which allows to calculate theoretical Hounsfield values for any material, e.g. tissue, with known chemical composition. A scatter plot of measured path length versus CT number, expressed in HU, reveals a piecewise linear relation at least for the tissue equivalent materials, see figure 3.4. Currently, at HIT a stoichiometric HLUT is implemented specific for the CT scanner and the used protocol, see table 3.1.

3.2.2 Mammographic Imaging Device

Figure 3.5: *Mammomat Inspiration* at the Heidelberg University Hospital.

Mammography uses low energy X-rays of around 30 kVp and compromises dose against soft tissue contrast. At these energies the photoelectric effect is dominant. The *Mammomat Inspiration* mammography unit (Siemens) installed at the Heidelberg University Hospital is a high-end digital mammography X-ray system launched in 2010 (figure 3.5). It is used for breast diagnostics, biopsy and follow-up imaging. An integrated amorphous selenium detector with a pixel size of $85 \times 85\,\mu m^2$ and a spatial resolution better than 5.8 lp/mm allows high resolution radiography. The system is optimized for good image quality at a comparable low dose in contrast to other state-of-the-art mammography systems. To improve spatial resolution anti-scatter grids are

used in addition to digital scatter corrections through signal deconvolution.

3.3 Flat-Panel Detectors

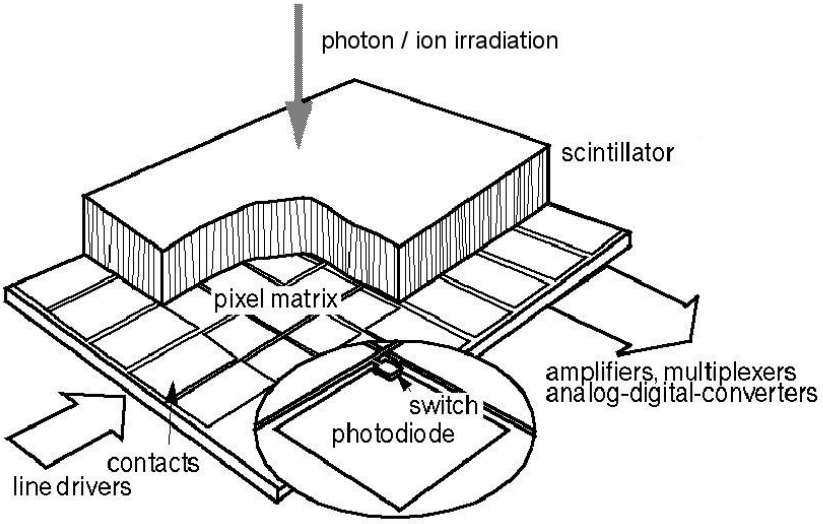

Figure 3.6: Indirect flat-panel detectors are composed of a scintillator and an a-Si:H photodiode array read out by TFT circuitry (original by Ewert (2002)).

A so-called flat-panel or electronic portal imaging device (EPID) is a digital detector consisting of a two-dimensional array of photodiodes and thin-film transistors (TFTs), all deposited on a single substrate. In indirect flat-panel devices, incoming radiation is converted to visible light in a scintillating foil that is installed on top of the pixel matrix.

The first flat-panel detector systems based on amorphous silicon (a-Si) were introduced in 1995. Two years later gadolinium-oxide sulfide scintillators were available and have been used for portable flat-panel detectors since 2001 (Körner et al., 2007). Today, flat-panel detectors are conventionally used in the clinical practice for X-ray digital imaging. The most obvious advantage of digital detectors in medicine is that they allow to substitute time consuming film measurements. In addition, they typically have greater contrast, increased dose efficiency and online read-out with digital image storage. Most of the flat-panel detectors are portable devices and resistant to mechanical stress. Due to their small size and weight of only several kilograms, they can be integrated into patient tables or mounted on gantries. The large active detector area makes the flat-panels suitable for most clinical applications.

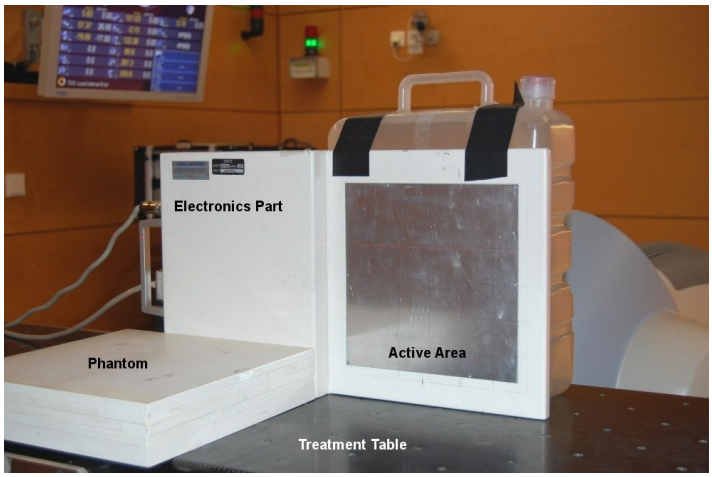

(a) Image of the detector positioned on the treatment couch.

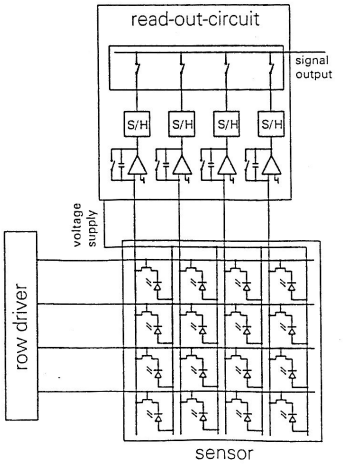

(b) Principle electronic arrangement of RID 256-L (Heimann, 1998).

Figure 3.7: RID256-L flat-panel detector distributed by PerkinElmer.

RID 256-L

The flat-panel detector investigated in this work is an indirect detection device, RID 256-L from PerkinElmer Optoelectronics GmbH & Co. KG (Wiesbaden, Germany), former EG&G Heimann, see figure 3.7. This model is fourteen years old and has been used for X-ray measurements as presented in Partridge et al. (2002). It is designed for kilo-and megavoltage portal imaging. The detector is based on a 512×512 p-i-n photodiode array with a pixel size of 400×400 µm^2, resulting in an active detector area of 204.8×204.8 mm^2. The diodes are binned 2×2 during readout leading to an effective pixel pitch of 800 µm with a capacitance of 34 pF. The scintillator consists of a Lanex Fast Back phosphor screen bonded to an amorphous silicon layer deposited on a glass substrate. In this indirect detection device the energy deposited in the scintillator by the impinging radiation is converted into visible light of around 550 nm wavelength. The emitted light is then, with very high efficiency, converted into electron-hole pairs in an array of a:Si-based photodiodes. The created electrical signal is then read-out by the thin-film transistor (TFT) pixel structure. The efficiency of the photodiodes response is made to match with the spectral output of the scintillator, giving a overall product efficiency for photon irradiation of around 55 to 65 % (Kuo, 2004). On top of the active detector layer, a cover of 0.6 mm aluminum is placed which operates as built-up material for photon beams and as shielding for scattered low energy photons (Partridge et al., 2002). Read-out is performed via a two 128-channel charge amplifiers and a 12 bit analog-to-digital converter (ADC). The read-out frequency can be adjusted to up to 12.5 Hz.

First measurements with the detector in ion beams have already been performed by Martišíková et al. (2011). They showed excellent signal linearity of the integrated signal as a function of beam intensity as long as the dynamic range was not exceeded by the signal. Further, no dose rate effects of the signal were observed. When irradiating the flat-panel detector with ions, the measured signal is a composition of indirect and direct detected irradiation. The ions traversing both layers produce scintillation in the scintillator as well as electron-hole pairs in the a-Si-based layer (direct signal). However, at the present stage it is not clear what part of the flat-panel detector signal originates from the scintillator and which part is due to the direct signal produced in the photodiode itself. This is investigated in section 4.1 by comparing experimental data to Monte Carlo simulations.

In the following, important characteristics of the flat-panel and applied methods are summarized. Effects under irradiation as well as image formation and spatial resolution are described and available experimental data on the characteristics of the flat-panel in ion and photon beams are presented.

Radiation Damage

The radiation hardness of a detector system is an important characteristic for its usability in clinical routine. The sensor part of the RID 256-L is physically separated from the electronics (figure 3.7) to minimize the damage by the radiation to the electronics. In addition, the electronics part of the housing is protected by a lead plate of 3 mm thickness contributing to a total weight of the flat-panel detector of around 8 kg. Total doses of $\sim 10^4$ Gy showed only minor performance changes in the combination of a-Si:H with a Lanex intensifying screen (Antonuk et al., 1990). For scintillators it is known that, they show high tolerances to large cumulative doses, but are susceptible to long-term changes in sensitivity due to effects of radiation. So far radiation damage of the RID 256-L due to ion irradiation has not been observed. The response was found to be stable within $\pm 0.1\,\%$ (Martišíková et al., 2011).

Signal Quenching

Signal Quenching refers to the underestimation of the particle energy loss in the active detector layer. It is a kind of intermolecular energy relaxation via non-radiative recombination between charge carriers due to i.e. lattice vibrations, heat, and impurity-related effects. Signal quenching increases with increasing ionization density along the particle track. It depends on the particle type and energy and is directly related to the LET of the particles, see section 2.1.1. Signal quenching has been observed for 132 MeV protons in the Bragg peak region in the order of 25 % (Martišíková, 2010), see figure 3.17. Heavier particles like carbon ions deposit locally larger amount of energy than

protons (section 2.1.1). Thus, quenching is expected to be higher in comparison to lighter particles. Since carbon ions are of major interest for ion radiography the signal quenching was investigated by measurement of a depth-response curve and comparison to a reference depth-dose curve, see section 5.1.2.

Signal Leakage

Within the TFT pixel structure of the detector a specific pixel line is read-out by applying a certain offset voltage as shown in figure 3.7 (right). All pixels in one line share the same read-out circuit, so that charges can "leak" to neighboring pixels.

Former measurements with the RID256-L showed that signal leakage in read-out direction is in the order of 0.1-0.2 % (Martišíková et al., 2012b) and similar for protons and carbon ions of all energies. Signal leakage is difficult to correct for, especially in scanned ion fields where single spots overlay in one signal detector image and thus time and position correlation of the irradiated geometry is complicated. Therefore, to minimize the influence of this effect on the measured radiographs, for all measurements the scan direction of the particle beam was chosen to be perpendicular to the read-out direction of the detector.

Dark Image

Photodiode and TFT dark currents, thermal noise from the preamplifier circuit, as well as the intrinsic offset applied to sensor read-out contribute to the dark signal, that varies from pixel to pixel. In photon imaging, the total offset is routinely eliminated by subtracting an averaged dark image. If the dark signal of the detector is stable, it is sufficient to acquire dark images just once, preferably shortly before a measurement. However, Partridge et al. (2002) report a drift in the amplifiers of the RID256-L read-out circuit. Since ion radiographic images are acquired over several minutes, this calls for an alternative correction method, which will be described in section 4.2.

Image Lag

Image lag may cause a reminiscent image after irradiation. It is a phenomenon that results from the release of a charge after the termination of irradiation. The charge that is trapped in the amorphous silicon matrix is then slowly released over time (Goldmann and Yester, 2004). Image lag is assumed to be proportional to the initial signal and is part of the physical signal (Partridge et al., 2002). Thus, to measure the complete signal the integrated detector images have to include several dark images after the irradiation where image lag is present. This is implemented as well in the new correction routine.

Temporary Pixel Specific Offset

A small fraction of pixels (ca. 0.1%) showed a very slowly decaying temporary offset after irradiation with ions. Lifetime of these pixel specific shift was variable and estimated to be of the order of 20-500 s, thus they are not assumed to be permanent radiation damage, but may introduce significant pixel artifacts in the final image (Huber, 2011).

Pixel Sensitivity

The sensitivity of a pixel to incident radiation is also subject to pixel-to-pixel variations, for example due to non-uniformities in the thickness of the scintillator or amorphous silicon layer. This non-uniformity can in principle be easily eliminated through a multiplicative sensitivity correction. Sensitivity corrections in photon imaging are based on average images of a uniform radiation field, the so-called flood field. However, this correction method is not feasible with scanned ion beams. The newly developed method is presented in section 4.2.

Image Formation

When recording scanned particle fields with a flat-panel detector, the image of the entire field is recorded in many frames. The final image is obtained by integrating the signal over all recorded frames:

$$I(\mathrm{i},\mathrm{j}) = \sum_{f=1}^{k} F_f(\mathrm{i},\mathrm{j}), \tag{3.2}$$

where $F_f(\mathrm{i},\mathrm{j})$ is the pixel value of an acquired frame at position (i,j), f is a successive nominator for the frame number, k is the total number of recorded frames and $I(\mathrm{i},\mathrm{j})$ describes the final image. After exposure and readout of the flat-panel signal, the raw imaging data is processed for display. Image processing is one of the key features of digital radiography with the potential to greatly influence the quality of the images.

Spatial Resolution

One of the parameters defining the quality of the images is the spatial resolution of the imaging system. The spatial resolution is typically quantified by the modulation transfer function (MTF) of the detection system and imaging modality, which describes the ratio of relative spatial resolution of the image to the object.

Various methods have been proposed to determine the pre-sampled MTF of digital radiographic systems, based on slit, edge, or bar pattern images (Fujita et al., 1992). Here the edge method is used.

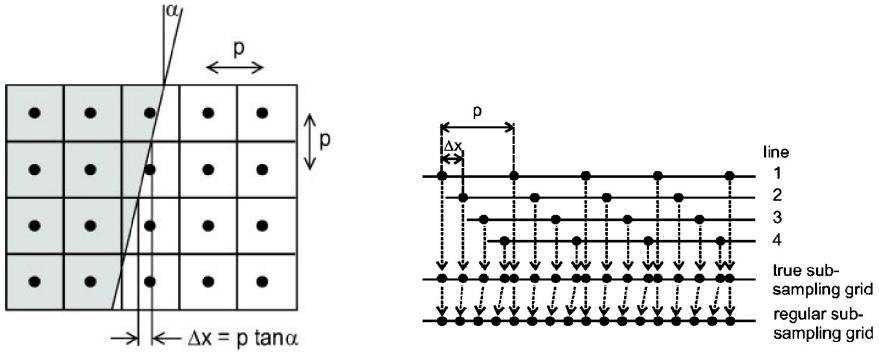

(a) Orientation of the edge to the detector pixel matrix.

(b) Outline of the construction of the oversampled ESF.

Figure 3.8: Schematic drawing of the tilted edge method (Buhr et al., 2003).

An edge is placed in front of the detector slightly tilted at an angle α with respect to the detector matrix (see figure 3.8 a)). The shift of the sampling position Δx is then given by

$$\Delta \mathrm{x} = \mathrm{p} \cdot \tan \alpha, \tag{3.3}$$

with p being the detector pixel spacing. From the digital edge image a composite, oversampled edge spread function (ESF) is generated as depicted in figure 3.8 b). The ESF is then fitted by an analytical edge spread function model (Boone and Seibert, 1994):

$$\mathrm{ESF}(x) = \begin{array}{ll} \text{if } x \geq 0; & \mathrm{ESF}(x) = \mathrm{ESF}^{\dagger}(x) \\ \text{if } x < 0; & \mathrm{ESF}(x) = -\mathrm{ESF}^{\dagger}(x) \end{array} \tag{3.4}$$

with

$$\mathrm{ESF}^{\dagger}(x) = a\{1 - \exp(-b\,|x - x_0|)\} + c \cdot \mathrm{erf}(d^{\frac{1}{2}}\,|x - x_0|). \tag{3.5}$$

Equation 3.4 defines a sigmoidal-shaped function that is useful for fitting the edge spread function commonly found in radiological applications and has in this work proven to be well describing for ion beam flat-panel measurements. In the next step, the obtained ESF function is differentiated to obtain the line spread function (LSF):

$$\mathrm{LSF} = \frac{d}{dx}\mathrm{ESF}(x). \tag{3.6}$$

Finally, the MTF is calculated by a Fourier transform of the LSF:

$$\mathrm{MTF} = \mathfrak{F}[\mathrm{LSF}]. \tag{3.7}$$

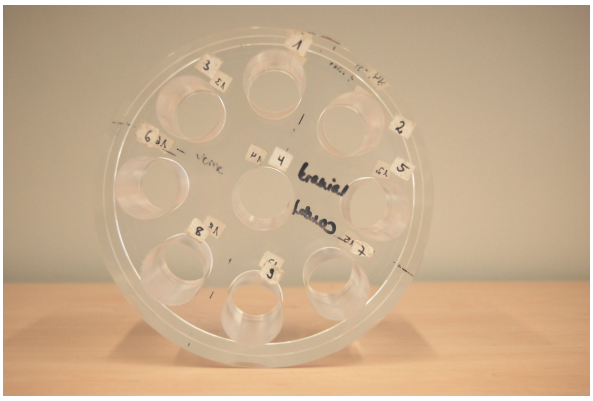

Figure 3.9: Image of the *PMMA head phantom* with a physical dimension of 16.0 cm in diameter and 10.0 cm depth with 9 bore holes for Gammex tissue equivalent rods.

3.4 Imaged Objects

Two different types of imaging objects, geometrical phantoms and biological samples were used for the experiments and are described in the following section. The phantoms differ in compositions ranging from tissue equivalent materials to biological samples. Tissue equivalent materials were used with simple defined geometry and patient replica. The biological samples were chosen to give realistic tissue contrast on the one side and patient like complexity on the other side.

3.4.1 Geometrical Phantoms

In radiation therapy polymethylmethacrylate (PMMA) is widely used as water substitute. Two different PMMA phantoms were investigated. A *PMMA head phantom* routinely deployed in quality assurance of CT scanners for conventional radiation therapy (figure 3.9) and a 1 cm thick *PMMA rack* to allow geometrical arrangement of the *tissue equivalent inserts* (figure 3.10).

Two different Gammex sets with 13 tissue equivalent rods each (figure 3.11) with a diameter of 28.45 mm and a length of 56.00 mm and slabs with a thickness of 10.00 mm, are available to be placed inside the phantoms. Each batch has slightly different chemical compositions and thus physical characteristic in ion beams. For one batch the WEPL values are given in table 3.2.

The arrangement of the Gammex inserts in the PMMA head phantom and rack is part of the experimental setup, see section 4.3.2.

The Rando Average-Man phantom, marketed by Alderson Research Laboratories, USA (figure 3.12), is specifically designed to simulate the human body during dose measurements involving therapeutic photon beams. The investigated *anthropomorphic head phantom* was fabricated in one piece and contains human skeleton and synthetic isocyanate rubber with similar properties to soft tissues (Alderson et al., 1962).

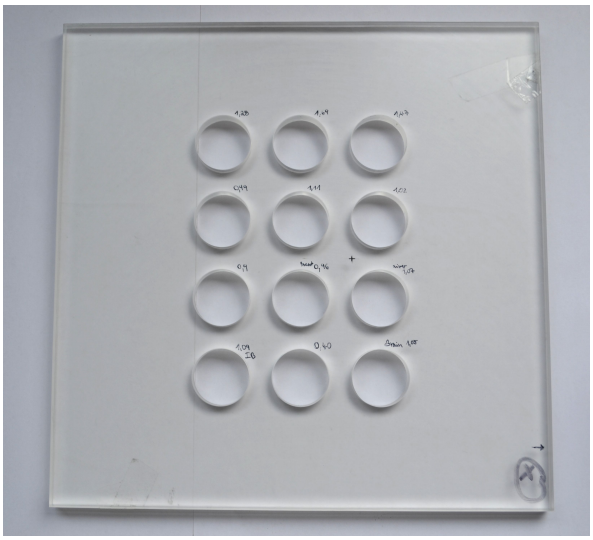

Figure 3.10: *PMMA rack* with 12 bore holes designed to hold Gammex tissue equivalent slabs of 1 cm thickness.

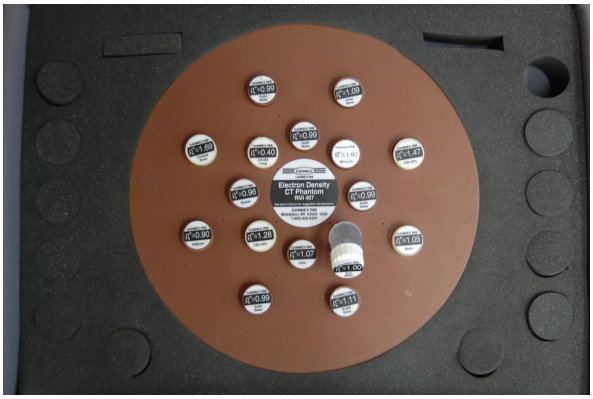

Figure 3.11: Image of the *Gammex Electron Density CT Phantom*, which consist of a Solid Water Disk (⌀16 cm) and 13 different rods out of various *tissue equivalent materials*. It is used to establish the relationship between electron density and the CT number of the materials in photon radiation therapy (Gammex, 2004).

Table 3.2: Water equivalent path length values, CT numbers and electron densities (Gammex, 2004) for various Gammex materials. The WEPL values were measured with carbon ions of 200 MeV/u at HIT (Ackermann et al., 2006). For the * marked value see Jäkel et al. (2001). The CT numbers were taken from CT calibration measurements carried out with Gammex *tissue-equivalent* rods placed in the PMMA head phantom. CT images were acquired with the standard CT head protocol used for ion beam therapy.

Material	WEPL	CT number [HU]	electron density [g/cm^3]
Adipose fat	0.943 ± 0.005	-118 ± 4.8	0.93
Breast	0.983 ± 0.005	-61 ± 4.8	0.97
Solid Water	1.001 ± 0.005	-8 ± 4.9	0.99
Brain	1.064 ± 0.007	5 ± 4.8	1.05
Muscle	1.033 ± 0.005	26 ± 5.9	1.02
Liver	1.073 ± 0.005	68 ± 5.1	1.06
Inner Bone	1.099 ± 0.005	269 ± 6.0	1.1
B200 Bone (Bone Mineral)	1.108 ± 0.005	270 ± 6.5	1.11
CB2 30%	1.263 ± 0.006	530 ± 6.3	1.28
CB2 50%	1.426 ± 0.006	961 ± 10.4	1.47
Cortical Bone	1.612 ± 0.006	1428 ± 15.1	1.7
PMMA	1.165 *	-	-

Figure 3.12: The *anthropomorphic head phantom* consists of a human skull surrounded and filled with tissue equivalent material.

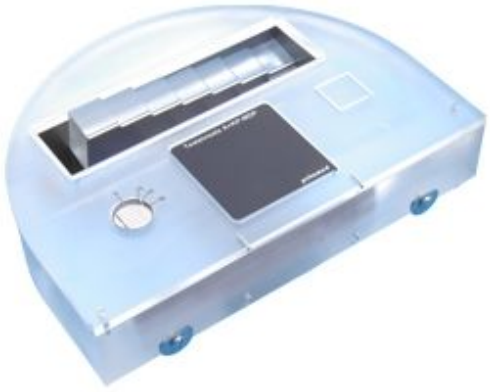

Figure 3.13: *PEHA med test phantom* for digital mammography (courtesy of DuMed).

Figure 3.14: Frozen knuckle of pork, shrink-wrapped.

Further, for digital mammography an image quality test phantom is deployed. The PAS 1054 fabricated by PEHA med (Sulzbach, Germany), consists mainly of 4 cm PMMA and an exchangeable test plate for acceptance and constancy tests. A gold-plated mammo detail test object was investigated.

3.4.2 Biological Samples

In order to measure real soft tissue objects, two biological samples were supplied and investigated; a frozen shrink-wrapped knuckle of pork and a frozen part of a pig head from former experiments at the German Cancer Research Center (DKFZ) (Huenemohr, 2011). The knuckle is composed of bony tissue with a surrounding tissue being a mixture of adipose and muscle flesh, see figure 3.14. The pig head on the other hand was chosen, because of its high complexity in geometry and tissue composition, see figure 3.15. It was cut through the saggital plane, which was ideal for alignment in front of the detector.

Figure 3.15: A frozen pig was cut in slabs and a triangular head piece. Only the head part has been investigated for the following experiments.

3.5 Data Evaluation and Simulations

The proposed water equivalent thickness measurement technique adapted to the flat-panel detector is presented in the following. Data analysis has been carried out with programs written in Matlab® (Version 7.10.0 R2010a). Further, the Monte Carlo code used for particle simulations is briefly discussed.

3.5.1 Ion Range Measurement Technique

The signal in a particular pixel of the flat-panel detector is depending on the particle type, the energy loss of the particles and the particle fluence rate. Single particle energy depositions cannot be calculated unambiguously from the measured signal. Other detection systems currently investigated for proton and heavy ion imaging (Zygmanski et al., 2000; Murashi et al., 2007) face the same difficulty. To correlate the signal to energy they use passive energy modulation via a range shifter (see section 2.3). In this work the active energy variation of the accelerator was exploited. Particle energy can be adjusted from irradiation spill to spill with high precision. While scanning with different carbon ion energies over the object, this method allows to correlate the measured signal S to the initial energy E_{init}. For each pixel of the detector a dependence of the signal on the initial beam energy is measured, see figure 3.16. The water equivalent thickness of the object is then given by the maximum signal $S_{\max}$ detected in each pixel, which corresponds to an energy $E_{\text{init,max}}$ at which the particles reach the end of range in the detector. Using the CSDA approximation (equation 2.7), the initial ion energy $E_{\text{init,max}}$ leads to a water equivalent thickness WET of the object given by:

$$\text{WET} = \int_0^{E_{\text{init,max}}} \left(\frac{dE}{dx}\right)^{-1}_{\text{water}} \mathrm{d}E. \tag{3.8}$$

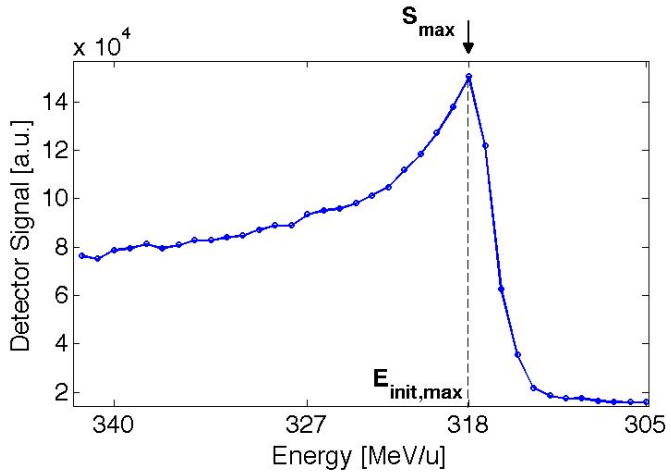

Figure 3.16: Water equivalent thickness evaluation. For each detector pixel a dependence of the signal on the beam energy is measured. The penetrated WET is determined by the water equivalent range corresponding to the peak maximum at $E_{\mathrm{init,max}}$.

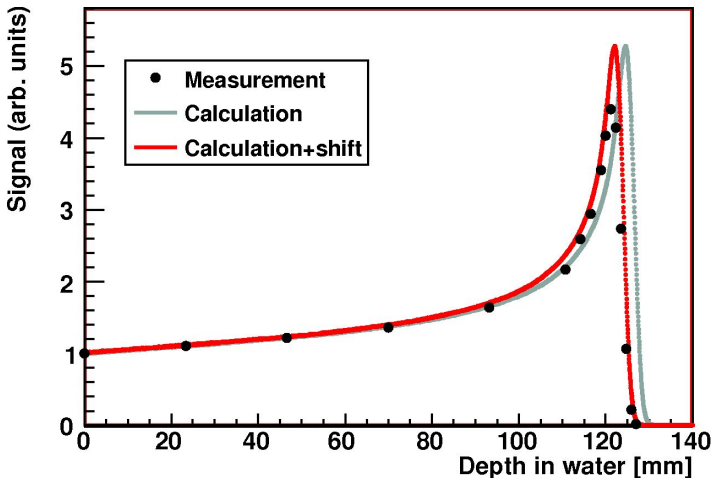

Figure 3.17: Determination of the flat-panel water equivalent thickness by Martišíková et al. (2012a) using protons (E=132 MeV). Monte Carlo simulations provided by K.Parodi and A.Mairani (HIT).

In order to measure absolute water equivalent thickness values, the WET of the flat-panel itself has to be taken into account. It was estimated by measuring a response curve in depth of PMMA (protons, E=132 MeV) with the flat-panel and comparison to Monte Carlo depth-dose simulations (Martišíková et al., 2012a). The shift of the simulated depth-dose curve to match the measurement determines the WET of the flat-panel, see figure 3.17. The water equivalent thickness of the flat-panel detector $\mathrm{WET}_{\mathrm{Flat-panel}}$ was found to be about 3 mm (Martišíková et al., 2012a) and is assumed to be valid for all energies and for carbon ion measurements. This $\mathrm{WET}_{\mathrm{Flat-panel}}$ value is then subtracted from the measured WET to calculate the final $\mathrm{WET}_{\mathrm{Object}}$. The

developed WET measurement technqiue is throughout this thesis referred to as *energy scanning* method.

Carbon Ion Computed Tomography

Tomographic imaging obtains cross-sectional images by reconstruction of a set of line integrals for multiple projection angles θ. In this work the proposed WET measurement technique of energy scanning, as described in the previous section, is employed for tomographic imaging. In ion tomographic imaging, the line integrals represent the integrated WEPL values of the materials along the particle trajectory, which is equivalent to the overall water-equivalent thickness of the imaging object WET. Generally the WET of an object at position r, on the projection at angle θ, is given by the line integral:

$$\mathrm{WET}(r,\theta) = \int_0^L \mathrm{WEPL}_{\mathrm{medium}}(x,y)\,\mathrm{d}l. \tag{3.9}$$

The value of r onto which the point (x, y) is projected at angle θ is given by:

$$x\cos\theta + y\sin\theta = r. \tag{3.10}$$

The equation above can then be rewritten as

$$\mathrm{WET}(r,\theta) = \mathfrak{R}(\mathrm{WEPL}) = \int_{-\infty}^{\infty}\int_{-\infty}^{\infty} \mathrm{WEPL}_{\mathrm{medium}}(x,y)\,\delta(x\cos\theta + y\sin\theta - r)\,\mathrm{d}x\,\mathrm{d}y. \tag{3.11}$$

This function is known as the two-dimensional *Radon transform* $\mathfrak{R}$.

In order to obtain tomographic images the data is reconstructed with the in X-ray imaging commonly used *filtered back projection* (Kalender, 2000). Before the data is backprojected for each projection the integral set is convolved with a filter. This is done by multiplication with the filter in the frequency domain. The filter is the inverse Fourier transform of the point spread function of the imaging system. Here a cropped ramp filter, called Ram-Lak filter, given in Matlab® was used. In the final step the convolved profiles are back projected along the original beam direction to yield the reconstructed tomographic images.

3.5.2 Monte Carlo Simulations

The Monte Carlo (MC) simulation code FLUKA (Battistoni et al., 2006) was used for all MC simulations in this work. It is a fully integrated particle physics package and can simulate with high accuracy the interaction and propagation of about 60 different particles (including photons, electrons and heavy ions) within matter. The first code

versions were originally used as a tool for designing shielding of high energy proton accelerators evolved under a CERN project in the 70s. Heavy ion transport, energy loss, effective charge and multiple scattering, was developed by Ferrari as early as 1998 (Ferrari et al., 2005). Increasing demand for interaction models of heavy ions led to the current version of *FLUKA 2011.2* which is equipped with a physical model describing interactions in the energy region typical for ion beam therapy with good accuracy (Sommerer et al., 2006).

3.6 Dose Optimization

Dose management is crucial in clinical imaging. Even small amounts of dose may lead to stochastic effects like radiation induced cancer. These stochastic effects of radiation occur randomly and their probability increases with higher exposure levels or with repetitive exposures to ionizing radiation. Therefore, the dose to the patient has to be minimized at all time.

Patient imaging with ion radiography would only be reasonable, if the dose can be as low or lower than for the conventionally used imaging modality of X-ray CT imaging. Dose optimization for ion radiography is discussed in the following.

The total dose D deposited at a certain water equivalent depth z in the imaged object during ion radiography is given by the particle fluence ϕ_p and their mass stopping power $\mathrm{SP}_{E_{\mathrm{init}}}(z)/\rho$:

$$D(z) = \phi_p \frac{\mathrm{SP}_{E_{\mathrm{init}}}(z)}{\rho}. \tag{3.12}$$

Thus, optimization of dose can be achieved by decreasing the ion fluence ϕ_p at a cost of higher noise or by influencing the depth-dose distribution $\mathrm{SP}_{E_{\mathrm{init}}}$. The depth-dose distribution is strongly depending on the particle type and particle energy used for imaging. Heavier particles deposit more energy in comparison to lighter particles with the same range. On the other hand, as was discussed in section 2.1.2, heavier particles also have superior imaging qualities due to reduced Coulomb scattering.

High particle energies generally reduce the deposited dose in the imaging object. The energy can be chosen, so that the imaging object is placed only in the entrance region of the depth dose curve, avoiding the high dose region of the Bragg peak. This however requires a modification of the imaging setup. If the flat-panel detector is placed directly behind the imaging object the resulting images would be very low in contrast.

Therefore, in this work a *copper range shifter* in combination with the detector was investigated for dose optimization. This range shifter, placed between the imaging object and the detector, allows to measure the signal in the peak region, while the imaging object is placed in the low dose region.

The influence of a copper range shifter on spatial resolution of ion radiographs has

been discussed by Huber (2011) and was found to reduce particle scattering and improve spatial resolution in comparison to materials with lower density. Here, the copper range shifter was deployed for dose optimization in ion radiography. Further, dose optimization in terms of decreasing particle fluence was investigated.

4 Experiments

4.1 Characterization of the Detector Response

Prior to ion radiographic experiments, the detector response to ion irradiation was characterized. Some qualitative and quantitative characteristics have already been obtained in other studies, especially with respect to ion beam monitoring and ion beam quality assurance (Hartmann et al., 2012; Martišíková et al., 2011, 2012a,b), see section 3.3.

In this work, properties important for ion radiography were investigated. At first, measurements of the direct detector irradiation (free-in-air) (Martišíková et al., 2012a) were compared to MC simulations to understand the general detector signal formation. Then, signal quenching in depth was investigated for carbon ion irradiation. This is of major interest for ion radiography, because it can strongly effect the shape of the Bragg peak and thus the image contrast.

Study Free-in-Air

The signal of indirect detectors, as RID256L, to photon irradiation is dominantly coming from the scintillation layer. Only a small amount of X-rays directly generate a signal in the amorphous silicon. Thus, the detector response is strongly depending on the characteristics of the used scintillator. For imaging in ion beams the general signal composition of the flat-panel detector is so far unknown and thus studied in the following experiment.

In order to qualitatively understand the detector response to ion beams, Monte Carlo simulations were compared to detector measurements. Since the detector signal is depending on the particle species and the particle energy, measurements free-in-air with spot irradiation of carbon ions and protons of several initial energies ranging from the lowest to the highest available energy (Martišíková et al., 2012a) were used for comparison, as seen in table 4.1. The Monte Carlo code FLUKA was used to simulate the energy loss dE in the detector layers. The detector was modeled to be composed of 0.6 mm aluminum, an air gap of 2 mm, a Lanex Scintillator foil of 300 µm thickness and 1 µm hydrogenated amorphous silicon (a-Si:H), see figure 4.1. The scintillator was build of $Gd_2O_2S : Tb$ and a density of $4.48\,g/cm^3$ (Kim et al., 2006). For the amorphous silicon a density of $2.32\,g/cm^3$ and a hydrogen content of 10 % (Tao et al., 2003) was

Figure 4.1: Detector geometry and composition as used for Monte Carlo simulation.

assumed. The deposited energy was scored in the scintillator and a-Si:H as a function of different initial energies for protons and carbon ions, see table 4.1. The number of particles for the simulation was sufficiently high (protons: 5×10^6 primaries, carbon ions: 1×10^6 primaries) to limit statistical uncertainties.

Table 4.1: Initial particle energies used for measurements and Monte Carlo simulations.

Type	Initial Particle Energy [MeV/u]						MC transported Primaries
^{12}C	88	91	100	150	250	430	1×10^6
^{1}H	48	49	50	60	150	220	5×10^6

Study In Depth

Ion radiographs have the best image contrast, when the steep gradient of the Bragg peak can be exploited. Thus, signal quenching in the peak region can degrade image quality severely. In order to investigate this effect for carbon ions, a signal-depth curve in PMMA has been measured and compared to a calculated depth-dose curve.

The detector was positioned at the beam isocentre perpendicular to the beam. Increasing amounts of PMMA slabs were placed in front of the flat-panel to measure the signal depending on depth. The set-up was irradiated with a carbon ion beam of 300 MeV/u. For reference, a depth dose curve in water was calculated with the treatment planning code TRiP (Krämer et al., 2000), which was previously benchmarked with experimental data within the pilot-project of carbon ion beam therapy at GSI. To compare the experimental data to the model, the depth in PMMA was recalculated to the depth in water by multiplication with the water equivalent path length value of PMMA, see table 3.2.

4.2 Image Processing

After exposure and readout of the detector signal, the raw detector data is processed for improvement of the image quality. Offset and pixel sensitivity corrections are applied

routinely for photon imaging (Beutel, 2000). However due to the long image acquisition times and sequential irradiations, the special case of scanned ion field irradiation requires modification of the established methods. Therefore, the characteristics of dark images were evaluated in detail. Further, several pixel sensitivity correction methods were investigated in terms of accuracy.

Dark Image

Dark images consist of a fixed designed offset and a variable background noise formed by diodes and transistor non-idealities (Kasap and Rowlands, 2002). The dark image is measured with no beam being present and subtracted from the acquired image. Previous work suggests measuring dark images on a regular basis e.g. before image acquisition (Beutel, 2000). However in our case, radiographic imaging is based on a number of up to 9000 image frames in which minor differences in dark images can sum up to a significant image distortion. Therefore, intensive studies of the dark image change in time and its dependence on the detector region were investigated without irradiation or previous irradiation.

Pixel Sensitivity Correction

The sensitivity of pixels to incident radiation is not uniform for the whole detector due to non-uniformities in the thickness of the silicon or scintillation layers or imperfections in the read-out circuits. Since the response of the detector over the operating range is known to be linear the non-uniformity can be easily eliminated. This is done by multiplication of the offset-corrected pixel data with a sensitivity correction matrix. For each pixel a multiplicative correction factor has to be obtained. Sensitivity corrections in photon imaging are based on average image frames taken with a given radiation field, the so-called flood field (i.e. radiation field free-in-air) (Beutel, 2000). However, this radiation field is highly inhomogeneous and irreproducible due to distortion given by the design of the radiation unit like a linear accelerator. Thus, these beam profiles of the radiation field are present in the correction matrix and lead to, when applying it to a different radiation modality like ion irradiation, incorrect results of the sensitivity correction process. Therefore, several methods were investigated to implement a pixel sensitivity correction routine for ion beam irradiation as a special application.

In the case of ion beam irradiation, the sensitivity of the flat-panel should be measured independently of the irradiated field. Therefore, it is of crucial importance that the detector is irradiated with a very homogenous field to acquire the pixel-to-pixel variations of the detector represented in the sensitivity correction matrix. Unfortunately, the irradiation homogeneity at HIT for carbon ions with the standard settings for therapy is around $\pm 5\,\%$ and very irreproducible, which for this purpose is not suf-

ficient. Thus, the experimental determination of the sensitivity correction was carried out at a ^{60}Co irradiation unit, the Gammatron S. This unit at the German Cancer Research Center provides quadratic fields of different sizes with a defined geometry at a source-to-axis distance of 80 cm. The advantage of the Gammatron S is the highly reproducible irradiation field, so that the small present non-uniformities of the irradiation field due to the design of the ^{60}Co source and the used beam collimation can be corrected.

Three different approaches using the Gammatron S irradiation field were tested for the sensitivity correction of the detector. The first investigated method included dose-calibrated radiographic films (Kodak X-Omat V) and iron markers, which were used to register the detector signal to the film response and thus correct for the inhomogeneities. The draw back of this method was found to be the inhomogeneity of the film response (locally up to 10 %), which occurs due to the film fabrication and development process. Secondly, a mathematical iterative method by Donetti et al. (2006) was used to recalculate the response independent of the inhomogeneities in the field. The algorithm is based on a three-step irradiation procedure with constant delivered fluence at each step. After the first irradiation the detector is rotated by 90° and irradiated again. Then it is displaced laterally by a defined distance and irradiated for the final image. From the three images and known transformations the response of the single pixel independent of the radiation field can be calculated. This iterative method is very sensitive to slight imperfections in the setup (e.g. rotation, translation), especially when applying it to large detector matrixes and led to inaccurate results. The chosen developed method is called *small field patching method* and it is explained in detail in the following passage.

The distribution of the Gammatron S irradiation field was estimated by film measurements. This information was then used to select a small very homogeneous 2 x 2 cm^2 central area of the photon field. Multiple images of this central region have been acquired with the detector being displaced laterally between the images. In the end, by cutting out the central beam region (25 x 25 pixels) of each of the 100 images and patching them to simulate a large homogeneous field, a composite pixel sensitivity matrix was formed. A similar correction technique has been described by Greer (2005). To increase the detector signal a 5 mm thick RW3 plate was placed on top of the detector during ^{60}Co irradiation. The detector was shifted laterally with a pitch of 2 cm in-plane according to the scheme shown in figure 4.2 (right). To displace the detector with high accuracy in the horizontal plane, an in-house developed 3-axis motor driven gantry table system consisting of three combined linear tables and a controlling unit was used, see figure 4.2 (left). This system is remote-controlled and adjusts the detector position with submillimeter precision.

For each detector position, an average image over 1000 frames was acquired. This

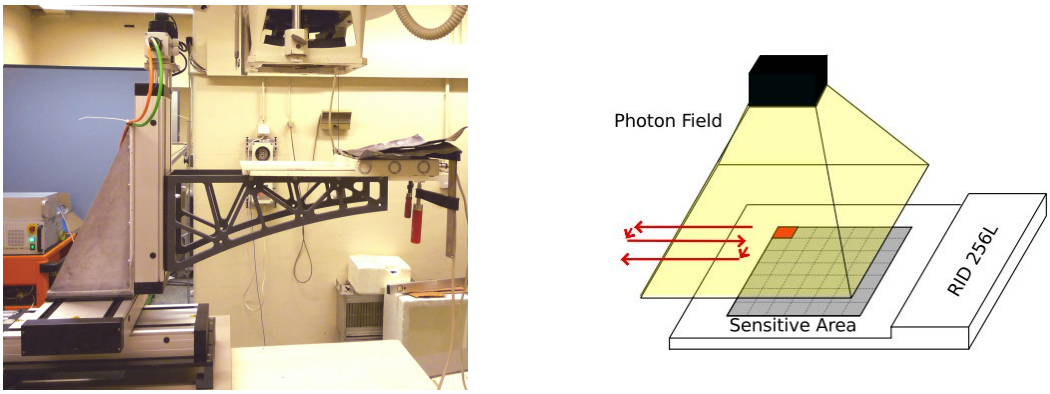

Figure 4.2: Left: Measurement setup at the Gammatron S. The detector is mounted on a 3-axis motor driven gantry table system below the ^{60}Co source. The detector electronics are shielded from the irradiation with lead. Right: Schematic displacement of the detector.

image was corrected with the dark image taken prior to irradiation. The obtained corrected Image $I_{\mathrm{corr-dark}}$ for the pixel with coordinats (i,j) was determined as

$$I_{\mathrm{corr-dark}}(\mathrm{i},\mathrm{j}) = \frac{\sum_{k=1}^{1000} I_k(\mathrm{i},\mathrm{j})}{1000} - d_{\mathrm{initial}}(\mathrm{i},\mathrm{j}) \ , \tag{4.1}$$

where I_k is the measured signal in that pixel and $d_{\mathrm{initial}}(\mathrm{i},\mathrm{j})$ is the dark image obtained before irradiation.

The pixel sensitivity correction matrix c is then formed by patching the central beam region of each of the 100 images $I_{\mathrm{corr-dark}}$ and normalization to the mean signal of the final pixel matrix.

In general, the flat-panel detector images I_{raw} are then corrected for pixel sensitivity by division with the correction matrix:

$$I_{\mathrm{corr}}(\mathrm{i},\mathrm{j}) = \frac{I_{\mathrm{raw}}(\mathrm{i},\mathrm{j})}{c(\mathrm{i},\mathrm{j})} \ . \tag{4.2}$$

4.3 Ion Radiographic Images

4.3.1 Spatial Resolution

After image processing as described in the previous section, the image quality in terms of spatial resolution is given by the pixel size of the detection system and the radiation quality. The spatial resolution refers to the minimum resolvable separation between two high-contrast objects. It is limited by the pixel size and is typically quantified by measuring the modulation transfer function (MTF) of the detector, see section 3.3. The MTF is a basic measure of the performance of an imaging system describing the signal transfer characteristics of the system as a function of spatial frequency (Williams, 1999).

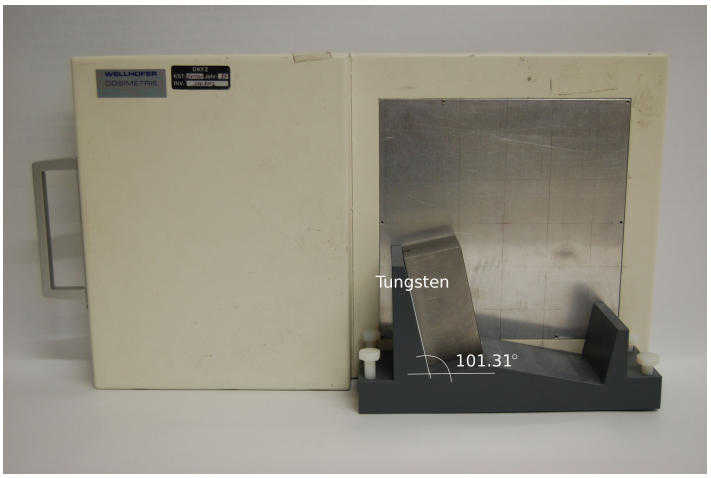

Figure 4.3: Tilted edge setup: the tungsten block is placed directly in front of the detector tilted against the detector pixel matrix.

Table 4.2: Irradiation settings for MTF measurements at HIT.

Particle Type	Energy [MeV/u]	Fluence (Particles/mm^2)
^1H	48.12	49.96×10^4
^{12}C	88.83	6.25×10^4

To investigate the potential of the detector for ion imaging, the MTFs for protons, carbon ions and photons were measured and compared. All MTFs have been calculated with an analytical edge spread function model, see equation 3.4. For this purpose a workshop built setup has been used consisting of a plastic fixture with two slopes at an angle of 11.31° and 101.31° relative to the pixel matrix. A tungsten block $5 \times 5 \times 10\,\mathrm{cm}^3$ used as an absorber was placed on the rack forming two very sharp edges to be radiographed, see figure 4.3. Ion radiographic measurements were compared to photon reference measurements at the Gammatron S ^{60}Co source (source-detector distance: 800 mm, field size at the detector surface: $200 \times 200\,\mathrm{mm}^2$). The signal of the photon field has been averaged over 50 frames with an exposure of 1.6 s each. The image correction was performed by a simple dark image correction and the developed sensitivity correction.

4.3.2 Soft Tissue Contrast

The proposed diagnostic information of ion radiographs motivated the following study on soft tissue contrast. Qualitative and quantitative measurements were carried out with a biological sample and a tissue equivalent phantom.

Figure 4.4: The frozen knuckle was placed directly in front of the detector and irradiated with protons and carbon ions of different energies. A Kodak X-Omat film was placed in between for reference measurement. In the back a water filled container was used for fixation.

Table 4.3: Irradiation settings for qualitative soft tissue measurements of a biological sample.

Particle Type	Energy [MeV/u]	Fluence (Particles/mm^2)
^{1}H	136	31.26×10^5
	143	31.36×10^5
^{12}C	250	1.11×10^5
	430	1.11×10^5

Qualitative Contrast

The first approach to show the usability of the a-Si:H detector for ion radiography of biological samples was to image a frozen knuckle of pork with proton and carbon ions of different energies. The knuckle contained both bony and soft tissues. In advance, X-ray CT images of the knuckle were taken to estimate the water equivalent thickness. In this way, the necessary energy of ions to pass through the object resulting in high contrast was estimated. For this purpose, the CT Hounsfield values were transferred into WEPL values with the HLUT currently in use at HIT and integrated along the beam path to yield WET. Ion radiographic images were obtained, irradiating the frozen shrink-wrapped knuckle with the parameters given in table 4.3. The response behind the object has been measured with the flat-panel detector as shown in figure 4.4.

Quantitative Contrast

In order to measure the soft tissue contrast of ion radiographs quantitatively, phantom measurements were carried out. The phantom consisted of 12 different soft tissue equivalent rods ranging from lung to bone placed in the PMMA rack as depicted in

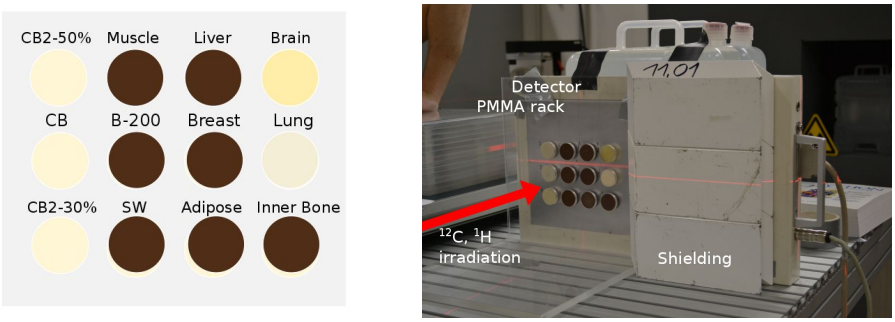

(a) (b)

Figure 4.5: Quantitative soft-tissue contrast measurement setup at HIT. a) Gammex inserts arrangement. b) A PMMA rack with inserted GAMMEX soft tissue equivalent rods is placed directly in front of the detector. Lead shields the electronic read-out of the detector from irradiation.

Table 4.4: Irradiation settings for quantitative soft tissue contrast measurements.

Particle Type	Energy [MeV/u]	Fluence (Particles/mm^2)
^{1}H	48	5.00×10^5
^{12}C	88	0.63×10^5
	302	1.09×10^5
	429	1.11×10^5

figure 4.5 a). The setup has been irradiated with the parameters given in table 4.4. Additional slabs of PMMA were placed between the phantom and the detector to measure the contrast in different depths. Correspondingly, a higher beam energy was used. The signal behind the setup has been measured with the flat-panel detector.

4.3.3 Characterization of the Potential for Mammography

One proposed advantage of ion radiography is the predicted improved soft tissue contrast at reduced dose compared to photon imaging. For mammography low energy photons are used to improve the soft tissue contrast in the breast images implying a relatively high radiation dose. Thus, the potential of ion radiography for mammography is investigated in the following experiments. For realistic comparison, a state-of-the-art mammography unit, Mammomat Inspiration by Siemens (section 3.2.2), was evaluated in terms of soft tissue contrast and spatial resolution.

Table 4.5: Mammomat Inspiration Quality Assurance settings at the Mammomat Inspiration.

Breast Phantom	X-ray Tube Voltage	Anode/Filter	Tube Current Time Product
4 cm PMMA	28 kV	W/Rh	56 mAs

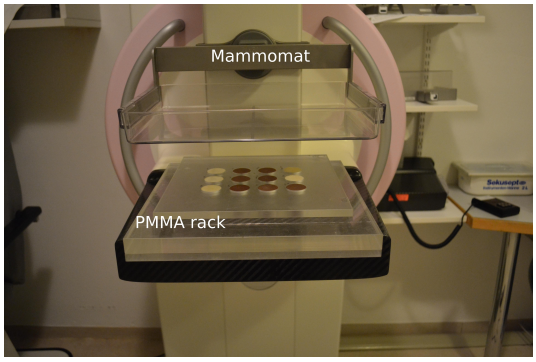

(a) Soft tissue contrast phantom setup.

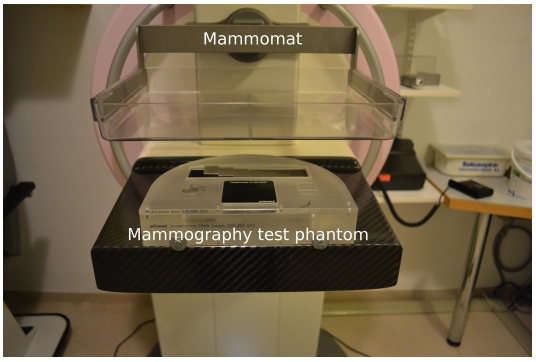

(b) Test phantom for digital mammography with gold-plated detail test objects.

Figure 4.6: Measurement setups at the Mammomat Inspiration.

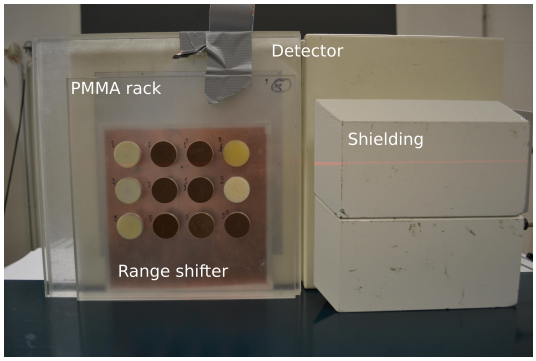

(a) Soft tissue contrast phantom setup with range shifter.

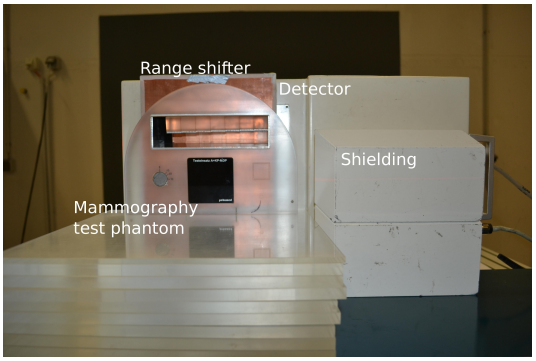

(b) Test phantom for digital mammography measured with the range shifter.

Figure 4.7: Measurement setups at HIT. Both phantoms are positioned in front of the detector, with the copper plate acting as range shifter in between. Detector electronics are shielded from scattered radiation by lead blocks.

Soft tissue contrast was measured with the predefined setup composed of PMMA rack and Gammex rods and additional 3 cm of PMMA adding up to the standardized breast thickness of 4 cm, see figure 4.6 a). Secondly, the test phantom for daily QA with gold-plated detail test objects was imaged (figure 4.6, b). A 1.5 mm tungsten plate tilted at an angle of around 2° was used to measure the ESF for spatial resolution characterization. Quality assurance settings of the machine were basis for all measurements, see table 4.5. The acquired images were then compared to the ion radiographs.

Comparable measurements were carried out with ions, see figure 4.7. To minimize the applied dose, a low particle fluence was used and the copper range shifter was placed in between the imaging object and the detector; see section 3.6 for more details on dose optimization. The results, ion radiography vs. mammography, were compared in terms of contrast, spatial resolution and physical as well as biological dose.

Table 4.6: Measurement settings at HIT for Mammography.

Particle Type	Energy [MeV/u]	Fluence (Particles/mm^2)
^1H	128.11	1.88×10^4
		6.25×10^4
		1.88×10^5
^{12}C	241.84	1156
		5780
		1.16×10^4
	250.08	1156
		5780
		1.16×10^4

4.4 Measurement of the Water Equivalent Thickness

The usage of radiographic proton imaging for particle range verification and patient positioning verification has shown to be very promising (Schneider and Pedroni, 1995). The comparison of the actually measured to the estimated water equivalent thickness (WET) is a measure of the accuracy of the patient treatment plan. The gained knowledge can improve the planning and patient treatment process. The proposed method to measure ion ranges and WET of an object with the flat-panel detector is described in detail in section 3.5.1. It was verified and validated with the following experiments. All ion range verification measurements were carried out solely with carbon ions, because of their supreme imaging characteristics (see section 2.1.2).

4.4.1 Geometrical Phantom

For verification of the method discussed in section 3.5.1, the PMMA head phantom was equipped with tissue equivalent rods (figure 4.8). It has the advantage that the exact geometry as well as the physical characteristic of the used materials are known, see table 3.2. The setup has been irradiated with carbon ion beams of energies ranging from 244 MeV/u to 355 MeV/u and a FWHM of 10 mm at three spot positions with a 10 mm spacing as shown in figure 4.8 a). The measured WET distribution was compared to the calculated values given by the known geometry and material composition. Investigations in terms of dose reduction were carried out. The range verification was exemplarily performed for one of the three beam spots. The phantom was irradiated with a range of energies (244 MeV/u to 355 MeV/u) and varying number of particles per spot (5×10^6, 5×10^5 and 5×10^4). In this way, the dependence of signal-to-noise ratio on the fluence was studied. Furthermore, the usage of a copper plate as a range shifter for dose reduction in WET measurements was studied (see section 3.6). The

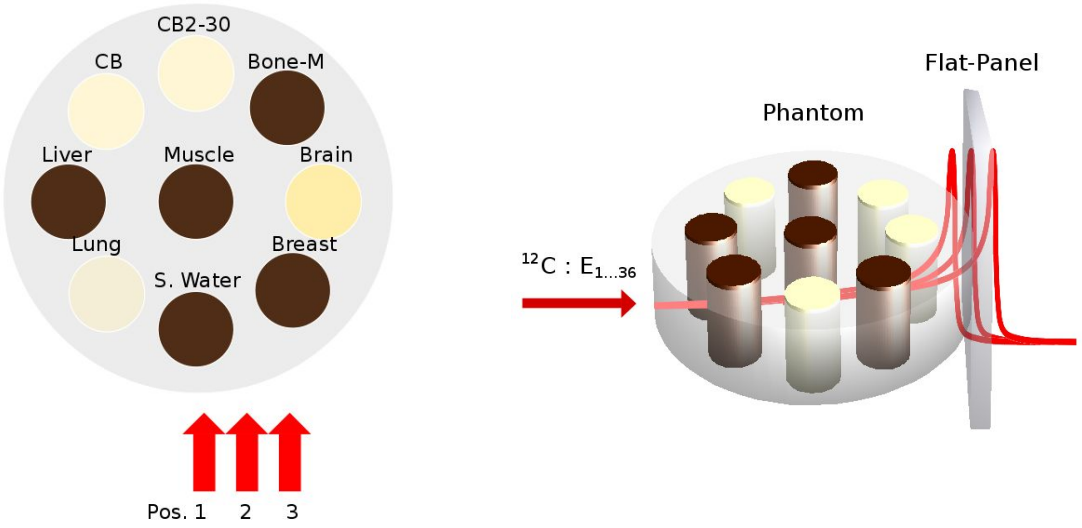

(a) The PMMA head phantom was equipped with the tissue equivalent inserts in the following arrangement. Irradiation was performed spot by spot indicated by the red arrows.

(b) Schematic drawing of the applied method. The detector is placed directly behind the imaging object and is irradiated with ions of several energies.

Figure 4.8: Water equivalent thickness measurement setup for the PMMA head phantom.

setup was irradiated at one of the three beam spot positions with a carbon ion beam of energies ranging from 314 MeV/u to 425 MeV/u. The obtained WET values were compared to measurements without the range shifter.

4.4.2 Biological Sample

In order to investigate the performance of the WEPL measurement technique for biological cases similar in dimension and homogeneity to real patients, a part of a frozen pig head was measured. The pig head was placed in front of the flat-panel detector and irradiated with carbon ions of energies ranging from 244 MeV/u to 355 MeV/u with a mean fluence for each field of 4.90×10^4 particles/mm^2. Two specific regions of the head were of interest; one at the brain, which is enclosed by bony structures, and another one at air-filled cavities. In addition, a WET measurement with the range shifter was carried out to validate the dose reduction method also for more complex setups than the PMMA head phantom.

4.4.3 Anthropomorphic Phantom

In order to mimic a realistic patient setup, an anthropomorphic head phantom was investigated. In the first step a thermoplastic mask was adapted to the anthropomorphic

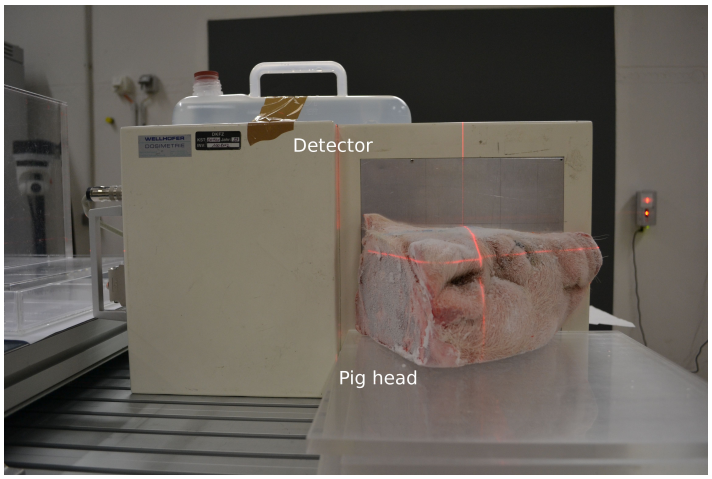

Figure 4.9: The frozen pig is positioned in front of the detector with the sagittal plane parallel to the detector.

(a) Two perpendicular X-ray images are taken for patient positioning verification in the treatment room.

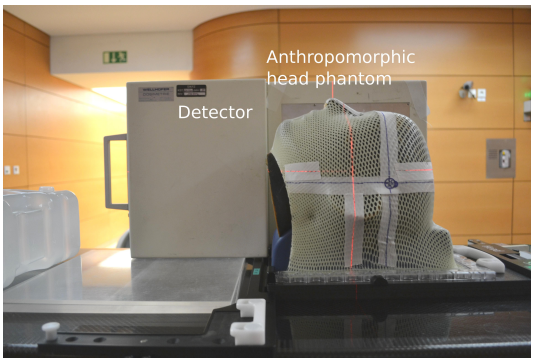

(b) In the final arrangement, the anthropomorphic head is mounted in a thermoplastic mask on the patient couch with the detector positioned in the back.

Figure 4.10: Water equivalent thickness measurement of the anthropomorphic head phantom at HIT.

head and equipped with metal localizers for exact positioning. This reference system is used for carrying out the CT imaging as well as the in-room positioning at HIT. In the step of treatment planning a displacement vector of the treatment couch from the actual position to the target point is calculated. Before the head is moved to its final position, two perpendicular X-ray images are taken for localization verification, see figure 4.10 a). If the position of the metal markers do not agree in the X-ray images and the treatment planning CT image, a position correction vector can be applied until the images match, which translates into couch table movement. This procedure allows very accurate positioning in the order of 1 mm for head fixation and is applied for each patient in clinical practice at HIT.

A region of interest around the skull base, where large complex differences in density

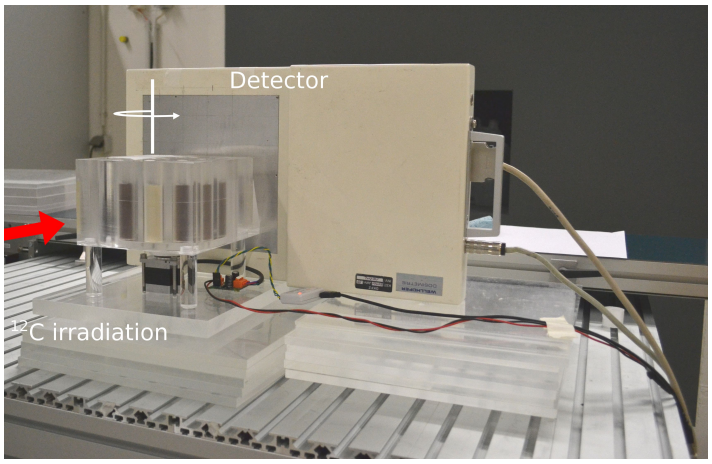

Figure 4.11: Irradiation setup at HIT for tomographic imaging of the PMMA head phantom. The setup is placed directly in front of the detector. Inside the PMMA cube the phantom is rotated automatically.

occur was investigated. This is of high interest for water equivalent thickness measurements and treatment planning algorithm verification. The region was irradiated with carbon ions of 247 MeV/u to 303 MeV/u in 52 energy steps and a mean fluence of $\approx 4.90 \times 10^4$ particles/mm^2 per energy slice.

4.5 Carbon Ion Computed Tomography

As an extension of the proposed WET measurement technique, the feasibility of carbon ion CT with the flat-panel detector was investigated. Carbon ion computed tomography was acquired of the PMMA head phantom assembled with 9 tissue equivalent Gammex rods, see figure 4.11 & 4.12. The WET energy scan measurement technique was slightly modified to accelerate the process. The necessary energy scanning process for the WET measurement was reduced to one single energy by taking advantage of the phantom symmetry and adjustment of the setup. Therefore, the phantom was placed in a $170 \times 170\,\text{mm}^2$ PMMA block with a 19.57° PMMA wedge ajar as seen in figure 4.12 b). The block is used to simplify the geometry and thus minimize the energies needed to measure the WET. Further, the static wedge allows to continuously vary the WET over the phantom. The advantage of this modified setup lies in the fact, that only one energy is needed for irradiation which saves the time consuming energy changes of the accelerator. The setup was irradiated with carbon ions of 341 MeV/u and a fluence of 5.55×10^4 particles/mm^2 for each angle. Rotation was automatically performed in steps of 2.25° over 180° with a step motor. The single images were evaluated in terms of WET value and than reconstructed with a conventional Ram-Lak filtered backprojection algorithm to form WEPL images, see section 3.5.1.

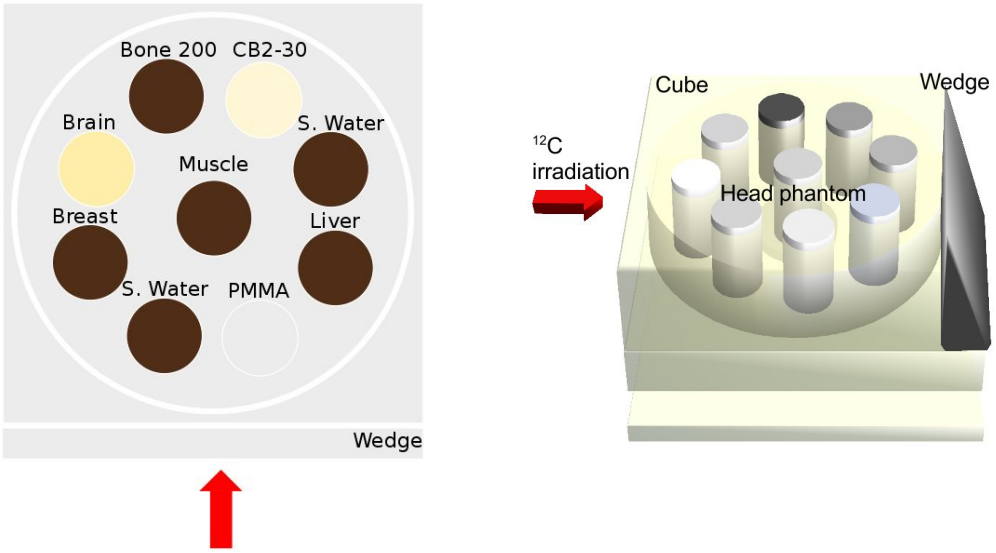

(a) The PMMA head phantom was equipped with the Gammex inserts in the following arrangement.

(b) A PMMA cube and a PMMA wedge are used to speed up the WET measurements.

Figure 4.12: Schematic illustration of the tomographic imaging setup.

5 Results

5.1 Characterization of the Detector Response

The study on detector characteristics is an important step towards gaining understanding of the detector response in ion beams. Experiments were carried out free-in-air and in depth of PMMA, see section 4.1.

5.1.1 Study Free-in-Air

The flat-panel detector response to photon irradiation is well known to be mainly depending on the scintillator foil, while only little contribution is directly formed in the a-Si:H photodiodes. To understand in more detail the detector signal formation, the Monte-Carlo code FLUKA was used to model the energy deposition in the Lanex scintillator and the a-Si:H layer of the detector. Those values were compared to the signal per particle acquired in carbon ion and proton beam measurements free-in-air.

In order to compare the simulated energy loss in the detector layers to the measured values, the signal has been normalized to the simulated energy loss at the highest available energy. This is done, because at high energies the local ionization density is lowest and thus the effect of recombination and local response saturation are as well expected to be low (Butts and Katz, 1967).

In general for all particle types the signal increases towards lower energies due to the increased stopping power of the particles (see section 2.1.1 and figure 5.1). Further, the calculated energy deposited in a-Si:H is about 1000 times lower than in the Lanex foil. Thus, the simulated total energy from both layers is dominated by the energy deposited in the Lanex foil. In the case of proton measurements, the normalized distribution of measured values overlaps with the simulated energy loss in the scintillator, see figure 5.1 (left). On the other hand, for carbon ion irradiation, signal quenching was observed. For lower initial particle energies the detected signal is lower than expected from the simulations: see figure 5.1 (right).

Due to the increasing ionization density of particles in matter with decreasing energy, quenching is expected to occur with increasing stopping power. Figure 5.2 shows the ratio of measured particle signal to simulated energy deposition in the scintillator depending on dE/dx for protons and carbon ions. The data was normalized to the

ratio with the lowest stopping power. For the proton measurements the signal is hardly underestimated. All points in the plot (figure 5.2 (left)) lie very close together being hardly distinguishable. However for carbon ions in the high stopping power region, the signal is strongly underestimated, it is quenched by a factor of around 10^{-2}: see figure 5.2, right.

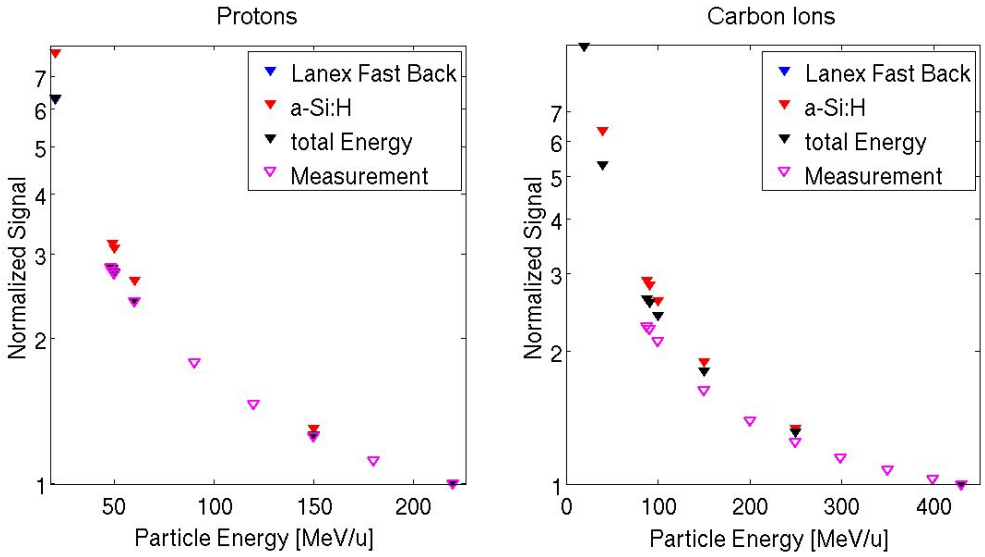

Figure 5.1: Semilogaritmic plot showing the simulated energy deposition in the detector layers and measured detector signals for proton (left) and carbon ions irradiations (right) of different energies normalized to the signal of the highest energy respectively. The energy deposited in the scintillator (blue) overlaps with the total deposited energy (black). Left: Protons: the simulated energy deposition in the Lanex layer overlaps with the measured values. Right: Carbon Ions: the simulated energy loss in the Lanex layer is higher for lower energies compared to the measured signals.

5.1.2 Study In Depth

Signal quenching in depth of PMMA was investigated for a carbon ion beam energy of 300 MeV/u. The treatment planning code TRiP was used to calculate, from interpolation of the basis data obtained at GSI, a carbon ion depth-dose curve in PMMA. The distributions are normalized to 1 at the values free-in-air. The comparison shows strong detector signal quenching in the peak area by a factor of ≈2.3 as shown in figure 5.3. Those values add to the quenching already observed in the entrance channel (free-in-air) quantified in section 5.1.1, which was eliminated here by the normalization.

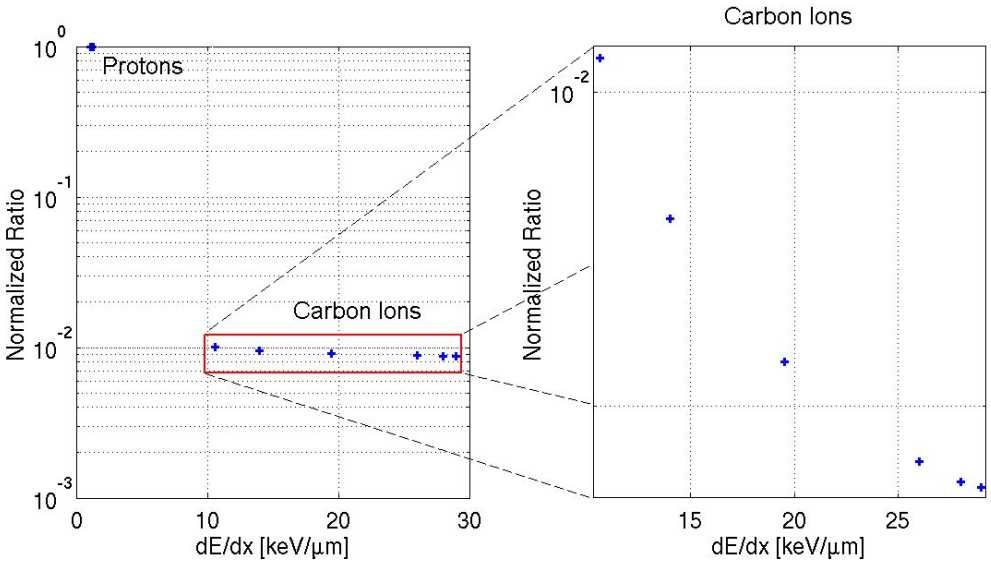

Figure 5.2: Signal quenching depending on particle stopping power for protons and carbon ions. The normalized ratio of measured particle signal to simulated energy deposition in the scintillator depending on dE/dx is shown. Stopping powers for proton and carbon ions were taken from Deasy (1994); Sigmund (2005), respectively.

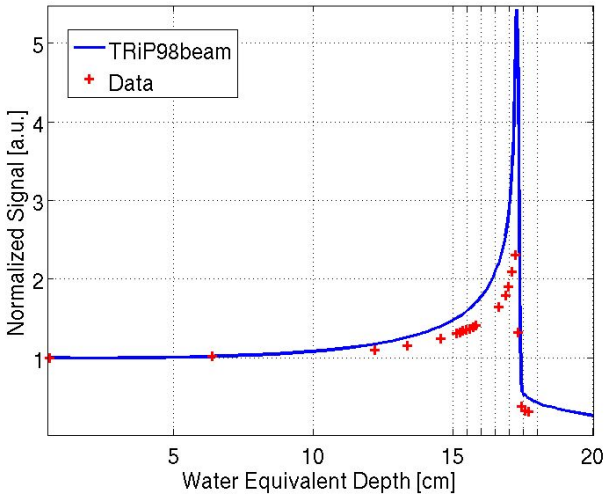

Figure 5.3: Comparison of a calculated depth dose curve (TRiP) with the flat-panel measured values in PMMA for carbon ions of 300 MeV/u.

5.2 Image Processing

Image processing is in general recommended to enhance the measured signal quality. Offset correction of the dark image and sensitivity correction of the pixel matrix were developed and implemented in a new correction routine based on the studies of dark image behavior and measured detector sensitivity matrix, as explained in section 4.2.

5.2.1 Dark Image

Dark images were studied extensively to improve offset corrections for ion radiography. Small differences between dark images occur, when the detector is heating up as illustrated in figure 5.4. When using these dark images for offset correction small deviations in the order of 0.01 % between single frames can sum up to a significant amount due to the large number of frames, typically up to 9000, used for ion radiography. Therefore, it is very important to leave the detector to reach temperature equilibrium before starting the exposure or dark image measurements. For all following measurements the flat-panel detector was left to heat up for a time of at least 30 min before starting any measurements. In addition to the temperature specific effects, a signal difference

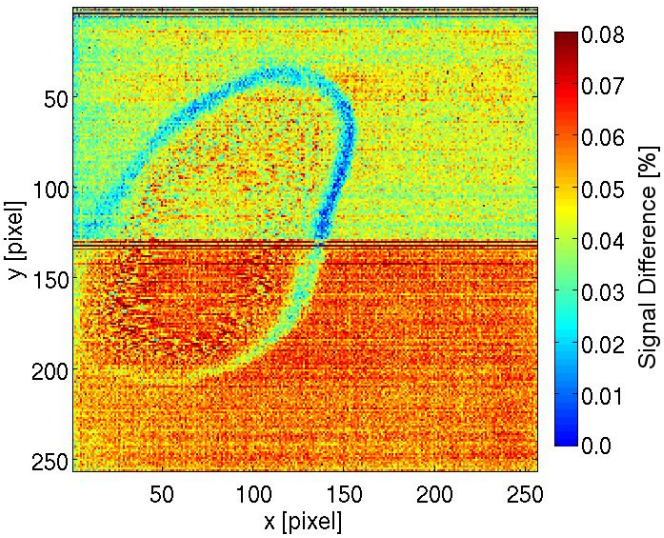

Figure 5.4: Detector signal difference between the first frame after connecting to the power supply and a frame taken about 1 min later. Small signal differences occur between the two detector halves connected to the two different amplifiers. Also differences due to the fabrication process are visible.

between the two detector halves can be observed. The detector consists of two halves, which are readout by the two 128-channel charge amplifiers and vary in gain over time.

This effect is shown in figure 5.5. The histogram on the right shows the drift of the relative signal of the second half to be in the order of 0.1 ‰. Further investigations

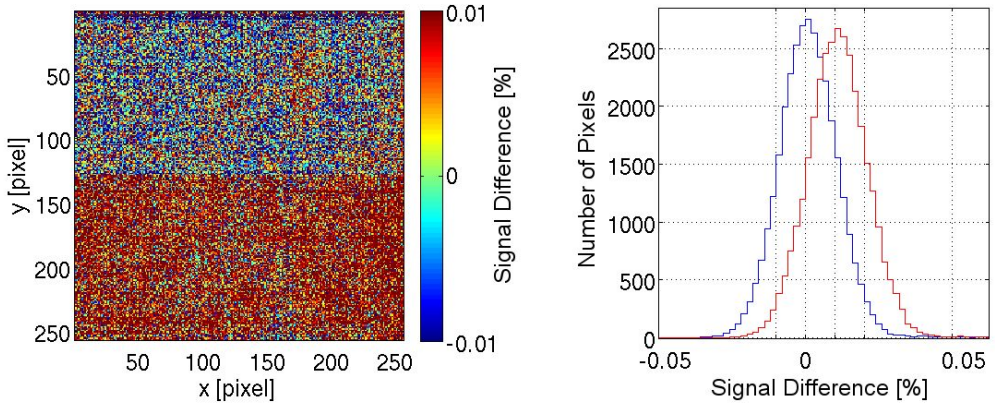

Figure 5.5: Left: Detector signal difference measured with a time difference of 5 min after the heating period of 30 min. Right: Histogram shows the signal shift of the two detector halves (blue: lower detector half, red: upper detector half).

have shown that the upper signal amplifier produces very reproducible results while the lower drifts with time in unpredictable direction.

To gain more information on the dark image behavior, further evaluation of the dark image time dependence has been performed. Exemplary, dark images were analyzed by the usage of regions of interest (ROI), see figure 5.6. For evaluation of the time-development of the dark images, the relative mean signal of the dark images in the ROIs has been plotted against time. Most significant changes of up to $\pm 0.3\,‰$ occur at high x-coordinates (figure 5.6, lower right). The row driver sets the pixels of one line to a certain potential to read them out along the read-out circuit orientated perpendicular to the rows, see figure 3.7 (right). The amplitude of occurring differences increases from left to right along the row driver lines by a factor of ≈ 5.

To take these effects into account, a new image correction routine has been developed.

5.2.2 Active Dark Image and Image Lag Correction

Previous investigations on the dark image behavior were the basis for the following correction procedure. Furthermore, second order effects of previously irradiated and already read-out spots, referred to as image lag and temporary pixel specific offsets (section 3.3) are addressed.

The correction routine is based on the typical synchrotron spill structure of the HIT accelerator system. The spill pause is used to acquire so called active dark images (ADI) to correct for time specific offset variations. Therefore, the routine handles the

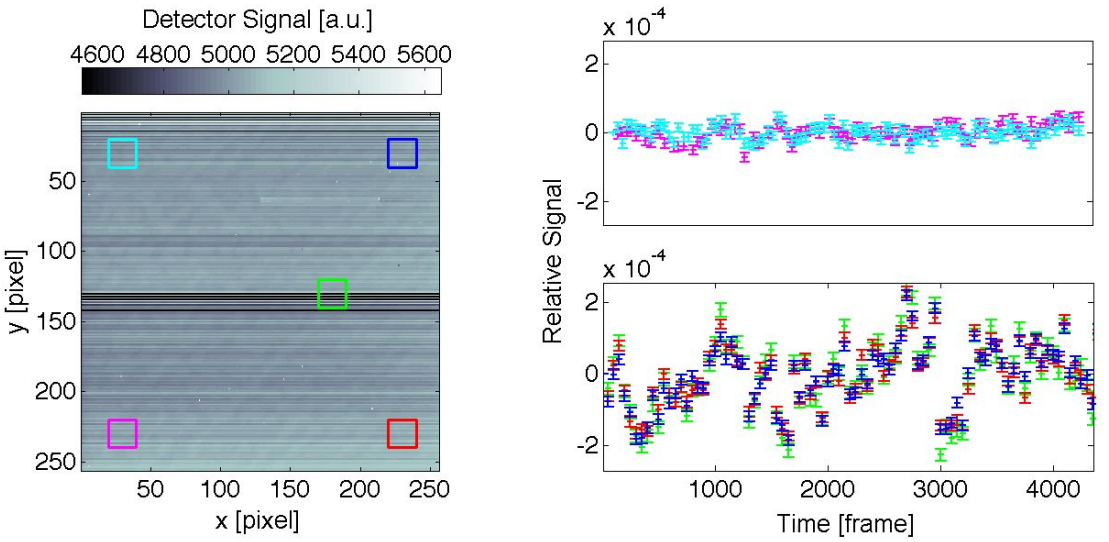

Figure 5.6: Left: Example dark image with marked regions of interest(ROI). The mean dark image has a signal value of around 5000 a.u.. Right: Mean values of ROI plotted against time. The relative signal values were normalized to the first acquired frame after warm-up of the detector. 1 frame$\widehat{=}$0.08 s

summation and correction of image frames in multiple steps dependent on the spill structure. All frames acquired during one irradiation spill and the frames acquired in the preceding spill pause are assigned the spill index n. Images are categorized as spill images or ADIs with a simple threshold on the average pixel value (see figure 5.7).

An uncorrected image $I_n(\mathrm{i},\mathrm{j})$ for one spill n is then given by

$$I_n(\mathrm{i},\mathrm{j}) = \sum_{f=s_1(n)}^{s_2(n)} F_f(\mathrm{i},\mathrm{j}), \tag{5.1}$$

where $F_f(\mathrm{i},\mathrm{j})$ is the pixel value of an acquired frame at position (i,j), f is a successive nominator for the frame number and $s_1(n)$ and $s_2(n)$ give the start and end frame of the spill-related part n, respectively. This spill image is subsequently corrected by subtracting the active dark image $d_n(\mathrm{i},\mathrm{j})$ obtained during the spill-pause-related part of the same spill n:

$$d_n(\mathrm{i},\mathrm{j}) = \frac{1}{\Delta p(n)} \sum_{f=p_1(n)}^{p_2(n)} F_f(\mathrm{i},\mathrm{j}), \tag{5.2}$$

where $p_1(n)$ and $p_2(n)$ give the start and end frame of the spill-pause-related part of the spill n.

In this way, pixel specific offset changes can be corrected for. However, further corrections are needed, as effects of image lag must also be considered.

In the ADI-correction method, the frames taken during spill pauses are not included in the integrated signal. However, they contain the image lag signal, which then would

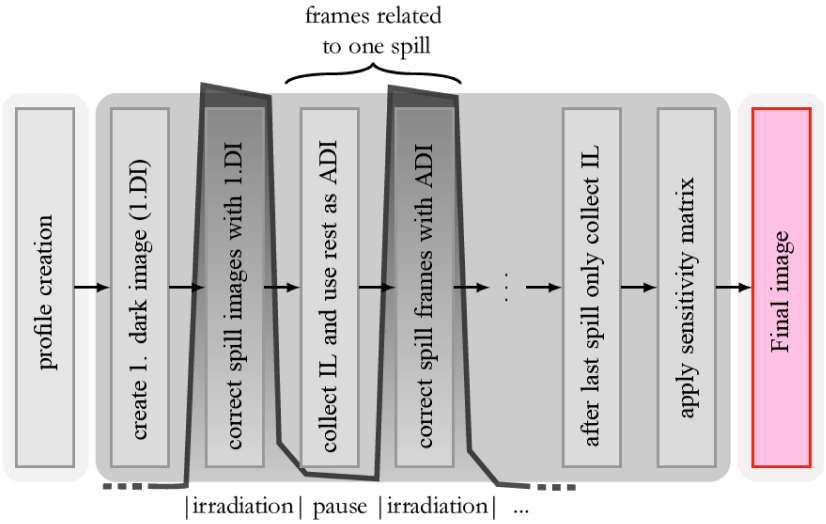

Figure 5.7: Workflow-scheme of the offset correction based on active dark images (reprinted from Huber (2011)). IL stands for image lag. The black shaded region represents the beam intensity and typical spill structure. The pixel sensitivity correction (see next section) performed after the offset correction is also indicated in the image.

be excluded from the final image and would lead to an underestimation of the detector signal being in addition part of the active dark image. To account for this, image lag is detected by exceeding a pixel threshold signal value during the spill pause. The pixels showing image lag are excluded from the active dark image and instead their signal is directly added to the obtained signal. The time evolving vacant pixels in the active dark image are filled with a dark image obtained before irradiation:

$$d_{\text{initial}}(\mathrm{i},\mathrm{j}) = \frac{1}{l}\sum_{f=1}^{l} F_f(\mathrm{i},\mathrm{j}), \tag{5.3}$$

where l is the index of the last frame before irradiation. To achieve good statistics for the initial dark image at least 100 dark frames were acquired.

Before using the initial dark image for the creation of a part of the active dark image, it is corrected for time-dependent amplifier specific offset drifts. These drifts are estimated by the relative mean pixel values over the respective detector halves. To be able to use this procedure, each half is required to have a large image lag free area, which is given in spot scanning irradiation techniques. The drift correction factor is given separately for each of the two detector halves within a spill n:

$$c_n(\mathrm{i},\mathrm{j}) = \begin{cases} c_n(1, i \leq 128\ \forall\ \mathrm{j}) \\ c_n(2, i > 128\ \forall\ \mathrm{j}) \end{cases} . \tag{5.4}$$

Using A as an index set for the area showing image lag, the active dark image is then given by:

$$d_n(\mathrm{i},\mathrm{j}) = \frac{1}{\Delta p(n)} \sum_{f=p_1(n)}^{p_2(n)} \left[F_f((\mathrm{i},\mathrm{j}) \notin A) + (d_{\mathrm{inital}}((\mathrm{i},\mathrm{j}) \in A) \cdot c_n((\mathrm{i},\mathrm{j}) \in A)) \right]. \tag{5.5}$$

The signal in the image lag affected area is collected separately. For the dark image correction of the image lag area, the according area of the initial dark image is used, which is previously corrected for amplifier specific offset drifts:

$$L_n(\mathrm{i},\mathrm{j}) = \sum_{f=p_1(n)}^{p_2(n)} \left[F_f((\mathrm{i},\mathrm{j}) \in A) + c_n((\mathrm{i},\mathrm{j}) \in A) - d_{\mathrm{initial}}((\mathrm{i},\mathrm{j}) \in A) \right]. \tag{5.6}$$

This process is repeated for all spills of the measurements. The final image $I(\mathrm{i},\mathrm{j})$ is acquired by composition of the single spill images $I_n(\mathrm{i},\mathrm{j})$, which were corrected using the active dark images $d_n(\mathrm{i},\mathrm{j})$, and the image lag images $L_n(\mathrm{i},\mathrm{j})$:

$$I(\mathrm{i},\mathrm{j}) = \sum_{n=1}^{N} \left[I_n(\mathrm{i},\mathrm{j}) - \Delta s_n d_n(\mathrm{i},\mathrm{j}) + L_n(\mathrm{i},\mathrm{j}) \right], \tag{5.7}$$

where N is the overall number of spills in the measurement and $\Delta s(n)$ is the number of irradiation-related frames in each spill n.

The performance of this active dark image and image lag correction routine is evaluated in section 5.2.4 together with the pixel sensitivity correction, which is presented in the following section.

5.2.3 Pixel Sensitivity Correction

The pixel sensitivity correction matrix was measured with the *small field patching method* as described in section 4.2. Measurements of the photon field at the Gammatron with a calibrated Kodak X-Omat film showed the standard pixel value deviation in a 2 x 2 cm^2 central area to be below 0.5 % for an applied dose of 2 Gy. Relative to this region the detector was displaced and thus covered entirely with the homogenous area. Afterwards, the images were patched together offline.

The obtained correction matrix and profiles through the middle of the correction matrix are shown in figure 5.8. Over the detector differences between the minimum and the maximum sensitivity correction factor of up to 9 % can be observed. Even larger deviations occur for permanently malfunctioning single pixel and pixel rows. It was found that in most cases the malfunctioning pixel response behaves linearly and can thus be corrected for with this correction matrix. Due to small inhomogeneities in the Gammatron S central field, a systematic local pixel to pixel sensitivity uncertainty of less than 0.7 % remains at the field patching borders.

The obtained pixel sensitivity correction matrix was implemented in the newly developed image correction routine.

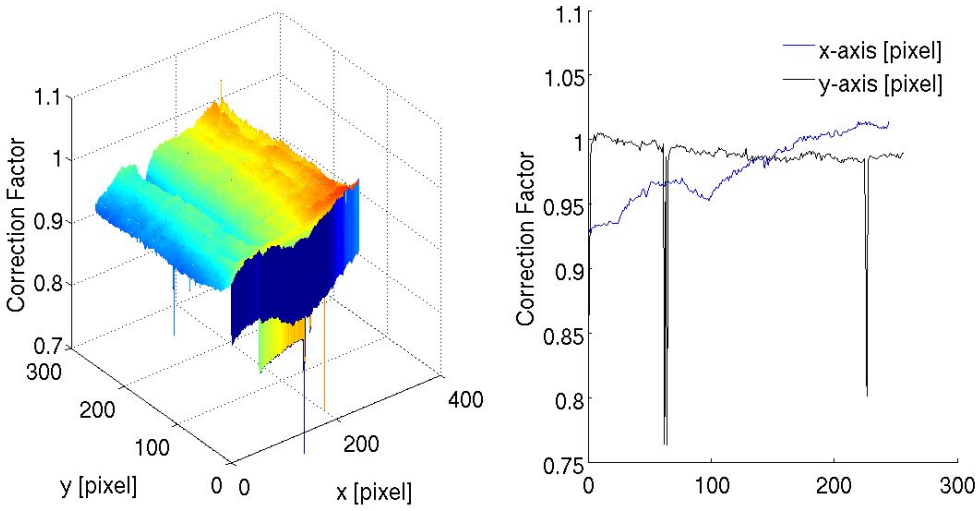

Figure 5.8: Left: Final sensitivity correction matrix. In addition to a systematic gradient of the correction factor along the x-axis, high local deviations, referred to as malfunctioning pixel, are seen. Right: Profiles along the x and y-axis illustrate the characteristic signal gradient.

Applied Correction	Standard deviation [%]	
	Proton field	Carbon ion field
Standard dark image corr. only	1.72	2.29
Sensitivity corr. only	1.30	1.87
Sensitivity & offset corr.	0.62	1.30

Table 5.1: Standard deviations of the signal values for homogeneously irradiated proton and carbon ion fields of $10\times10\,\mathrm{cm}^2$. The high signal gradient at the field boarders was neglected by calculation of the standard deviation obtained over 80 % of the field width.

5.2.4 Newly Developed Image Correction Routine

The newly developed image correction routine includes previously presented correction of dark images and image lag as well as pixel sensitivity.

The performance of the correction procedure was demonstrated using homogeneously irradiated proton and carbon ion fields, see Hartmann et al. (2012). The corresponding standard deviations are listed in table 5.1. For the proton and the carbon ion fields, an improved uniformity of the measured signal distribution over the detector area when employing the sensitivity-correction can be seen. The homogeneity is further improved when the offset-correction is additionally applied.

To exemplarily demonstrate the effect and improvement of the correction routine, one example of a $80\times100\,\mathrm{mm}^2$ proton field irradiation is presented in figure 5.9. From left to right figure 5.9 shows the proton field image with standard dark image correction

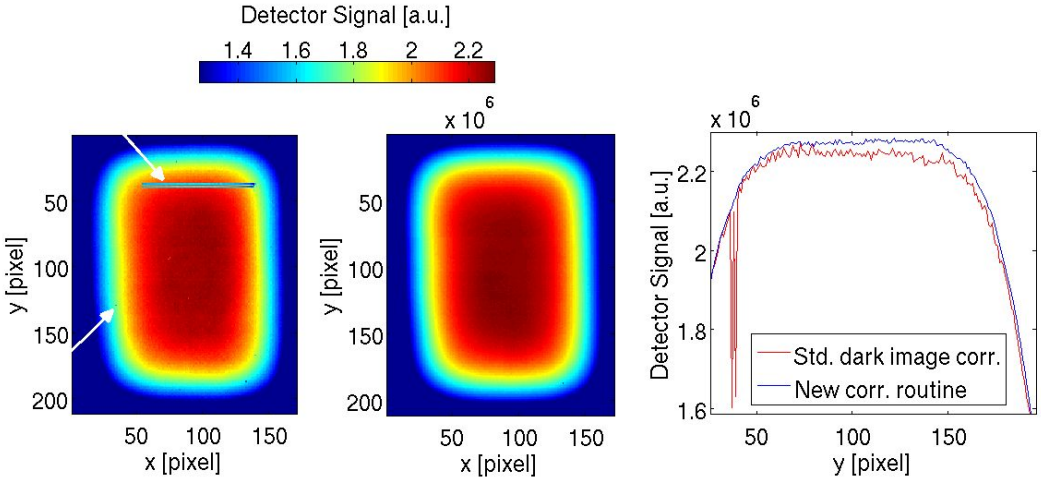

Figure 5.9: Comparison of correction routines for images of a proton field. Left: Applied standard simple dark image subtraction. Malfunctioning pixel and lines (indicated by the arrows) are clearly visible. Middle: Final image after the application of the newly developed routine. All effects are corrected for. Right: Profiles along the y-axis for x=100 to demonstrate the significant improvement by the correction routine for ion radiography.

by a simple subtraction, as routinely applied in photon imaging and the newly implemented routine including the new offset and sensitivity correction. The malfunctioning pixel and lines are all corrected for. In addition, the applied sensitivity correction has an impact on the signal distribution across the field, changing the shape of the measured irradiated field. The obtained results show the importance to correct for pixel sensitivity to achieve high quality images.

For all ion radiographic measurements the newly developed correction routine is applied by default.

5.3 Ion Radiographic Images

To use this detector for ion radiographic imaging is a unique idea and has been employed from scratch in this thesis. The following section presents the obtained results concerning spatial resolution of the images, soft tissue contrast and feasibility for mammography.

5.3.1 Spatial Resolution

Image characteristics in terms of spatial resolution have been quantified using the tilted edge method (see section 3.3) for each of the three radiation modalities, protons, carbon ions, and photons for reference. In addition the data was analyzed both parallel and

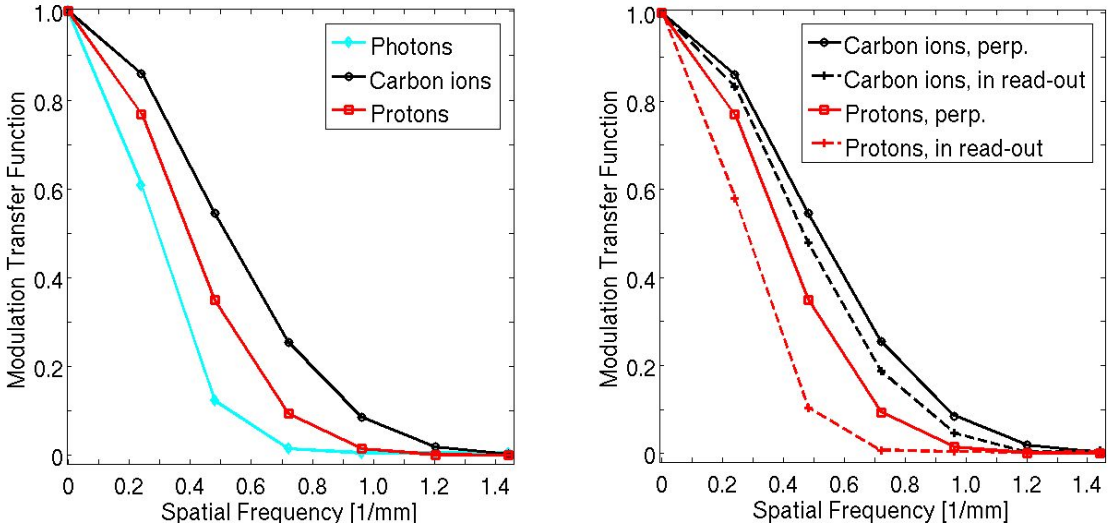

Figure 5.10: Modulus of the normalized MTF for the RID256L detector. Left: Comparison of the photon MTF to the obtained carbon ion and proton MTFs. MTFs were calculated perpendicular to the read-out direction of the detector. Right: Results are shown for carbon ions and protons, analyzed both parallel and perpendicular with respect to the read-out direction of detector.

perpendicular to the read-out direction of the detector, since differences due to the readout process were expected. Figure 5.10 (left) shows the resulting normalized MTF curves for carbon ions, protons and photons. Regarding the beam modalities, spatial resolution of the detector image is increased for ions compared to photons. The carbon ion radiograph shows the highest spatial resolution. Figure 5.10 (right) presents the MTF results for carbon ions and protons in and perpendicular to the read-out direction. Clear differences between both directions can be seen. Spatial resolution drops in read-out direction probably due to signal leakage along the read-out lines, see section 3.3.

From the calculated MTF and measured ESF, respectively the point-spread-function (PSF) can be calculated. The PSF gives a measure of the degree of spreading (blurring) of a point source through the imaging system. In principle, it can be used to deconvolute the obtained images and improve spatial resolution. However, it should be noted that even if the PSF was obtained, the deconvolution process is very sensitive to minor deviations. For the flat-panel detector the response is not isotropic, as it can be seen from the differences of the MTFs in read-out direction and perpendicular to it (figure 5.10, right). Furthermore, it is strongly dependent on the particle type (figure 5.10, left). Therefore, it is not straight forward to determine a realistic PSF for the flat-panel detector in mixed fields typical for ion radiography.

5.3.2 Soft Tissue Contrast

One of the proposed advantages of ion radiography is the high soft tissue contrast possible to reach in the radiographs. Qualitative and quantitative experiments with the flat-panel detector were carried out to demonstrate the soft tissue contrast obtained in the detector images. In the following section the results are presented.

Qualitative Contrast

A knuckle of pork has been radiographed with protons and carbon ions of several energies to qualitatively show the image soft tissue contrast. Three radiographs are presented in the following: two obtained with carbon ions (medium and a high energy) and one obtained with protons (medium energy). The medium energies were chosen to be optimal in terms of contrast by placing the detector in the steep gradient of the Bragg-peak. The energies were estimated by calculation of the water equivalent thickness (WET) image from the knuckles' CT image. The CT numbers given in Hounsfield values are converted into water equivalent path length (WEPL) values via the Hounsfield look-up table implemented in the treatment planning at HIT (table 3.1). Finally, the obtained WEPL matrix is summed up in beam direction to form a WET image see figure 5.13 (left). In addition for carbon ions, the highest available energy was used for imaging.

Figure 5.11 shows the obtained images for carbon ions. In addition to that, the depth dose curves for the corresponding energies are shown on the right side of figure 5.11. The contrasts in the images result from different penetrated WET and thus differences in the energy of the outcoming ions, which deposit different energies dE/dx in the detector. In case of the 250 MeV/u- carbon ion radiography (medium energy) the resulting image shows very high contrast between bony tissue and soft tissue in the middle of the knuckle, but little spatial resolution. On the other hand, the higher carbon ion energy radiograph exhibits an inverted contrast with the background signal being high in comparison to the imaged object. This can be explained by looking at the depth dose curve, which in the entrance region slightly declines. For this energy more fine details of the sample can be observed in the image, which is caused by the decreased scattering of the particles at higher energies.

In the background signal of both images, an irradiation pattern of the scanned beam can be seen. It documents the limited homogeneity of the irradiation field for carbon ions. This effect is of the same order as the differences expected in energy deposition to yield contrast. Given by the specification of the medical accelerator at the HIT facility up to 5 % inhomogeneity in a carbon ion field are tolerable for a successful therapy outcome. This degrades the potential image quality for carbon ion radiography.

For proton radiography the irradiated field shows improved homogeneity due to the

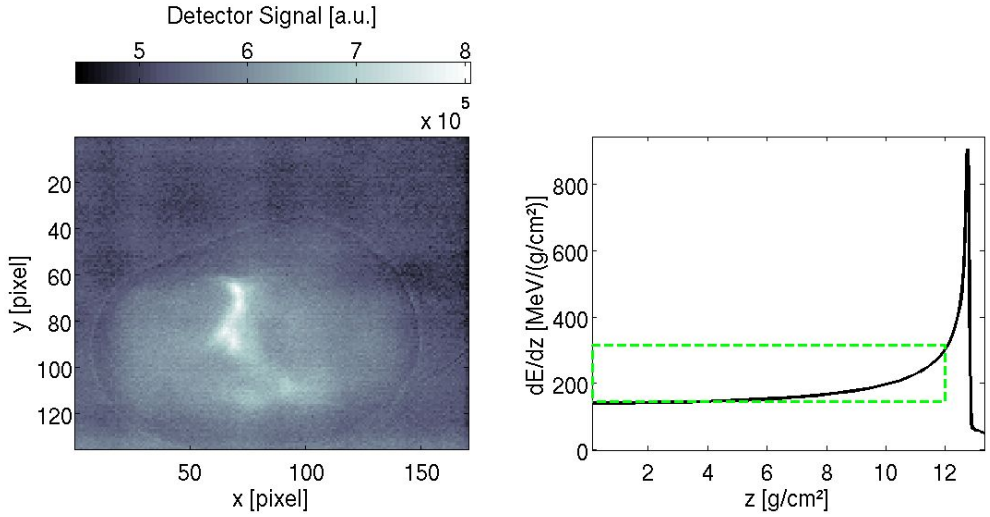

(a) Left: Carbon ion radiograph obtained with an energy of 250 MeV/u. Right: Depth dose curve for the respective particle energy in water. In green the range of water equivalent thickness and energy loss, respectively are framed. The differences in the energy loss cause the contrast in the image.

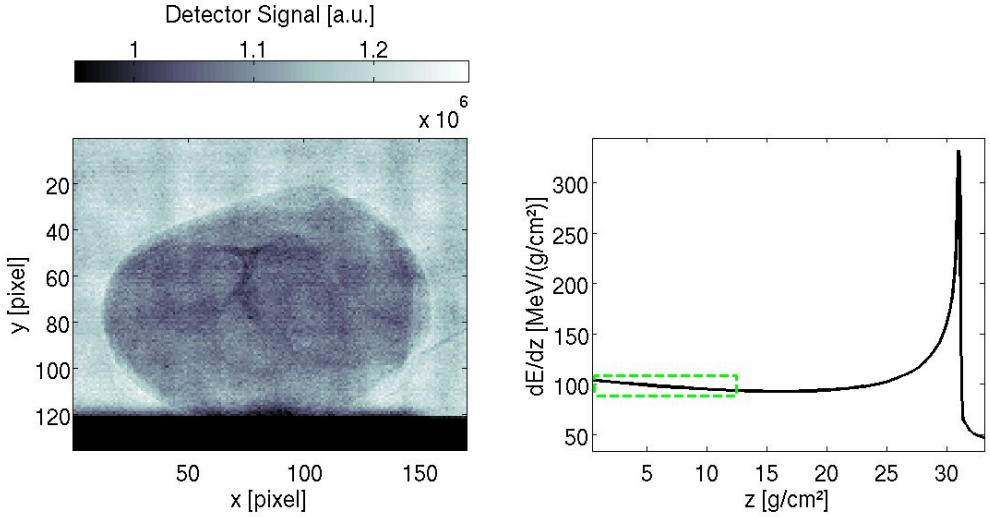

(b) Carbon ion radiograph obtained with an energy of 430 MeV/u and the corresponding depth dose curve in water. The contrast is lower and inverted and the spatial resolution is higher in comparison to a).

Figure 5.11: Carbon ion radiography of the knuckle for two different energies resulting in significantly different acquired images.

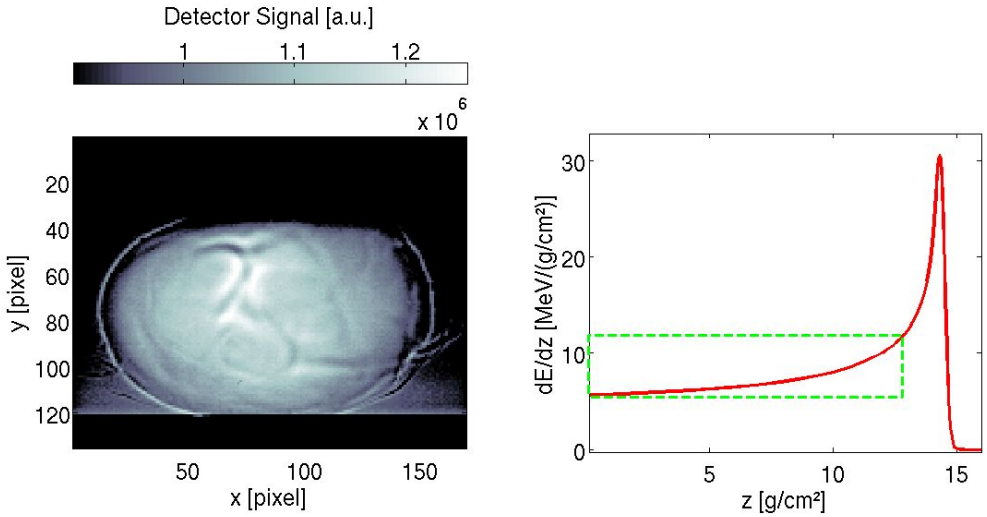

Figure 5.12: Left: Proton radiograph obtained with an energy of 143 MeV/u showing high contrast and high spatial resolution. Right: Corresponding depth dose curve in water.

overlapping of broader beam spots. This results in a knuckle's radiograph with very fine details, see figure 5.12. However, the contrast in the ion radiograph is not only given by differences in energy deposition of the particles but also by occurring differences in particle fluence due to scattering of the particles at material interfaces. This explains e.g. the edge-enhancement of the outer border of the knuckle in the proton radiograph.

For image information comparison, the WET image obtained from the CT image of the knuckle is plotted in figure 5.13 (left). Hypothetically, if multiple Coulomb scattering would be absent and the image information in the ion radiograph would result from a linear gradient of the Bragg-curve, both modalities should result in comparable images. The overall shape and size of the knuckle in the WET image and the proton radiograph agrees well. The profiles along the red line show one example for principal differences in image information obtained with the two different imaging modalities.

Quantitative Contrast

In order to quantitatively measure the achievable soft tissue contrast in ion radiographs with the flat-panel detector, tissue equivalent materials embedded in a PMMA rack have been imaged. Figure 5.14 shows the obtained radiographs with protons and carbon ions of the lowest available energy chosen due to the small sample thickness. The achieved contrast is different for the two particle species. The detector signal values were evaluated quantitatively by placing a region of interest (ROI) with a diameter of 10 mm over each of the inserts. For the ROIs the mean signal values and standard deviations were calculated.

Figure 5.15 shows the signal values plotted against the WEPL values of the inserts

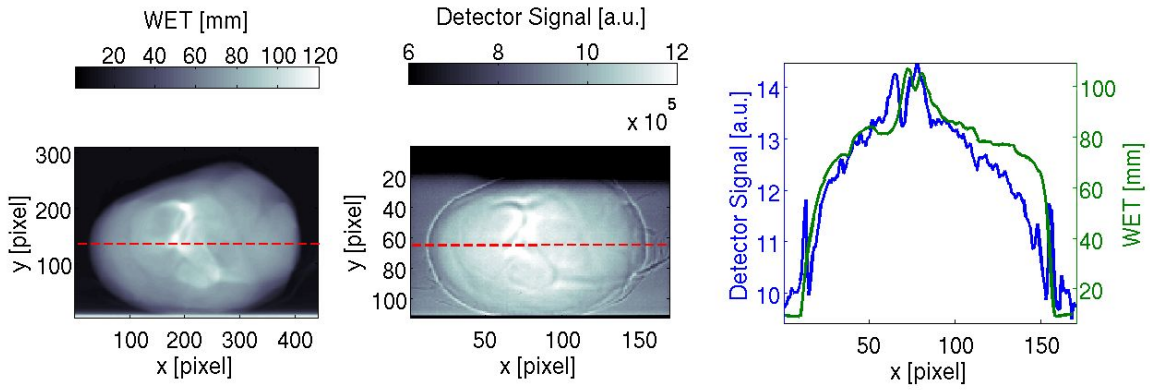

Figure 5.13: Comparison of image information. Left: CT image calculated into WET. Middle: Proton radiograph like figure 5.12. Right: Profiles along the red lines showing in detail the very different image informations given in the WET and proton image.

(table 3.2) with one sigma uncertainty for all obtained radiographs. The values are normalized to the signal of adipose tissue for better comparison. The dependence of the signal values on WEPL are different for different energies and particle species. Comparing protons (48 MeV) and carbon ions (88 MeV/u) of similar ranges, degradation of soft tissue contrast for carbon ion radiographs due to quenching of the signal can be observed. For carbon ions irradiation with an energy of 301 MeV/u, additional slabs of PMMA were placed in front of the detector to measure with the detector approximately in the same high gradient region of the Bragg peak. However in depth of PMMA, particle scattering degrades the peak and the contrast as seen in figure 5.15. A special case is the contrast obtained for the high energy carbon ion irradiation (429 MeV/u). The energy was not sufficiently high enough to irradiate completely through the setup, so that the obtained signals result from the descending flank of the Bragg peak. This causes high inverted soft tissue contrast. In all obtained radiographs the tissue contrast enables to differentiate between all six soft tissue equivalent inserts, ranging from adipose to liver. This was possible even in high penetration depths using higher energies.

The direct measurement of the water equivalent thickness of an imaging object allows to estimate the accuracy of the treatment planning algorithm by comparison of the measured to calculated WET images. So far the flat-panel detector was used to measure ion radiographs solely. However for a given particle energy, a comparison of the absolute measured signal values behind the tissue-equivalent inserts with values obtained in depth of PMMA (figure 5.3) allows to calculate the WET values for the inserts. This

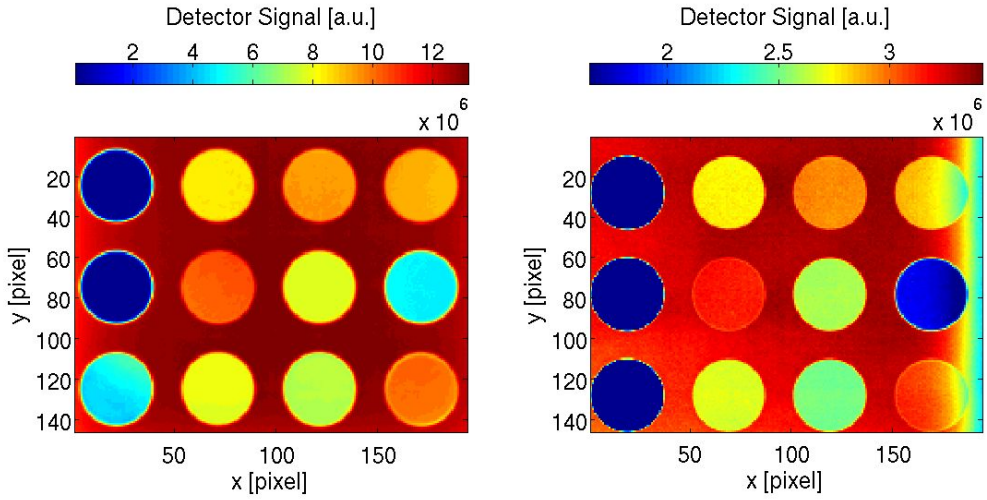

Figure 5.14: Left: Proton radiograph (E=48 MeV) of Gammex tissue-equivalent rods. Right: Carbon ion radiograph (E=88 MeV/u) of the same phantom. At the right side of the image the drop-off of the homogeneous irradiated field can be seen.

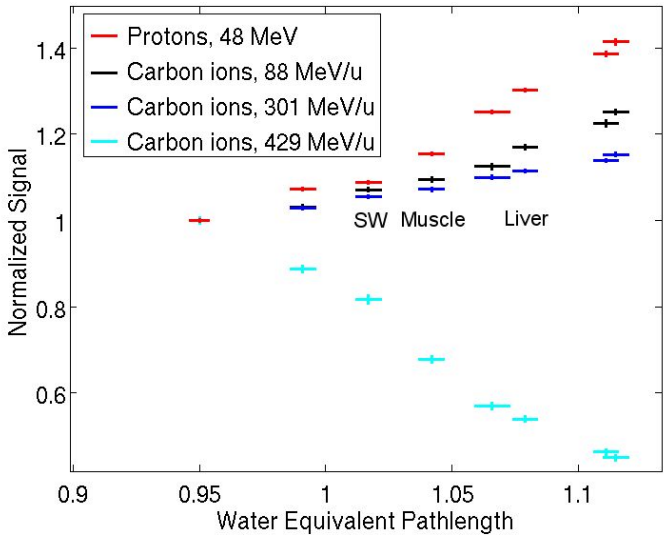

Figure 5.15: Regions of interest (ROIs) were placed over the Gammex rods in the radiographs (figure 5.14) to analyze the signal dependency on their material specific water equivalent pathlength (table 3.2). This was done for protons and carbon ions of different energies. The values are plotted with one sigma error bars and normalized to the adipose value. Indicated are the solid water (SW), the muscle and liver values.

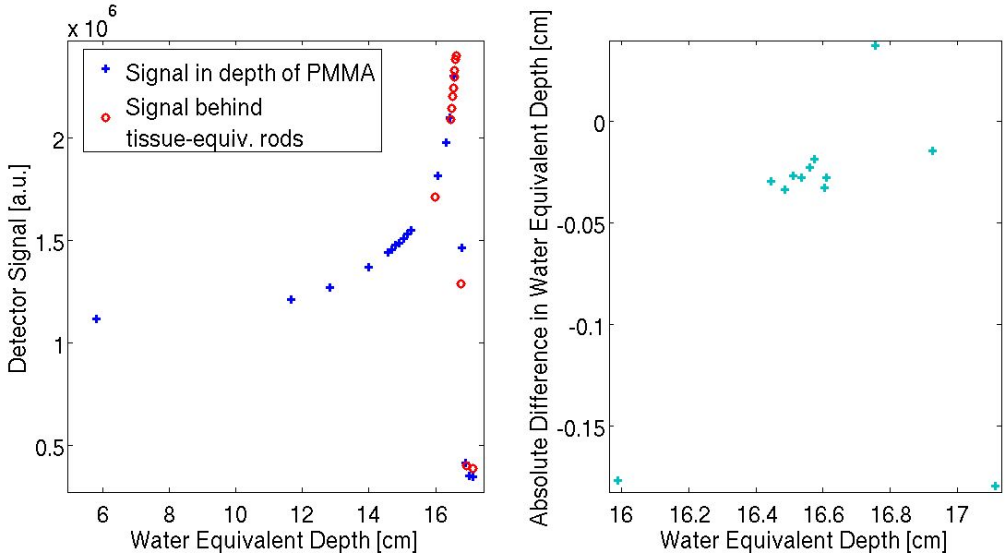

Figure 5.16: Left: Detector signal in depth of PMMA for carbon ions 300 MeV/u (see section 5.1.2) compared to signals obtained behind the tissue-equivalent inserts. Right: Difference of measured to reference water equivalent depth for all inserts.

was done by comparing the detector signal values obtained behind the tissue-equivalent rods (setup as described above with additional 15.7 cm of PMMA) to the reference values in depth of PMMA fitted to a spline. The location of the detector signal value in depth equates to the WET of the penetrated object, see figure 5.16. The assumption is that the particle field, the fluence and scattering of particles can be assumed to be in the same order for penetration of the imaging object and the reference PMMA measurement. The absolute difference of the obtained WET values and the calculated values, which are given by the known material composition and geometry, shows slight deviations. Larger deviations occur at flat parts of the depth dose curve and the tail of the peak. Highest accuracy is given around the peak position. However, the overall accuracy is better than 1 % for all inserts, which shows the feasibility of this method within the described limitations.

5.3.3 Characterization of the Potential for Mammography

Mammography could be one field of application for ion radiography, since high contrast at low dose is desired. The flat-panel detector's performance for ion radiographies was compared to a state-of-the-art mammography system.

The spatial resolution characterized by the MTF of the imaging systems is compared in figure 5.17. The response of the Mammomat a-Se detector with a pixel size of $85\times85\,\mu m^2$ was rebinned to match the flat-panel pixel size of $0.8\times0.8\,mm^2$. The resulting MTF is very similar to the one measured in the carbon ion radiograph and slightly better than in the proton radiograph. The same effect can be observed for

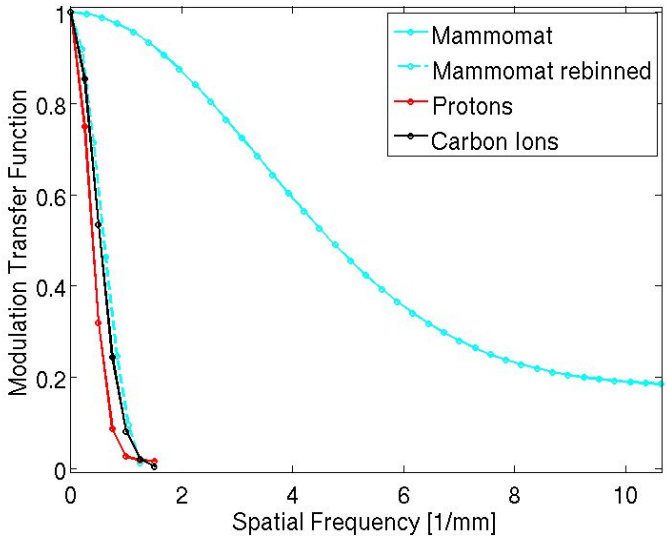

Figure 5.17: MTF for the Mammomat Inspiration unit compared to the proton and carbon ion measurements with the flat-panel detector at HIT. In addition to the original data obtained with the Mammomat, the images were rebinned to match the flat-panel detector pixel size of $0.8 \times 0.8\,\mathrm{mm}^2$ before calculation of the ESF.

the resulting images from the gold-plated test object, see figure 5.18. The rebinned Mammomat image in the middle has roughly the same resolution and noise level as the image obtained with carbon ions of 250 MeV/u and a fluence of 1156 particles/mm^2. However, the obtained contrast is different in the carbon ion radiograph in comparison to the Mammomat images. The small structures of the gold filling can be seen in all images, but in the ion radiograph even small changes in the thickness of the PMMA (figure 5.18 second and fourth row of the plates) cause high signal differences when measuring with the detector in the Bragg-peak region. For some measured pixels the energies of some of the particles are not high enough to pass through the imaging object, which explains the inverted contrast in these rows. Further, the quantitative soft tissue experiments with the PMMA rack and the soft tissue equivalent inserts were carried out at the Mammomat and once again at HIT for the specific mammography settings (see section 4.3.3). The results for carbon ions and protons with the lowest investigated fluence are shown in figure 5.19 (left). The values are normalized to the adipose tissue value for better comparison. The steep fall-off of the Bragg-peak gives rise to high contrast. For comparison the image values of the mammograph are plotted against the electron density of the tissue equivalent inserts (table 3.2). Figure 5.19 (right) shows a close-up of the soft tissue equivalent inserts. The contrast obtained in the carbon ion radiograph is higher than the contrast in the mammograph which is comparable to the proton radiograph. Further it can be noted, that the normalized signal for the breast insert in the mammograph is higher than one would expect from

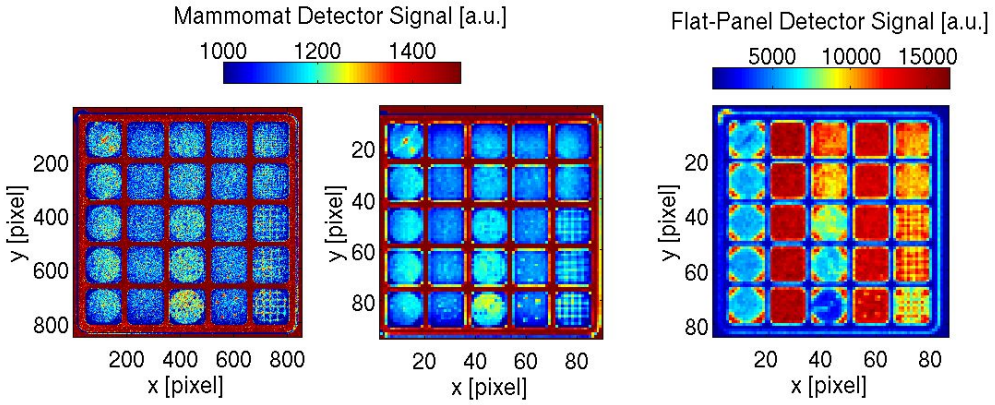

Figure 5.18: Left: Original Mammomat Image of the test phantom. Middle: Binned Mammomat image to match flat-panel pixel size of $0.8 \times 0.8\,\mathrm{mm}^2$. Right: Original flat-panel image obtained with carbon ions of 250 MeV/u and a fluence of 1156 particles/mm^2.

the signal distribution. This is due to the fact, that these Gammex inserts are made of tissue equivalent materials, however the composition of the breast insert does not match tissue realistic chemical composition and the electron density, respectively.

Finally to compare flat-panel ion radiography vs. mammography, the applied doses were evaluated. For the measured ion radiographs the dose was optimized (section 3.6) by reduction of particle fluence and employment of the range shifter.

The physical dose D_{phys} is given by equation 3.12 and listed in table 5.2 for the lowest measured ion fluences and a proton energy of 128 MeV and carbon ion energy of 242 MeV/u. For the Mammomat, imaging doses were estimated by the system and given as a system output. The dose deposition of the three imaging modalities is comparable in the order of a few mGy as presented in table 5.2.

Table 5.2: Comparison of the physical dose D_{phys} for the acquired proton, carbon ion and mammography images.

Radiation Modality	Physical Dose [mGray]
Protons	1.86
Carbon ions	2.49
X-rays (Mammomat)	1.80

However, the relevant quantity for dose comparison is the biological dose, which can be estimated by:

$$D_{\mathrm{biol}} = \mathrm{RBE} \cdot D_{\mathrm{phys}} \tag{5.8}$$

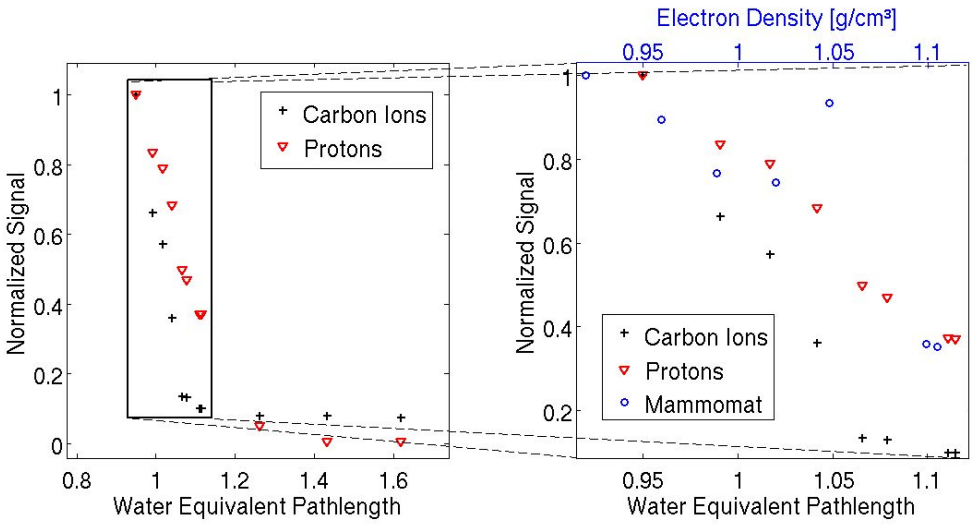

Figure 5.19: Left: Soft tissue contrast of the tissue-equivalent inserts obtained from the ion radiographs (^1H: 128 MeV, $6.25 \times 10\,4$ particles/mm^2, ^{12}C: 242 MeV/u, 1156 particles/mm^2). The flat-panel detector signal values are plotted against the WEPL values (table 3.2). Right: Close-up of the signal comparison obtained from the ion radiographs and mammography. The mammography signal values are plotted against the electron densities of the tissue-equivalent materials (table 3.2). For better comparison, all values were normalized to the adipose tissue value.

with RBE being the relative biological effectiveness, which expresses the relative amount of dose of a radiation type on biological tissue compared to the reference photon radiation (section 2.1.1).

RBE values for mammography are considered to be between 1 and 6. Recent publications estimate the RBE of X-ray mammography to be 4.02 ± 0.72, see Heyes et al. (2009) and Heyes and Mill (2004). For protons a generic RBE of 1.0-1.1 is used, which means that there is a single RBE value, which is applied to all proton beam treatments independent of dose, stopping power and initial energy (Paganetti et al., 2002). For carbon ions the RBE is strongly LET dependent. It was estimated by the Local-Effect-Model, see section 2.1.1.

Table 5.3: Biological dose D_{biol} comparison for proton, carbon ion and mammography images.

Radiation Modality	RBE	Biol. Dose [mGray]
Proton	1.1 ± 0.16 (Paganetti et al., 2002)	2.05 ± 0.30
Carbon ions	6 ± 4 (LEM IV: X-rays, 30 kVp: α/β: 0.41 Gray (Mestres et al., 2008))	14.94 ± 9.96
X-rays (Mammography)	4.02 ± 0.72 (Heyes et al., 2009)	7.23 ± 1.30

Table 5.3 shows the comparison of the RBE values and the estimated biological doses for the three imaging modalities. In terms of biological dose, protons are the superior

imaging modality with a factor of 3.6 lower dose than the mammography system. For carbon ions the dose estimation is a factor two higher than the biological dose for mammography and has a large uncertainty resulting from the RBE calculation.

5.4 Measurement of the Water Equivalent Thickness

Measurement of the water equivalent thickness of phantoms with the amorphous silicon flat-panel detector has been investigated using the proposed method of energy variation (see section 3.5.1). Solely, carbon ions were used to image three different objects: a PMMA phantom, a pig's head and an artificial anthropomorphic head phantom composed of tissue equivalent materials. In the following section the results are presented.

5.4.1 Geometrical Phantom

As a first approach to study the performance of the proposed technique a very simple phantom setup, the PMMA head phantom (section 3.4.1), has been imaged. The water equivalent thickness (WET) was calculated from the known geometry and composition of the used materials. Figure 5.20 shows a sketch of the irradiation setup (left) and the calculated WET values (right). The accuracy of the proposed technique is given by comparison of the calculated WET values to the flat-panel measured values. Therefore, a profile of the obtained WET image is evaluated as indicated by the green box in figure 5.20 (right).

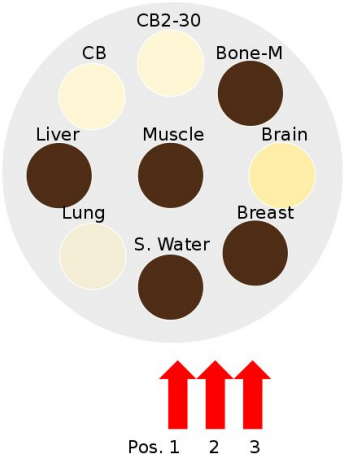

(a) Schematic setup with arrows indicating area of interest.

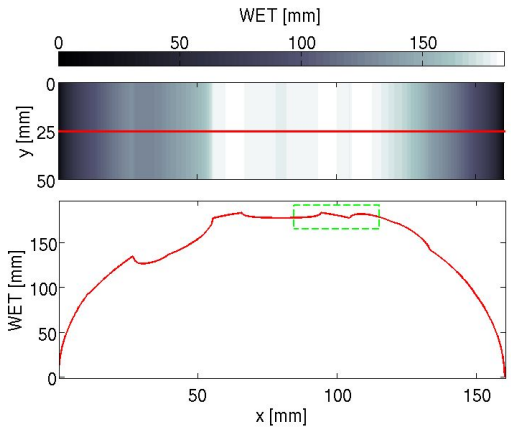

(b) Calcluated WET values. Top: Projected WET distribution of the phantom. Bottom: One profile along the phantom is evaluated. The green box marks the area of interest.

Figure 5.20: Ion range measurements of the PMMA head phantom. Illustration of the investigated area.

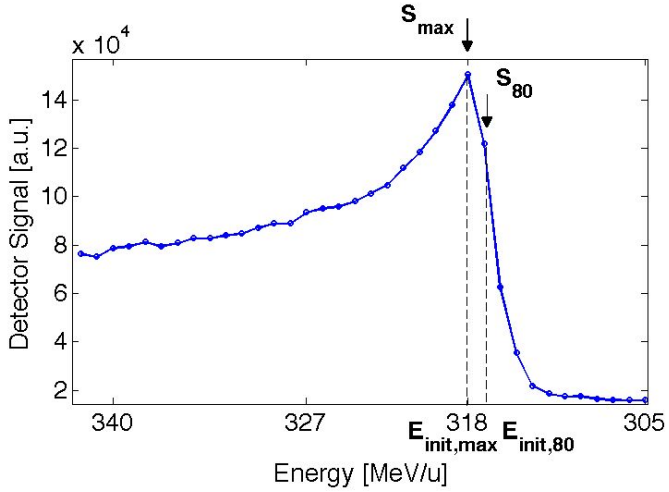

Figure 5.21: Experimental WET evaluation. For each detector pixel a energy-signal curve is measured. The penetrated WET corresponds to the peak position $S_{\max}$. The nominal resolution can be increased by evaluation of S_{80}.

The WET measurement was carried out as described in section 3.5.1. An energy-signal curve was measured by variation of beam energy for each detector pixel, see figure 5.21. The obtained peak position corresponds to a certain energy $E_{\text{init,max}}$, which is translated into WET. As seen in figure 5.22 (left) the measured WET values agree well with the expectation. However, the nominal resolution of the energy steps limits the measured WET resolution. The energy steps are given by the design of the accelerator, they are 1 mm WET for low and medium energies and 1.5 mm WET for high energies. The resolution can be increased by interpolation of the energy-signal curve and evaluation of S_{80} at which the signal amounts to 80 % of the peak value at the descending flank of the peak, see figure 5.21. This idea is based on the fact that the particle CSDA range is given by the point corresponding to the 82 % of the peak maximum (section 2.1.3). The WET_{80} value obtained at 80 % of the signal increases WET resolution as seen in figure 5.22 (right). However, the measured values are slightly lower than the calculated values. This underestimation can be quantified by investigation of the energy-signal correlation. Assuming a low probability of particle multiple Coulomb scattering in homogeneous material, energy variation only shifts the Bragg peak in depth while preserving the peak shape. Therefore, the shift between the $S_{\max}$ and S_{80} value is nearly constant and can be used as a correction factor. Figure 5.22 (right) shows the corrected WET_{80} values. They agree very well with the calculation. However, in the case of more complex imaging objects the Bragg peak degrades due to multiple Coulomb scattering (for more information see section 2.1.2). This Bragg peak degradation leads to an increased peak width. The given

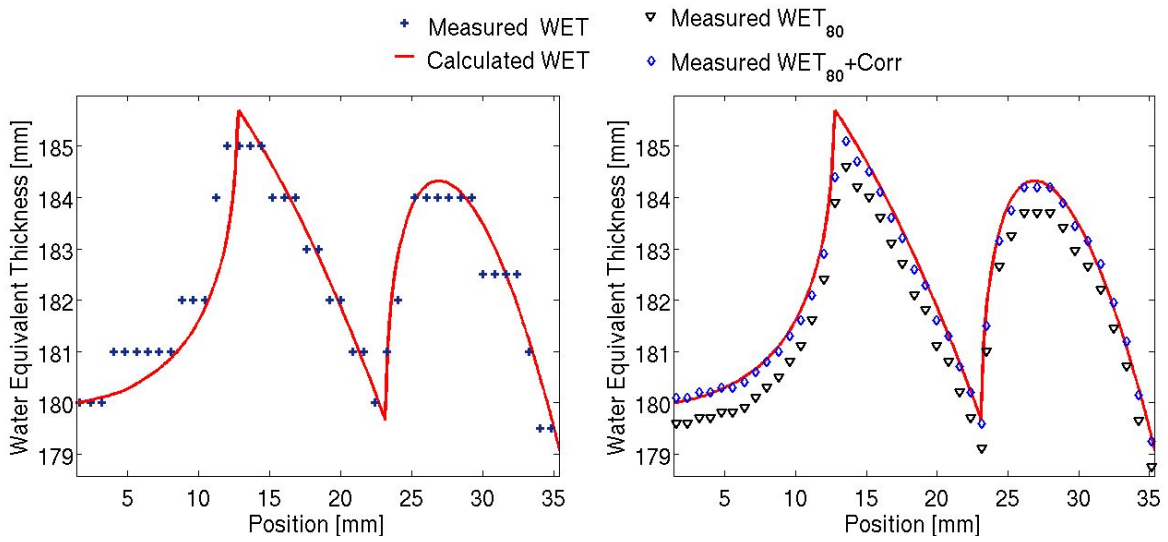

Figure 5.22: Comparison of the calculated and measured WET values. Left: Measured WET obtained at $S_{\max}$. Right: Measured WET obtained at S_{80}. A correction shift is applied to the measured WET values to agree well with the expected calculated WET distribution.

energy $E_{\text{init},80}$, at 80 % of the maximum signal, is then shifted to higher energies, which corresponds to smaller WET_{80} values. This effect is strongly correlated to the local inhomogeneity of the imaged object. For the WET measurement of the simple PMMA head phantom, only minor Bragg peak degradation takes place at the sharp edge at around 13.5 mm of the WET distribution: figure 5.22 (right). Here the WET values are slightly underestimated in comparison to the calculated values.

The dependence of the measured WET on particle fluence and dose accordingly was investigated. In three measurements the particle fluence was reduced each time by a factor of 10. The resulting WET distributions of a beam spot measured at position 1 (see figure 5.20) are shown in figure 5.23. With decreasing amount of particles N_p, the signal drops linearly. The WET images show an area where the method works well given a certain minimum of particles. On the outside where the particle fluence decreases due to the normally distributed fluence, noise dominates. This is why the beam spot seems to decrease in size from left to right.

Another very effective approach to reduce the amount of deposited dose, is to shift the depth-dose curve and the peak, downstream of the imaging object by using a range shifter (section 3.6). The influence of a range shifter on WET determination was studied. Therefore, the WET distribution at position 2 of the phantom (see figure 5.20) was measured with and without the range shifter. The results are shown in figure 5.24. The WET distribution obtained with the range shifter was measured with the proposed WET measurement technique at higher energies and additional subtraction of the water equivalent thickness of the copper stack value $\text{WET}_{\text{r-shifter}}$=72 mm. The

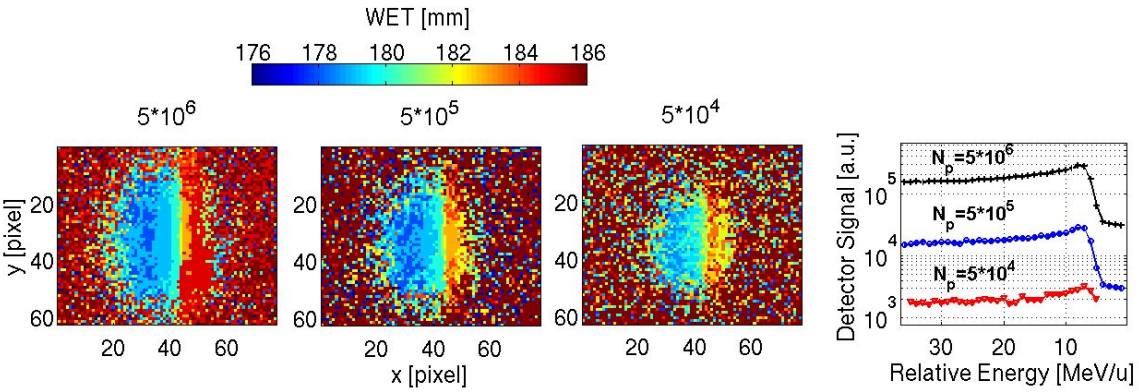

Figure 5.23: From left to right: 5×10^6, 5×10^5 and 5×10^4 particles per single spot. Right: Signal to energy distribution for one single pixel plotted for each of the measurements.

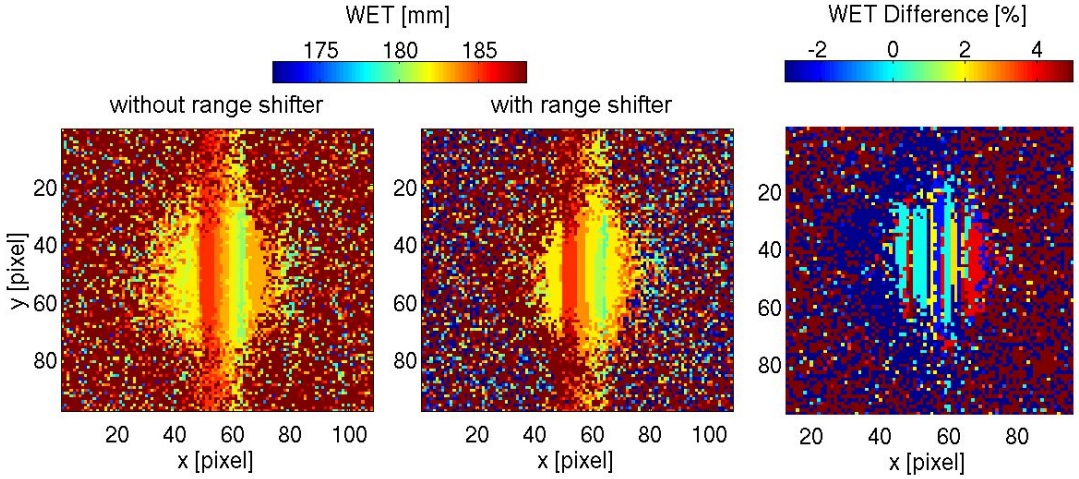

Figure 5.24: WET map measured with carbon ions without (left) and with the range shifter (middle). The WET difference map (right) shows that only slight deviations of a few percent occur.

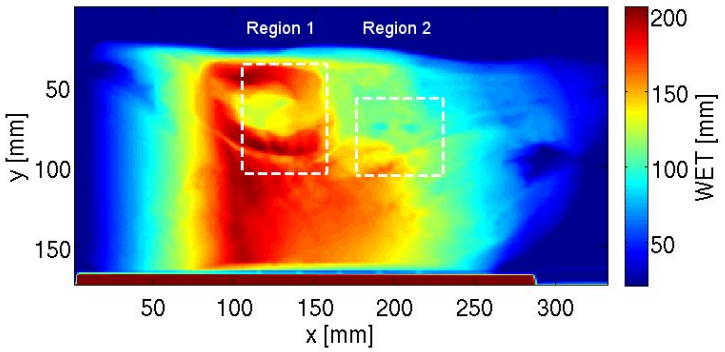

Figure 5.25: WET map of the frozen pig head with the regions of interest indicated in white. The WET values were calculated from CT data.

result agrees very well within ±2 % of the WET image obtained without range shifter. For measurements with the range-shifter the used energies are higher and given by the design of the accelerator the focus size of the beam is smaller. This results in larger deviations between both measurements at the beam spot boarder, see figure 5.24 (right). In the next section the usability of the range shifter method for more complex biological measurements is investigated.

5.4.2 Biological Sample

A frozen pig head was measured to investigate the feasibility of the energy scan method for more complex two dimensional WET distributions. Due to the complex heterogeneous structure of the frozen pig and occurring Bragg peak degradation the proposed improvement of the nominal WET resolution by evaluation of the S_{80} as presented in the previous section is not further employed.

Two specific regions of the frozen pig head were measured and compared to the calculated WET image obtained from CT data. The calculated WET distribution was obtained by transforming the CT numbers of the CT image into WEPL with the Hounsfield look-up table and integration of the WEPL values along the beam direction. The investigated regions of the pig head are indicated in the calculated WET map (figure 5.25). Region 1 includes steep WET gradients resulting from the "C-shaped" boney structure enclosing the brain. Region 2 was investigated, because it includes small cavities also resulting in steep WET gradients.

The obtained results are shown in figure 5.26 and 5.27 for region 1 and 2, respec-

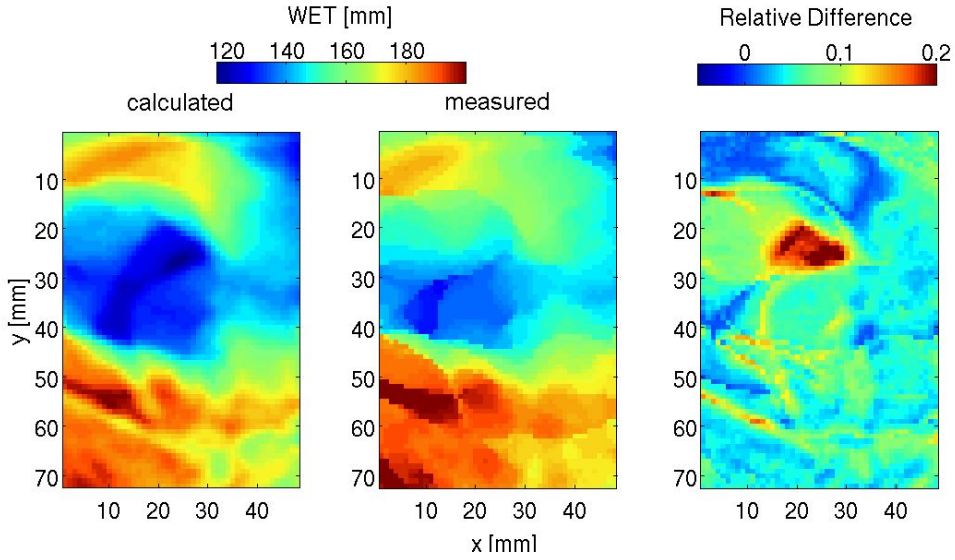

Figure 5.26: Region 1: Left: WET map calculated from CT data. Middle: Measured WET distribution with carbon ions. Right: Relative difference between the calculated and measured WET distribution.

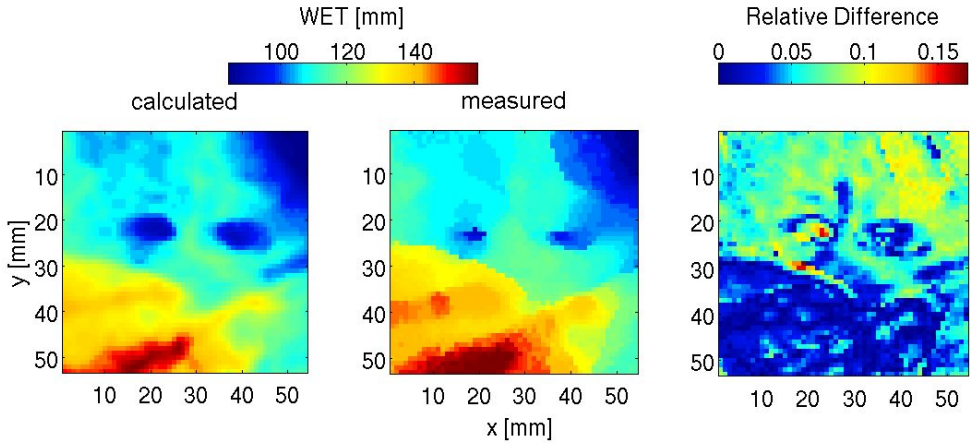

Figure 5.27: Region 2: Left: WET map calculated from CT data. Middle: Measured WET distribution with carbon ions. Right: Relative difference between the calculated and measured WET distribution.

tively. The measured and calculated WET maps agree well. In region 1 larger relative differences between the measured and calculated values occur in an area below the upper boney structure. The frozen sample started to melt during the ≈4 h long measurement. This caused geometrical changes. Region 1 included the pig ear (see figure 4.9), which flapped down during the melting process. This might be the reason for the large systematic deviations in the described area in region 1. Further deviations occur at steep gradients due to difficult reproducibility of positioning of the biological sample. On the CT couch the pig head was aligned at the laser cross. However, the CT coordinate system does not necessarily match the coordinate system in the experimental room at HIT, which results in systematic positioning errors. Further, at steep gradients where material interfaces are encountered by the traversing particles, Bragg-peak degradation takes place due to multiple Coulomb scattering (section 2.1.2). The degradation of the peak is not incorporated in the water equivalent range concept and neither in the treatment planning algorithm. Thus the calculated and measured WET values do not agree when multiple Coulomb scattering degrades the Bragg peak. This is further discussed in the next section.

The result obtained for region 2 also agrees well with the calculation. The relative difference map shows the same characteristics as for region 1 with differences of up to 15 % at high gradients only. The two small central structures given by the cavities are slightly decreased in size in the measured WET map in comparison to the calculated WET map. This is only one example for the in general measured decreased WET gradients. The reason is investigated in detail in the next section.

Despite the encountered problems with the melting of the sample and the difficult positioning, for both regions more than 90 % of the pixels lie within a 10 % relative deviation.

The usefulness of the range shifter for dose reduction in WET measurements was investigated for the biological sample. The WET distribution with the range shifter was measured with the proposed WET measurement technique at higher energies and additional subtraction of the water equivalent thickness of the copper stack value $\mathrm{WET}_{\text{r-shifter}}$=72 mm. Region 1 was measured with and without the range shifter without repositioning at a comparable melting stage of the frozen pig head. The results are presented in figure 5.28. The WET map obtained with the range shifter (middle) shows some deviations on the left side (dark red) in comparison to the WET map measured without range shifter. This is an artifact resulting from the decreasing beam width with increasing beam energies. The covered region of the pig head for higher beam energies was slightly smaller in contrast to the lower energies. Thus, at the outer boarder the statistical fluctuation increases which leads to uncertainties in the WET measurement. By adjustment of the irradiation field size and smaller distances between single spots, this effect can be overcome. However, not only the FWHM of the beam

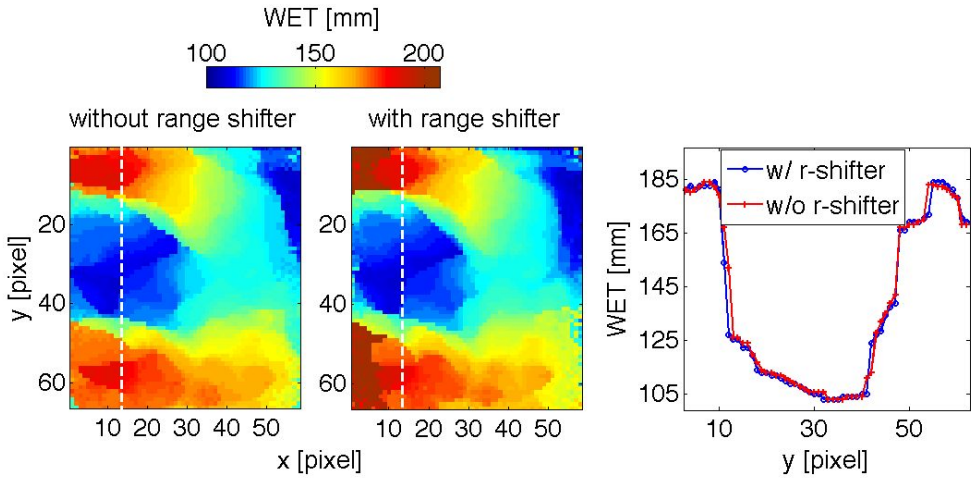

Figure 5.28: WET measurements of region 1 carried out without and with range shifter. Left: WET map measured without range shifter. Middle: WET map measured with the range shifter. Right: WET distribution comparison along the dashed white line.

spot decreases with higher energies but also the step size between the energies increases from 1 mm WET to 1.5 mm WET. This feature of the accelerator further limits the WET resolution of the proposed energy scan method. As an example, one profile (indicated by the white line) for the WET measurement of the frozen pig with and without range shifter is plotted in figure 5.28 (right). Despite the reduced WET resolution in the image obtained with the range shifter, only minor differences in comparison to the image obtained without the range shifter occur, which are due to the change in energy step width. Overall, the WET images agree very well within 1 %, neglecting the area on the left side where the peak determination of the energy scanning method failed due to insufficiently low particle fluence.

In order to further investigate the encountered differences between the measured and calculated WET distributions, the proposed method was carried out with an anthropomorphic head phantom as presented in the next section.

5.4.3 Anthropomorphic Phantom

As seen in the previous section, frozen samples can undergo geometrical changes during the melting process. To verify if the differences are caused by geometrical changes and multiple Coulomb scattering, rather than by the energy scan method itself, an anthropomorphic head phantom was investigated. Fixed geometry and composition of tissue equivalent materials allow to accurately measure the WET of the phantom. Further, the phantom's patient realistic head geometry allows to accurately position the imaging object with a thermoplastic head mask in the CT unit and on the treatment

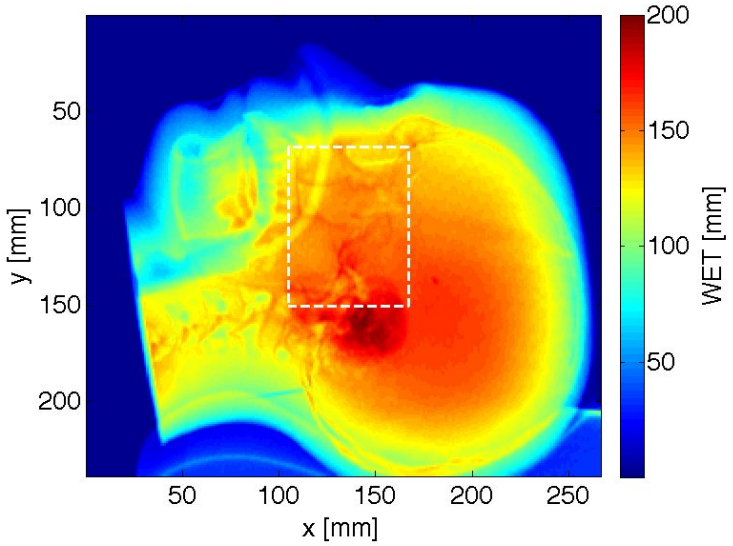

Figure 5.29: CT-WET map of the anthropomorphic head phantom calculated by a transformation of the CT image. The white dotted line indicates the area of interest.

couch within 1 mm accuracy. In doing this, the complete patient treatment planning workflow was mimicked with the anthropomorphic head phantom, see section 4.4.3.

The WET distribution was measured with the flat-panel detector and the developed energy scan method. In preparation for the measurements, the CT image of the anthropomorphic head phantom was transformed into the water equivalent system with the Hounsfield look-up table and summed up in beam direction to yield WET values, see figure 5.29. An area of interest indicated by the white rectangle was investigated in detail. This area includes mainly skull base, part of the jaw and the eye-socket. It was chosen, because of its very fine WET structures and high gradients.

Figure 5.30 shows a comparison of the measured WET image and the calculated CT-WET image (standard method). The measured values are in good agreement with the CT-based calculation, see figure 5.30 (right). More than 94 % of the pixels have a relative deviation of less than ±5 %. Differences between both WET images occur mainly at steep WET gradients. This results in an apparent distortion of the measured WET image. For example, the nasopharynx region with lower WET values indicated by the arrows seems to be significantly narrower in the measured WET map in comparison to the CT based calculation. Similar effects have been already observed for the WET measurement of the frozen pig, see figure 5.26 and 5.27. Understanding of these measured differences was gained, investigating the measured peak shapes of the signal to energy curve obtained with the flat-panel detector for each pixel. Figure 5.31 (left) shows the exemplary signal to energy curve of four pixels across the discussed region of the nasopharynx as indicated in figure 5.30 (middle). Bragg peak degradation, as seen in the signal to energy distribution (figure 5.31 (left)), occurs due to heterogeneous

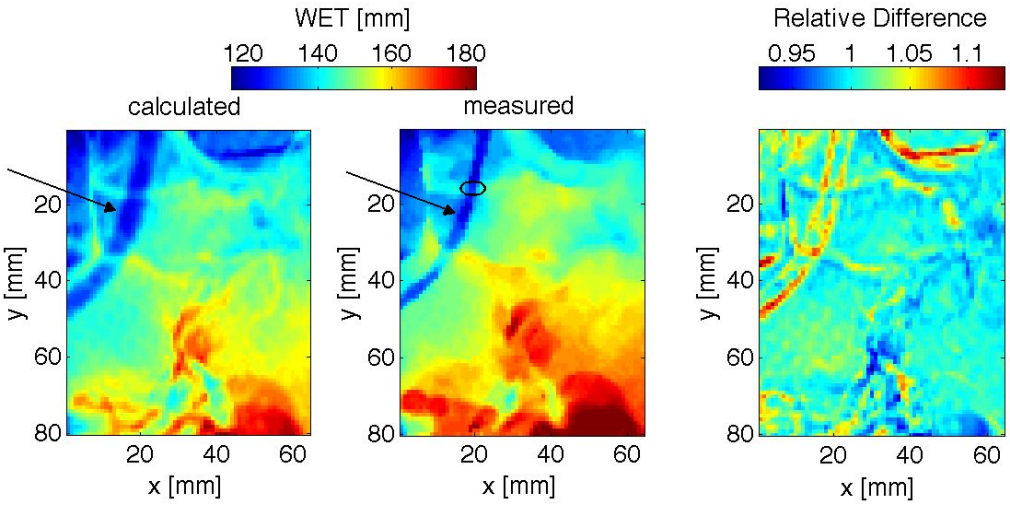

Figure 5.30: For comparison, the calculated WET image obtained from the CT data is shown on the left side and the measured WET map is presented in the middle. Occuring differences are indicated by the arrow. In the measured WET map a small region of pixels is indicated for which the signal-curves are analyzed in detail in figure 5.31. Right: Relative difference between the calculated and measured WET images.

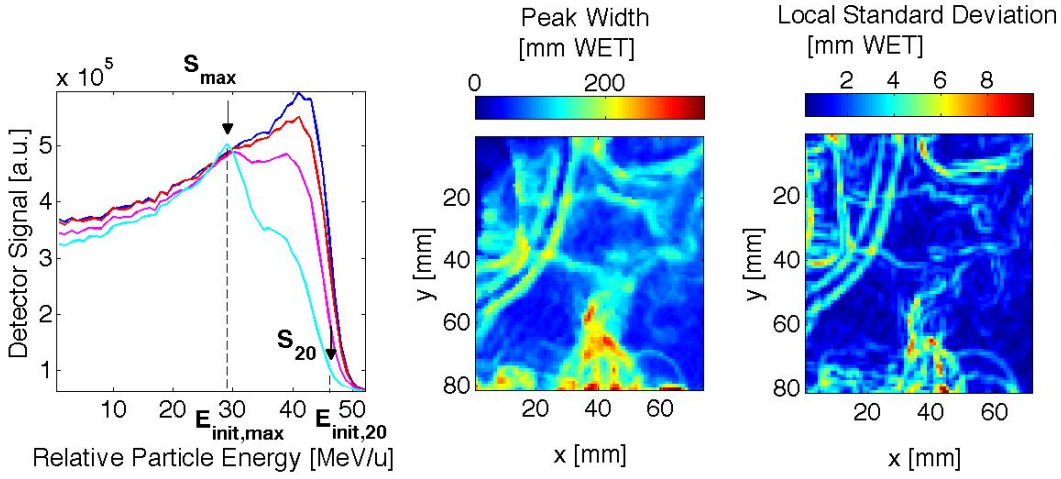

Figure 5.31: Left: Signal-energy curve for four pixel across a steep gradient. Peak degradation and even peak split-up occurs. Middle: Measured peak width. The width is estimated by the distance between the E_{100} and E_{20} and calculation into WET. Right: For comparison, the local standard deviation of the calculated WET image is plotted, where each pixel contains the standard deviation of the 3-by-3 neighborhood around the corresponding pixel of the calculated WET map.

overlying materials in beam direction. In the proposed technique, the WET value is given by the signal peak position. The measured values derivate from the CT-WET values. The transformation of the CT image into the water equivalent system assumes for each single CT voxel a homogenous material, although the CT numbers reveal only average photon attenuations, see also section 2.1.1. This method presents for most cases a good WEPL estimate. However, at material interfaces where scattering of the particles through different materials can cause severe Bragg-peak degradation, deviations are likely to occur.

In order to quantify the occurring differences between the measured and calculated WET values, the measured peak width and the local standard deviation of the calculated WET map are shown in figure 5.31 (middle and right). The measured peak width is defined by $d_{\text{peakwidth}} = (E_{\text{init},100} - E_{\text{init},20})$ with $E_{\text{init},20}$, the initial particle energy corresponding to 20 % of the detected peak signal. This difference in energy is recalculated into a difference in WET as plotted in figure 5.31 (middle). The comparison of the measured peak widths and the calculated local standard deviations in WET shows a clear correlation. As expected, at steep WET gradients represented by the local standard deviations, multiple Coulomb scattering leads to increased Bragg peak degradation.

With this knowledge, the WET measurements carried out with the energy scan method can be used to study ion range variations due to inhomogeneous interfaces parallel to the beam by visualization of the measured peak width. The overall agreement was studied by building difference maps. To exclude the discussed effect of inhomogeneities, the measured pixels with large peak degradation ($d_{\text{peakwidth}} > 10\,\text{mm}\,\text{WET}$) were neglected from the difference map. Further, calculated WET values above and below the maximum and minimum measured WET respectively (WET_{min} : 125 mm; WET_{max} : 170 mm; circled in figure 5.30) were excluded from the evaluation. These limitations were given by the chosen energy range used for the energy scan measurement. For visualization, all excluded pixels were marked in white in figure 5.32 (middle). After exclusion of these pixel only 53 % of the original pixel were left for evaluation. The histogram in figure 5.32 (right) shows that after exclusion of the pixels, the measured and calculated WET maps agree very well. 92 % of the measured pixel lie within ±2 % of the calculated WET values. For comparison the mean values and the standard deviations of the relative WET difference before and after exclusion are listed in table 5.4.

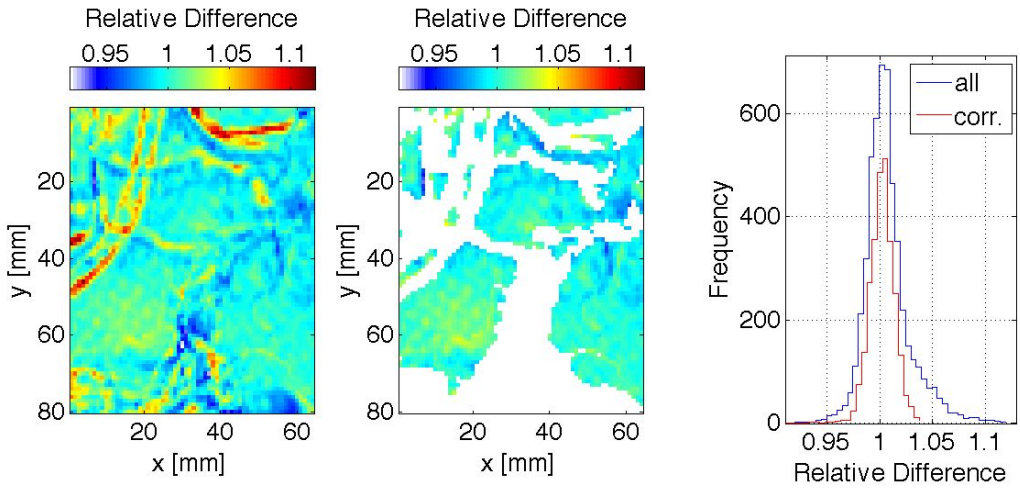

Figure 5.32: The occurring differences between the measured and calculated WET images are analyzed. This method allows to detect uncertainties in the treatment planning algorithm. Left: Relative difference between the measured and calculated WET map. Middle: For a realistic comparison the areas in the difference map where Bragg-peak degradation takes place are excluded from the analysis. Right: The histogram of the difference map shows that the areas of the measured and calculated WET map after pixel exclusion agree very well.

Table 5.4: Overview of the relative differences between the measured and the calculated WET image of the investigated area of the anthropomorphic head phantom.

	Relative Difference	
	Mean	Std.
Complete area	1.0044	0.0217
Corrected area (53 % remaining)	0.9997	0.0117

5.5 Carbon Ion Computed Tomography

Carbon ion computed tomography would in principle allow to measure distributions of the water equivalent path length (WEPL) of complex imaging objects. In analogy with an X-ray CT, this is done by measuring the water equivalent thickness (WET) of the imaging object for many rotation angles, representing single projections. The reconstructed image should yield information about three-dimensional WEPL distribution also for objects where the standard method of X-ray CT transformation through the Hounsfield look-up table tends to be inaccurate. However, ion scattering can lead to image blurring. For protons, image quality is improved by reconstruction with the most likely path (MLP) algorithm. In the case of heavier particles like carbon ions, scattering corrections are assumed to be negligible due to less multiple Coulomb scattering.

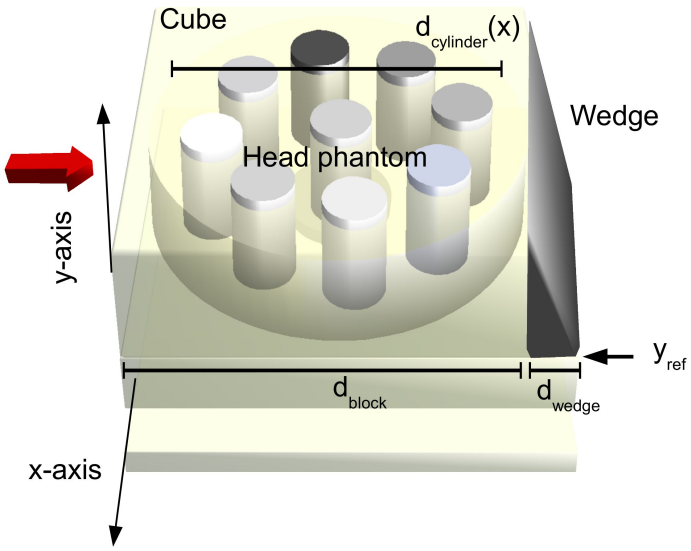

Figure 5.33: Schematic drawing of the measurement setup used for tomographic imaging with the flat-panel detector. The PMMA head phantom is placed in a cubic PMMA block to accelerate image acquisition. A static PMMA wedge (right side) is used to vary the energy in y-direction. A geometrical reference for calculation of the wedge thickness at any point in y direction is given by y_{ref}, the location of a small air gap between the bottom side of the wedge and the table.

The cylindrical PMMA head phantom equipped with tissue equivalent inserts was radiographed with carbon ions for tomographic imaging with the flat-panel detector. In contrast to the energy scan method, as discussed in the previous sections, for tomographic imaging the setup was modified to accelerate the imaging process. In this modification the phantom symmetry was exploited by embedding the cylindrical phantom in a PMMA cube and placing a static PMMA wedge in front of the detector. This wedge was used to passively modulate the given carbon ion beam energy across

the phantom, replacing the energy scanning from the accelerator. Therefore with this setup, a field of $x \times y\,[\mathrm{cm}^2]$ was irradiated with only one primary energy to measure the WET distribution. Tomographic imaging was carried out by rotation of the cylindrical head phantom in the reference system of the PMMA cube and wedge (figure 5.33). For more details see section 3.5.1. Each measured projection (example shown in figure 5.34

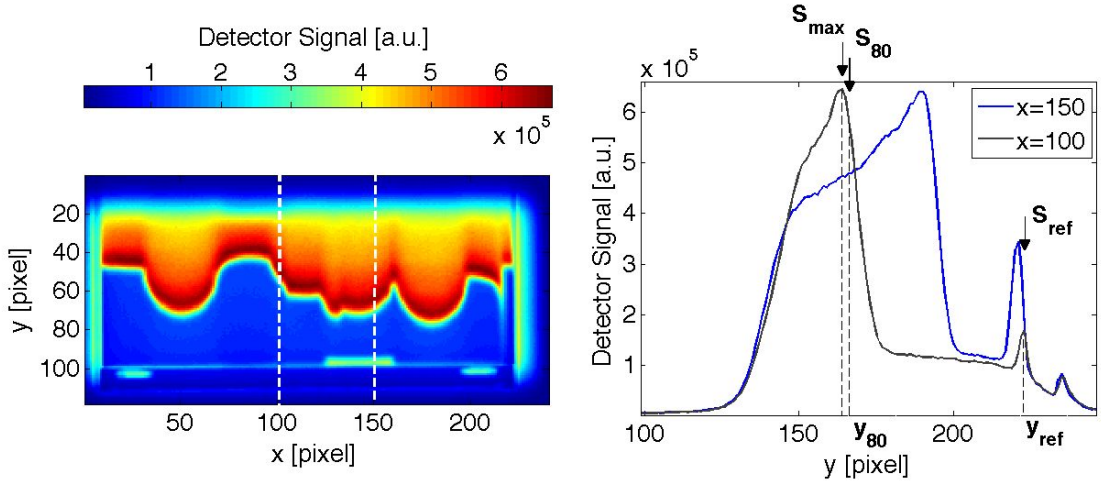

Figure 5.34: Left: Flat-panel signal image of the phantom setup for one projection. The signal distribution along the y-axis can be calculated into a WET value. Right: Profiles along the white lines. The signal peak position is given by y_{80} at 80 % of the peak height. A geometrical reference for calculation of the wedge thickness at y_{80} is given by y_{ref}, the location of an air gap in the phantom setup.

(left)) represents in y direction the measured wedge-modulated signal to energy curve for a given position x. The wedge thickness increases from top to bottom forming the characteristic signal curves which were used as replacement for the signal-to-energy curves measured in the previous WET experiments (figure 5.34 (right)). The WET value is given by the position of the maximum signal S_{max}. The position is calculated by the distance in y direction to the reference position y_{ref} (air gap) with known wedge thickness d_{wedge}. To increase the WET resolution, which is given by the slope of the wedge (19.57°), the steep fall-of of the peak dominated by the wedge geometry is used to determine the peak position at 80 % of the peak height.

The measured WET for a certain position in x is then given by:

$$\mathrm{WET}(x) = \mathrm{WET}(E_{\mathrm{init}}) - \tan(19.57°) \cdot (d_{\mathrm{wedge}} - (y_{\mathrm{ref}} - y_{80}) \cdot 0.8) \cdot \mathrm{WEPL}_{\mathrm{PMMA}} \quad (5.9)$$

with $\mathrm{WET}(E_{\mathrm{init}})$ being the water equivalent range of the particles of initial energy E_{init}, $\mathrm{WEPL}_{\mathrm{PMMA}}$ the water equivalent path length of PMMA, and 0.8 the conversion factor from the detector pixel size to mm.

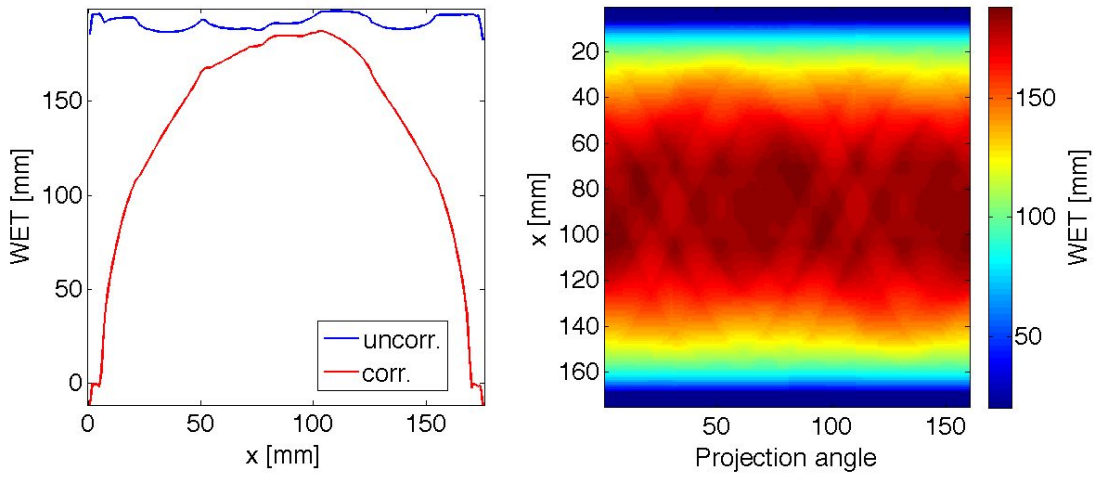

Figure 5.35: Left: Measured WET distribution in blue and the geometrical corrected distribution in red. Right: Final sinogram of the measured data.

The resulting WET distribution for the measurement at 0° is shown in blue in figure 5.35. Further, the known geometry of the PMMA cube with a side length of d_{block} and a cut out the size of the cylindrical phantom $d_{\text{cylinder}}(x)$ allows to recalculate the WET distribution of the cylindrical PMMA phantom:

$$\text{WET}_{\text{corr}}(x) = \text{WET}(x) - (d_{\text{block}} - d_{\text{cylinder}}(x)) \cdot \text{WEPL}_{\text{PMMA}}. \tag{5.10}$$

The final WET distribution $\text{WET}_{\text{corr}}(x)$ with the characteristic steep gradient on the left and right side, which is due to the shape of the cylindrical object, is indicated in red in figure 5.35.

The setup was imaged for 80 angles in steps of 2.25° over 180°. Calculation of the WET_{corr} distribution for each rotation angle forms the columns of the sinogram (figure 5.35, right). It is used as an input parameter for the filtered back-projection algorithm (section 3.5.1).

Figure 5.36 shows the resulting reconstructed WEPL image of the cylindrical PMMA head phantom (left) and the known insert WEPL values (table 3.2) in known phantom geometry (right). The overall reconstructed phantom shape with the inserts is in excellent agreement with the given geometry. Due to the reconstruction with a limited number of angles, streaking artifacts can be seen. The quantitatively measured WEPL values were analyzed by averaging the WEPL values of the tissue equivalent inserts over an area of 1.6 cm in diameter. The measured WEPL values from the reconstructed image were plotted against the known WEPL values as shown in figure 5.37. The obtained data was linearly fitted (red) and shows in comparison to the expected values (black line) a systematic shift in WEPL of -0.007. The measured WEPL values seem to be lower than the known WEPL values.

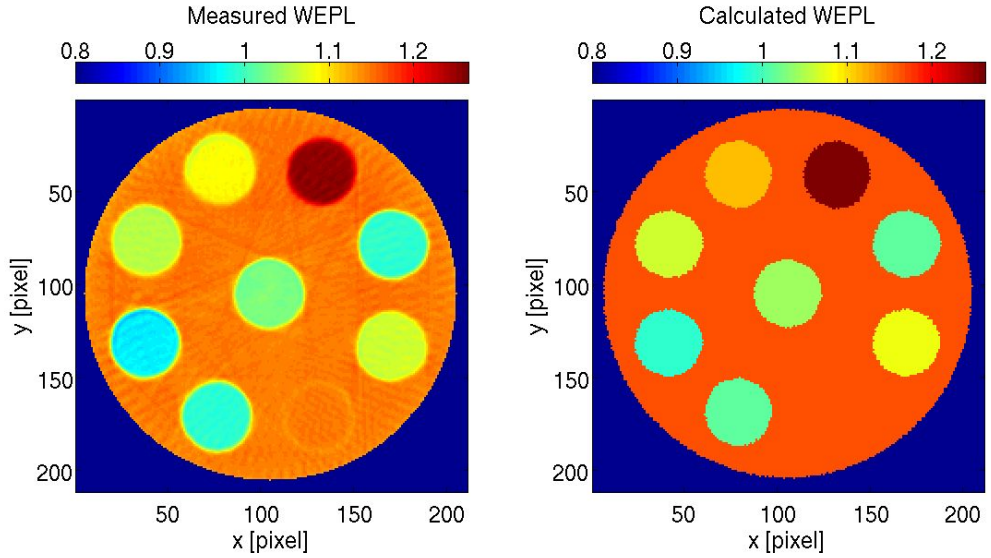

Figure 5.36: Left: Reconstructed WEPL image of the phantom. Right: Expected WEPL image.

The Ram-Lak filter used in the back projection algorithm is designed to cut-off high frequencies above a set threshold. This filtering process can lead to decreased values in the position space. To account for this, scaling of the obtained data is necessary. In X-ray CT imaging this is performed by applying a linear transformation called Hounsfield scale (equation 3.1). Here, for the reconstruction in carbon ion CT, a scaling factor was obtained by comparison of the measured WET values of a single projection with the WET values obtained from the reconstructed image. In figure 5.38 (left) the measured WET distribution for one projection is compared to the calculation from the reconstructed image. Clearly the noise originating from the reconstruction process can be seen. The reconstructed image underestimates the measured values. By multiplication with an estimated correction factor, both distributions agree well. This correction factor was found to be valid for all measured projections and WET distributions. Applying this correction factor to the obtained reconstructed WEPL values (figure 5.38 (right)), the reconstructed and expected WEPL values agree within one standard deviation.

The resolution of the reconstructed WEPL image is given by the standard deviation of the WEPL values shown in figure 5.38 (vertical bars). The resolvable difference in the WEPL image corresponds to twice the standard deviation given by the fit. The WEPL resolution in the reconstructed carbon ion CT image is better than 0.01 WEPL.

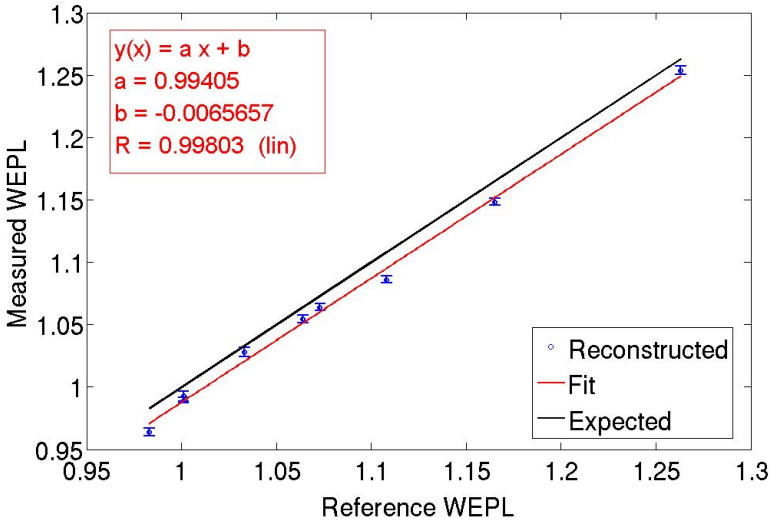

Figure 5.37: The WEPL values of the tissue equivalent inserts have been evaluated by calculating the mean and the standard deviation of ROIs placed over the inserts in the WEPL image. The reconstructed WEPL values are plotted against the expected reference values and are linearly fitted with the figure of merit given by the Pearson's correlation coefficient R.

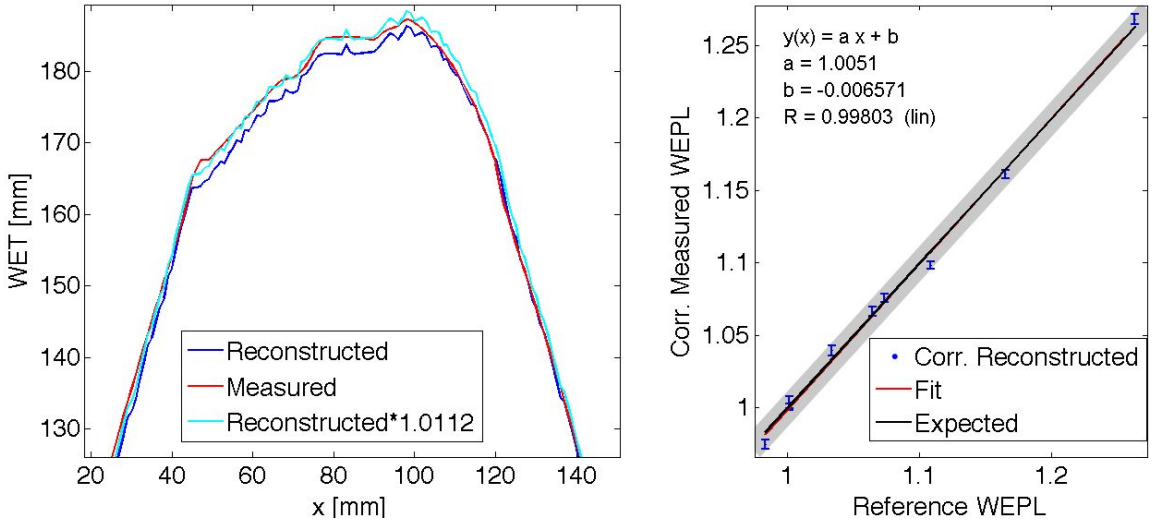

Figure 5.38: Left: Exemplarily for one projection angle, the measured and reconstructed WET values are plotted. The reconstruction underestimates the WET values by a factor of around 1.0112. Right: The correction factor was used to scale the reconstructed WEPL values. The corrected reconstructed WEPL values were fitted (red). The fit lies on top of the expected values (black). The gray band indicates the standard deviation of the reference WEPL values.

6 Discussion

6.1 Characterization of the Detector Response

Previous studies by Martišíková (2010); Hartmann et al. (2012); Martišíková et al. (2012b) investigated the detector response to ion irradiation. Based on this knowledge, further flat-panel detector characteristics relevant for ion radiographic imaging were studied.

The comparison of experimental results and MC simulations showed that the response of the flat-panel detector to ion irradiation is signal dominantly generated in the scintillator. Recent investigations of flat-panel detectors in proton beams by cooperation partners at HIT confirmed this result. Horn (2011) compared the response of a scintillator-based indirect flat-panel to a direct flat-panel detector (without scintillator). Under the assumption that the diodes fabricated in the two detector models are similar, their study concluded that about 98 % of the detector signal was produced in the scintillator and approximately 2 % of the signal was generated directly in the diodes.

Additionally, signal quenching of the detector was investigated and found to be strongly dependent on the particles' LET (figure 5.2). It is assumed that the increasing ionization density along the particle track leads to the recombination of electrons and electron holes in the sensitive volume and underestimation of the particle energy loss (Butts and Katz, 1967). For carbon ions, the detector response is lower than the assumed particle energy by a factor of 2-3 in the high LET region of the Bragg-peak (section 5.1.2). This strong signal quenching in the high LET region of carbon ion beams directly impacts the shape of the measured depth-signal curve. When employing the detector for ion radiographic imaging, this effect leads to a degradation of the image contrast. Despite the peak deformation, the Bragg peak position in depth can be determined by the flat-panel detector with an accuracy of 1 mm water equivalent thickness, as it was shown in this thesis. This is the basis for successfully implementing the water equivalent thickness measurement technique called energy scanning, in which particle energies are varied for each spot.

6.2 Image Processing

Image processing is used to improve signal quality. The routine presented in this thesis is technically consistent with a dark image correction and a pixel sensitivity correction. In order to determine image influencing parameters, the dark image behavior of the detector was studied. Small deviations between dark images in the order of 0.1 ‰ were found during the detector's heating up process (figure 5.4). Additional differences in the dark image between the two signal amplifiers that divide the detector in half (figure 5.5) were found to be in the same order. Also the dark image noise depends on the detector region (figure 5.6). Noise increases along the read-out lines away from the electronics, probably due to signal leakage in the capacitors.

In photon imaging small changes in the dark images are negligible. However, in the case of long lasting scanned ion irradiations of up to 12 min (≈9000 frames) these effects can sum up to a significant amount of up to 4 %. The aim of this thesis is to reach high contrast images. Thus, a newly developed active dark image correction routine was implemented in the offline image processing routine (Hartmann et al., 2012). The idea of this study is to use the irradiation-free time in between particle spills to regularly correct dark images every 5 seconds by taking image lag into account; see section 5.2.2.

The feasibility of pixel sensitivity correction procedures for application to ion imaging was investigated, resulting in a newly developed pixel sensitivity correction published in Hartmann et al. (2012). The pixel sensitivity matrix was acquired in ^{60}Co photon irradiation. The detector signal is linear to the number of impinging radiation quanta over the dynamic range and is dose-rate independent. This allows for an application of the correction matrix independent of the radiation modality. So far, the correction matrix has not shown any significant changes while applying it to ion images. Nevertheless, sensitivity changes of the pixels can occur due to radiation damage in the read-out electronics, diodes or the scintillator. Therefore, it is advisable to control the flat-panel detector radiation response with reference to the radiation of ^{60}Co on a regular basis.

The pixel sensitivity correction excellently improved the detector image's quality up to 9 % (figure 5.8). The correction technique was also exploited by other authors for other flat-panel detectors as presented in Horn (2011) and is essential for the application of the detector in the QA procedures at the HIT facility.

Combined, both image corrections are included in the newly developed image correction routine as published in Hartmann et al. (2012) (see section 5.2.4). The routine is implemented to be automatically applied offline.

6.3 Ion Radiographic Images

6.3.1 Spatial Resolution

The spatial resolution for the different radiation modalities (protons, carbon ions and photons for reference) was compared by determining the modulation transfer function. The MTF was measured using the tilted-edge method. The measured reference spatial resolution for ^{60}Co photons (figure 5.10) was found to be comparable with former measurements obtained with the same detector (Partridge et al., 2002) within 0.02 mm^{-1} at $\mathrm{MTF}_{50\,\%}$. Ion radiographic spatial resolution has shown itself to be higher, in comparison to photons, and was highest for carbon ions. This was expected, because heavier particles scatter less. Even in mixed particle fields, which are encountered in carbon ion radiographic imaging, carbon ions are expected to play the dominant role in terms of energy deposition. In the depth of the Bragg peak at $\sim$15 cm, the fluence of primary carbon ions reduces to about one half, but the primary ions account for more than 90 % of the deposited dose.

Also, the spatial resolution of the imaging system depending on the orientation to the pixel matrix was investigated. The $\mathrm{MTF}_{50\%}$ in read-out direction dropped in comparison to the $\mathrm{MTF}_{50\%}$ perpendicular to read-out for carbon ion and proton images by 12 % and 25 %, respectively (figure 5.10 (right)). This is assumed to be probably due to signal leakage along the read-out lines as described in Martišíková et al. (2012b).

The anisotropic response of the detector and the dependence of the MTF on the particle type, particle energy and composition and geometry of the imaging object do not allow to use the measured MTF to deconvolute the response of the imaging system in a straight-forward way.

6.3.2 Soft Tissue Contrast

The soft tissue contrast in ion radiographs was qualitatively investigated by imaging a biological sample. In the proton radiographs the contrast dissolved fine structures of the knuckle of pork; see figure 5.12. A comparison of the proton radiograph with the calculated CT-WET image showed that the overall shape and structures of the knuckle are in agreement. However, the image information in the proton radiograph is not only given by differences in energy deposition of the particles, but is also affected by the distortion of the lateral particle equilibrium leading to the e.g. peripheral high signal halo. Due to the shape of the Bragg peak, the measured energy loss of the particles can not be unambiguously correlated to the traversed water equivalent thickness. The different nature of particle and photon interaction with matter makes the high image contrast, given in ion radiographs, unique, and incomparable to X-ray radiographs.

Carbon ion radiography of the knuckle resulted in low image contrast due to inho-

mogeneities in the particle fluence of around 5 %[1] and signal quenching (figure 5.11). This is a very important aspect to consider when employing the flat-panel to conduct ion radiography. Since the detector measures the integrated signal of the particle energy loss without information about the particle fluence, the quality of the obtained radiograph is correlated to the homogeneity of the delivered fluence by the accelerator. To optimize the irradiation field in terms of homogeneous fluence, raster scanning at HIT was carried out in the following experiments with large beam spot foci and small distances between the individual raster spots. A passive beam delivery would lead to improved results.

Quantitative soft tissue contrast measurements were carried out with tissue equivalent materials: see section 5.3.2. By choosing the energy in accordance to the detector placement in the steep rising oder descending gradient of the Bragg peak, the soft tissue contrast in the ion radiographs allows to differentiate between all soft tissue equivalent materials. For small imaging objects, up to a few centimeters, the contrast in the carbon ion radiographs is reduced in comparison to proton radiographs due to strong signal quenching by a factor of 2-3 in the peak region. Increasing the object's thickness severely reduces the contrast of proton radiographs due to increased multiple Coulomb scattering. In this case carbon ion radiography is favorable.

It is eligible to compare the reached contrasts to X-ray CT soft tissue contrast. To quantify the obtained image qualities, the contrast-to-noise ratios (CNR) are calculated and compared. Here, the CNR for a given object x with respect to solid water (SW) is defined as:

$$C = \frac{|S_x - S_{\mathrm{SW}}|}{\sigma_0} \tag{6.1}$$

where S_x and S_{SW} are signal values for the object x and solid water and σ_0 is the standard deviation of the image noise. As an example, the contrast-to-noise-ratios for muscle and liver to solid water were calculated for X-ray CT images (values taken from table 3.2) and the obtained proton and carbon ion radiographs. The comparison of the calculated CNR and the image doses are summarized in table 6.1. The image noise σ_0 was calculated as the average noise in regions of interest placed over the inserts.

The measured image quality of the proton radiograph at a lower dose is a factor of 1.5 (muscle) and 2.3 (liver) higher than the CNR found in X-ray CT images. For the carbon ion radiograph, the CNR is comparable to the X-ray CT values. The high ionization density of low energetic carbon ions (initial particle energy 88 MeV) led to strong signal quenching. The dose was not optimized and resulted in around 100 mGy. Higher energies should be employed for radiographic imaging with carbon ions to improve image quality. Thus, using a high density range shifter placed between

[1] The medical accelerator at HIT is optimized for dose delivery. 5 % fluence inhomogeneity is in agreement with the specification and will result in only a small deviation in dose due to interplay effects over the treatment duration.

Table 6.1: Contrast-to-noise ratio of given insert to solid water; comparison between CT image, proton radiograph (48 MeV) and carbon ion radiograph (88 MeV). Uncertainties are calculated with propagation of uncertainties.

Insert	Contrast-to-Noise Ratio		
	X-ray CT image (≈ 60 mGy) (Shrimpton et al., 2003)	Proton Radiograph (≈ 20 mGy)	Carbon Ion Radiograph (≈ 100 mGy)
Muscle	5.7 ± 0.6	9.3 ± 0.3	3.7 ± 0.4
Liver	12.7 ± 0.5	30.7 ± 0.4	15.4 ± 0.4

imaging object and detector has the potential to enhance image quality.

This study on tissue contrast between ion radiography and X-ray CT does not present an ideal comparison, because two-dimensional ion radiographic imaging was compared to three-dimensional sectional X-ray CT imaging. However, the study gives a good impression of the high image quality obtained in ion radiography. The following section will continue to discuss the comparisons between the two radiation modalities under the aspect of mammography.

In general, ion radiography with the flat-panel is strongly dependent on the matching of object thickness and particle imaging energy accordingly. The energies of the HIT accelerator are given in discrete steps corresponding to 1 mm range difference in water. These steps inherently result in uncertainties between the calculated and available particle energy. Thus the detector might measure the signal in the gentle gradient before the Bragg peak, which decreases the contrast in the ion radiographs. Such a limitation could be overcome by varying the energy with a passive energy modulator (Muraishi et al., 2009).

6.3.3 Evaluation of the Potential for Mammography

The applicability of the flat-panel detector in combination with ion imaging for mammography was investigated in detail. To optimize the dose, the employment of a high density range shifter was studied.

The spatial resolution of a state-of-the-art mammography system, which consists of a low energy photon source and a complementary a-Se detector, was compared to the performance of the flat-panel detector in ion beams (figure 5.17). The measured MTF of the Mammomat ($MTF_{50\,\%}$ =4.70 mm^{-1}) imaging system is consistent with values given in literature ($MTF_{50\,\%}$ =4.86 mm^{-1}): see Marshall et al. (2011). Due to the small pixel size of the Mammomat detector, the spatial resolution of the images ($MTF_{50\,\%}$)

is a factor of about 9 higher in comparison to the flat-panel measurements. After rebinning of the Mammomat images to match the flat-panel pixel size, the resolution of the images is comparable to the carbon ion radiographs. Due to reduced scattering the spatial resolution is better than in the proton radiographs. The relatively high spatial resolution of this X-ray imaging modality is reached by the implemented scatter grid and photon scatter corrections.

Soft tissue contrast of the mammography, and the corresponding ion radiographic images, has been evaluated (figure 5.19). The obtained image qualities can be compared quantitatively by the contrast-to-noise ratios, which are shown in table 6.2. The

Table 6.2: CNR of given insert to solid water; comparison between mammography and ion radiography. The biological doses for the images were calculated in table 5.3 (Mammograph: (7.23 ± 1.30) mGy, Carbon ions: (4.94 ± 9.96) mGy, Protons: (2.05 ± 0.30) mGy).

	Contrast-to-Noise Ratio		
Insert	Mammograph	Carbon Ion Radiograph	Proton Radiograph
Muscle	≈11	≈15	≈17
Liver	≈17	≈51	≈52

contrast-to-noise ratio for the proton radiograph has increased by a factor of 1.5 and 3 (muscle and liver respectively) in contrast to the mammography, which has a factor of 3 higher biological dose. The uncertainty of the biological carbon ion dose calculation is too high to draw conclusion on the image dose in comparison to the mammograph.

Mammography employs low energy photons of around 30 kVp because in this energy range the photoelectric interactions predominate over Compton interactions and give rise to a high contrast proportional to $Z^{3\text{-}4}$. The investigated high-end mammography unit features contrast and dose improvement by automatically adjusting the photon energy to the imaging object thickness. Despite the Mammomat's optimized image acquisition, in this work it was shown that the image quality, in terms of contrast-to-noise ratio in ion radiographs with the flat-panel detector, can be improved by a factor of about 1.5 and 3 for muscle and liver, respectively (table 6.2).

The soft tissue contrast in the measured ion radiographs was higher in the carbon ion radiograph than in the proton radiograph (figure 5.19). This does not accord with the quantitative soft tissue contrast measurements from the previous section 5.3.2. Discrepancies result from the discrete energy steps given by the design of the accelerator, which shows again the limitation of this method. Small energy deviations have a tremendous effect on low particle energies (small imaging objects) because of their narrow Bragg peak. Image quality could be improved by a continuous range shifter.

The main concern studying ion radiography's potential for mammography is the

amount of applied dose. To achieve dose reduction, the particle fluence was decreased and a copper range shifter was employed (section 3.6). The corresponding biological dose for all three imaging modalities (carbon ions, protons and photons) was calculated. The biological dose of X-ray mammography was estimated to be about a factor four times higher than the biological dose of proton radiography. Carbon ion biological imaging dose was calculated to be a factor two times higher than the biological dose of X-ray mammography. However, the carbon ion RBE is calculated with large uncertainties, resulting in large uncertainties of the calculated biological dose. A dedicated irradiation study of breast cell cultures could present a direct comparison of the biological effectiveness of the discussed radiation modalities, avoiding model-based calculations.

Using protons for breast imaging could be beneficial due to the lower biological dose of a factor of four and higher soft tissue contrast in comparison to X-rays mammography. Having the mammography detector rebinned to the pixel size of the flat-panel, the spatial resolution of proton radiographs ($MTF_{50\,\%}$) was found to be 11% lower due to multiple Coulomb scattering of the particles. Since the MTF measurements of ions were carried out with the lowest available energies (section 4.3.1), increasing spatial resolution is expected for increasing particle energies due to less multiple Coulomb scattering of the particles. Optimization of the usage of a high-density range shifter complementary to the higher particle energy allows one to measure high soft tissue image contrast in the steep gradient of the Bragg peak with a decreased effect of particle scattering. In the case of mammography, the breast is compressed to an average of 4 cm. If the compression is carried out as well for ion radiography the water equivalent thickness of the breast would be known with high accuracy. This allows one to choose the imaging energy accordingly. The information might be used to deconvolute the detector signal with an energy-dependent kernel for particle scattering correction and improve image spatial resolution further.

Newly developed flat-panel detectors with a pixel pitch of ≈75 µm (Kagadis and Langer, 2011), an optimized irradiation setup and an appropriate ion scatter corrections, as discussed above, could present a solution for ion radiography, which is able to reach superior image information content in comparison to X-ray mammography.

Nevertheless, the mount of time needed for ion radiography is much more expensive than the use of the Mammomat unit. Recent developments and design studies of compact proton accelerators (e.g. super conducting synchrocyclotron (Mevion, 2011), dielectric wall accelerator (Poole et al., 2007)) might extensively reduce the cost of particle therapy units within twenty years.

6.4 Measurement of the Water Equivalent Thickness

The proposed measurement technique of water equivalent thickness by energy variation of the primary beam was in this work successfully applied to several phantoms with increasing complexity. The resolution of WET is predominantly limited by the discrete energy steps of the accelerator and was shown to be better than 1.5 mm WET. This resolution is already sufficient for therapy planning.

Unlike for ion radiography, previous knowledge of the water equivalent thickness and homogeneously irradiated fields are not necessary for this technique. The only requirement necessary, is the requirement that particle fluence has to be constant during the energy scanning process. This is with high accuracy given for the HIT accelerator.

Until now, WET measurements have been carried out with a peakfinder water column[2] as described in Karger et al. (2010). This device consists of a water column that has an adjustable length, and it contains ionization chambers in front of and behind it. These chambers measure the signal proportional to the deposited radiation dose. The peak finder has been designed for highest precision Bragg peak position detection. It integrates the signal laterally over the whole beam spot with a FWHM of at least 4 mm (carbon ions). It is suitable for WET measurements of homogeneous samples of a defined thickness, but this method does not allow to measure two-dimensional WET distributions at high spatial resolution in the order of mm.

The newly proposed flat-panel WET measurement technique consists of small pixel sizes, comparable to the dimensions of CT pixels. Also, it has a high measurement accuracy in terms of WET. This allows to measure the WET distribution of special cases, e.g. jaws with teeth and gold fillings. The dental fillings of head and neck patients can lie in the beam's path and critically distort the actual dose distribution. The impact of gold fillings on the ions' range is difficult to quantify with current methods. The proposed method could help to investigate differences in WET between the planned and actual distribution and to estimate the effect of dental fillings on dose calculation.

When investigating the applicability of an imaging modality for patient application, the imaging dose is an important quantity. For the WET measurements the dose was reduced by employing the range shifter. It was shown that the range shifter does not affect the accuracy of the WET measurement.

A fluence of at least 500 carbon ions/mm^2 per energy scan is needed to accurately measure the WET distribution (see section 5.4.1). This corresponds to a physical dose of ≈1 m Gray per energy slice, when employing the range shifter. For an energy scan of around 50 energies, as used for the experiments, this amounts to ≈0.05 Gray, which is in the order of the physical dose for a standard head CT scan (Shrimpton et al.,

[2]PTW Freiburg GmbH, Freiburg, Germany

2003). The biological effect of the energy scan is estimated to be larger than the X-ray CT scan. An idea to account for the dose of ion radiography is its incorporation into the patient dose calculation in the treatment plan. This is also done with daily patient CT scans along the therapy course, which sum up to doses of around 0.1 Gy. Furthermore, the spot scanning at HIT allows measurements of very small fields of $3\times3\,\mathrm{mm}^2$, enabling one to verify the WET of only single, most interesting and critical spots, while sparing surrounding healthy tissue.

Comparing doses to the current clinically standard methods shows that the proposed method is not ideal for patient imaging and requires some forms of modification. However, it is a powerful tool for testing and assuring the quality of the treatment planning algorithm. Studies on the anthropomorphic head phantom (section 4.4.3) showed the clinical relevance of the WET measurement method with the flat-panel detector. Firstly, it allows one to verify the treatment planning algorithm, especially the underlying HLUT. The WET distribution is calculated from the CT image by use of the Hounsfield look-up-table. This calculation forms the basis for the treatment planning algorithm. Comparing it to the measured WET, excluding the pixel with Bragg-peak degradation, allows one to detect uncertainties in the HLUT. Secondly, the measured Bragg-peak degradation, which can not be accurately predicted by the treatment planning algorithm, allows one to estimate uncertainties between the planned and actual dose distribution, as previously discussed in the case of dental fillings.

6.5 Carbon Ion Computed Tomography

The measurement of WET distributions for tomographic imaging with carbon ions was investigated. To accelerate the imaging process, the energy scan technique was replaced by the use of a static PMMA wedge, which functioned as a passive energy shifter. This significantly reduced the measurement time from about 20 hours to 6 hours in total. A high WEPL contrast of 0.01 WEPL was achieved in the reconstructed image at a total dose of about 8 Gray. This contrast corresponds to an improved ion range calculation uncertainty of about 1 % in comparison to the 2-3 % accuracy that using CT-based calculations ensures (Jäkel et al., 2001). The imaging dose needed for tomographic carbon ion imaging is 10^3 higher than that used in conventional X-ray CT imaging, making it unfeasible for patient imaging at the moment. Nevertheless, it presents a very accurate technique to access three-dimensional WEPL information, therefore assuring and improving the quality of treatment planning. Faster energy variation with for e.g. a moving passive range shifter as employed by Murashi et al. (2007), could reduce the long measurement time by a factor of around 5. Another advantage of the flat panel detector is its compact design, which allows one to integrate the detector into the ion gantry for a technically feasible tomographic imaging of phantoms.

7 Conclusions

This work has investigated the applicability of a flat-panel detector in ion radiography and tomography, constituting the first study on ion radiographic imaging with an amorphous silicon detector.

Studies on the characteristics of the RID256-L detector response for ion radiography have shown that the detector signal is dominated by the scintillators's response rather than the direct signal from the photodiodes. In high LET ion beams, and in the depths of the Bragg peak, signal quenching is found to decrease the signal. Especially for carbon ions, this decreases the Bragg peak's height and degrades image contrasts in the ion radiographs. Nevertheless, a determination of the peak position with an accuracy of 1 mm depth in water is feasible.

Following an extensive study on detector dark images and the influence of parameters on image quality, like the varying pixel sensitivity to irradiation over the detector, a new image correction routine was developed. This offline applied correction method significantly improved the quality of the acquired ion radiographs. For homogeneously irradiated proton and carbon ion fields the standard deviation improved by a factor of two. Other works have shown that the application of this image correction routine is essential when using the flat-panel detector for beam quality assurance (Hartmann et al., 2012; Hartmann, 2010) and patient plan verification (Martišíková, 2010).

The spatial resolution of the images obtained with the flat-panel detector and different radiation modalities was quantified by the modulation transfer function. Carbon ions are the supreme imaging modality due to decreased Coulomb scattering which limits spatial resolution in case of proton imaging. The $MTF_{50\,\%}$ of the proton and photon radiographs dropped 23 % and 45 % respectively in comparison to the spatial resolution of the carbon ion radiograph. The MTF was shown to be dependent on the direction with respect to the pixel matrix. In the read-out direction signal leakage degrades image quality. To limit interplay effects in scanned ion beams, scan direction was chosen to be perpendicular to the detector read-out direction.

The first radiographic images of a biological sample indicated a high soft-tissue contrast. To quantify the obtained contrast, measurements with soft-tissue equivalent materials were carried out. For a comparison with X-ray CT image quality, the contrast-to-noise ratio was calculated. The results showed that the soft-tissue contrast in proton radiographs can be twice as high at a factor three lower dose than as those

in the X-ray CT.

Mammography employs low energy photons for high tissue contrast imaging at the cost of high dose. A reduction of dose is desirable. Based on the obtained results, concerning the usage of the flat-panel for ion radiography, the potential for mammography was studied in detail. This work found that the performance of proton radiography can be better than a state-of-the-art mammography unit, under the assumption that the compared detector systems have the same pixel sizes. The dose applied for the proton radiograph was a factor of 3.5 lower, and the contrast-to-noise ratio was increased in contrast to the mammograph by a factor of about 1.5 and 3 for muscle and liver, respectively. However, a draw-back in proton imaging is the decreased spatial resolution of the images due to particle scattering. To be able to compete with X-ray imaging, improvement is necessary. For mammography the breast is compressed to a uniform thickness of a few centimeters. This might allow to implement ion scatter corrections dependent only on the breast thickness to deconvolute the measured signal and improve spatial resolution. Another possibility would be to use carbon ions instead of protons for imaging. This work has also shown that carbon ions have high potential for ion radiography. Due to reduced scattering of the particles the spatial resolution is high, and despite the signal quenching in the detector the tissue contrast is much higher than in the mammographs. However, the biological effect of carbon ion irradiation on breast tissue can only be estimated with large uncertainties, making it difficult to estimate the patient dose. The optimal beam modality might be an ion species in between the atomic numbers of protons and carbon ions, like helium ions, and has to be confirmed by further studies.

In order to verify and improve heavy ion therapy treatment planning algorithm it is desired to measure the differences between planned and actual water equivalent thickness of an object, e.g. a phantom. In this work a newly developed method for WET measurement, called energy scanning method, was investigated. The energy variation of the accelerator is employed to acquire a signal-to-energy curve with the flat-panel detector. The energy resulting in the maximal detected signal corresponds to the WET of the object. It was shown that this proposed method in combination with the flat-panel detector enables to determine the water equivalent thickness of the imaged object with an accuracy better than 1.5 mm WET. Application of the method allows to study range uncertainties for complex phantoms and use it to detect errors in the treatment planning algorithm. In contrast to the current standard WET measurement techniques (Karger et al., 2010), the two-dimensional WET maps are acquired here at a detector pixel size of $0.8 \times 0.8 \text{mm}^2$ over a large active area of $20 \times 20\,\text{cm}^2$. The dose needed for an energy scan of 50 energies (equivalent to a range of 75 mm WET) is around 0.05 Gray. For radiation therapy this dose could be incorporated into the treatment planning as it is conventionally done with X-ray CT images at HIT. Further,

spot scanning at HIT also allows to measure the WET of small areas of interest ($4 \times 4\text{cm}^2$), sparing surrounding healthy tissue.

Ion computed tomography as a basis for treatment planning could in principle eliminate the need for the ambiguous conversion from CT numbers to water equivalent path length. Therefore, the WET measurement technique was exploited to acquire a carbon ion computed tomography image. The reconstructed image showed high spatial resolution and high WEPL resolution of 0.01 WEPL, corresponding to an accuracy of 1 %. Due to the dose of about 8 Gy needed and the long measurement time of 6 hours, in this configuration the carbon computed tomography is not suitable for patient imaging. However, it provides a powerful tool for quality assurance by measuring very accurately the three-dimensional WEPL distribution in complex imaging objects.

So far, no significant radiation damage of the RID256-L fat-panel detector has been observed. It is resistant to moderate mechanical stress and very easy to handle due to its compact size. Simple operation and its low weight allows to mount it on the treatment table or on the ion gantry.

In this work it was shown that the flat-panel detector is feasible for ion radiography, WET and tomographic WEPL measurements. Increased potential due to lower dose is expected from new generations of silicon-based detectors.

8 Outlook

Recent Developments of Flat-Panel Detectors

The new commercially available models of a:Si-H flat-panel detectors have a higher spatial resolution given by a small pixel pitch of around 75 µm, faster read-out (≈ 30 fps) and larger sensitive areas (up to $40\times40\,\mathrm{cm}^2$) (Kagadis and Langer, 2011). For indirect detection systems a variety of scintillators are available. CSI is an excellent absorber of X-rays and has in combination with amorphous silicon the highest-rated photon detection efficiency in use today. Further the scintillator thickness can be optimized. In relation to the result that also in ion beams most of the signal is generated in the scintillator, a thick scintillator layer might increase the particle energy deposition. However, it can also degrade spatial resolution due to the spreading of the secondary photon cascade in the layer. The high numbers of possibilities for scintillator materials and thickness, and read-out diodes, might hold a combination which improves spatial resolution and contrast and reduces signal quenching of the detector in carbon ion beams. However, from the known material composition it is difficult to estimate the response of the detector in ion beams and thus further investigations are needed. Concerning this issues, it might be rewarding to investigate direct flat-panel detectors for ion radiographic imaging. A first characterization was carried out at the Heidelberg Ion Beam Therapy Centre (Horn, 2011) with an RID 512-400 Al1 model by Perkin Elmer (Wiesbaden, Germany). The signal quenching in high LET regions and long term radiation damage are going to be studied in the near future.

New Particle Detectors for Ion Radiography

High doses needed for high-quality ion radiographic images with the flat-panel detector result from the need of high particle statistic due to the lack of ability to recognize single particles. New detector types like the Medipix (Medipix, 2012) based on the CMOS read-out chip technology and crystalline-Si sensor are able to detect single particles in square pixel sizes of $55\times55\,\mu\mathrm{m}^2$(Vykydal et al., 2005). A recent development is the Timepix detector (Llopart et al., 2007), which evolved from the Medipix2 chip technology. Beneficial for ion radiography is the measurement of the energy deposition per ion and that multiple detectors can be stacked together to form parallel layers

(Sokup et al., 2011) which allows to measure the direction of the ions (Jakubek et al., 2011). As of today, a limiting factor when employing the Timepix/Medipix for imaging is its small active area of about $2\,\mathrm{cm}^2$. However, the technology to fabricate larger detectors is available (Tick and Campbell, 2011). With all those developments, the Timepix has the potential to measure ion radiography at significantly decreased dose in comparison to flat-panel detectors.

Acknowledgements

It is a pleasure to thank the numerous people who made this thesis possible:

First of all from the department of Medical Physics in Radiation Oncology of the German Cancer Research Centre, I especially thank:
Prof. Dr. Wolfgang Schlegel, head of the department and **Prof. Dr. Oliver Jäkel**, head of the heavy ion research group and my doctoral adviser. Throughout the last years he provided encouragement, sound advice and excellent teaching. His positive outlook and confidence in my research inspired me and gave me confidence. Most importantly, I wish to thank my supervisor **Dr. Maria Martišíková,** for her constructive criticism and comments from the initial conception to the end of this work. It was a pleasure working with her. I'm thankful to **Prof. Dr. Christian Karger** and **Prof. Dr. Hans-Christian Schultz-Coulon** (KIP) for willingly accepting to be TAC members. I highly appreciated their advices and the inspiring discussions.

I would like to thank **Andrea Schwahofer** for borrowing the phantoms and Gammex inserts and the medical engineering team of **Gernot Echner** and **Armin Runz** for the planning and optimization of the measurement setups, which were in-house workshop built with so much passion.

I am thankful to **Prof. Dr. Marc Kachelrieß** and his students for the discussion on computed tomography reconstruction. The **group members of E0409**, I am indebted to for providing a stimulating and kind environment which made it so much fun to come to work every single day. I am thankful to **B. Hesse**, who introduced me to the flat-panel in first place and helped me with the measurements of the first year and **B. Hartmann** and **L. Huber** who supported me during beamtime at HIT- physically and mentally.

A special thanks goes to **Dr. Stephan Brons** (HIT) for arranging and supporting the beam times- no matter when, during the night or on public holidays, he was always there or willing to help on the other side of the telephone. **Benjamin Ackermann** I wish to thank for all the fruitful discussions, the inside information to HIT and the help carrying out the anthropomorphic phantom experiment. Further, I wish to thank **M. Schenk** from the Kopf Klinik in Heidelberg, who was highly supportive and a great help performing CT measurements. For the measurement support at the Mammomat at the University Hospital in Heidelberg and the borrowing of the mammography phan-

toms, I thank **N. Grünfelder**.

On a personal level I would like to thank my family and friends for the amazing last three years;
A special thanks goes to "The Heidelberg Connection" (Maria, Julia and Sabrina) for all the fun time working out and awesome Thursday nights,
Peter and Felix for so much "quality time" at the Thursday lunches,
Daniel for everything, e.g. polishing this thesis- I can never ever make it up to you again-
and Kathi, a friend I can always count on no matter what.
I wish to thank my entire family; without their never-ending support and belief this thesis would not have been possible.
Lastly, and most importantly, I wish to thank my husband Matthias for all the patience and love!

Bibliography

Abe, S., Nishimura, K., Sat, H., Muraishi, H., Inada, T., Tomida, T., Fujisaki, T., Futami, Y., Kanai, T., Kawachi, K., and Tazawa, S. (2002). Heavy ion ct system based on measurement of residual range distribution. *Jpn. J. Med. Phys. Vol.22 No.1.* (Cited on pages 13 and 14).

Ackermann, B., Qamhiyeh, S., Ellerbrock, M., Geithner, O., and Jäkel, O. (2006). Stoichiometric calculation of the relation between carbon ion ranges and x-ray ct numbers. *Tagungsband DGMP.* (Cited on page 30).

Alderson, S. et al. (1962). An instrumented phantom system for analog computation of treatment plans. *Am. J. Roentgenol.* (Cited on page 28).

Amaldi, U., Biachi, A., Chang, Y.-H., Go, A., et al. (2010). Construction, test and operation of a proton range radiography system. *Nuclear Instruments and Methods in Physics Research A.* (Cited on pages 2 and 15).

Antonuk, L. et al. (1990). Radiation damage studies of amorphous silicon photodiode sensors for applications in radiotherapy x-ray imaging. *Nucl. Instrum. Meth. A.* (Cited on page 24).

Battistoni, G., Muraro, S., Sala, P., Cerutti, F., Ferrari, A., Roesler, S., Fasso, A., and Ranft, J. (2006). The fluka code: Description and benchmarking. *Proceedings of the Hadronic Shower Simulation Workshop 2006.* (Cited on page 34).

Bethe, H. and Ashkin, J. (1953). *Experimental Nuclear Physics.* (Cited on page 4).

Beutel, J. (2000). *Handbook of medical imaging: Physics and psychophysics.* (Cited on page 39).

Bichsel, H., Hiraoka, T., and Omata, K. (2000). Aspects of fast-ion dosimetry. *Radiation Research 153, 208-219.* (Cited on page 11).

Boone, J. and Seibert, J. (1994). An analytical edge spread function model for computer fitting and subsequent calculation of the lsf and mtf. *Med. Phys.* (Cited on page 27).

Bragg, W. H. and Kleeman, R. (1905). *Philos. Mag., 10,318.* (Cited on page 4).

Buhr, E. et al. (2003). Accuracy of a simple method for deriving the presampled modulation transfer function of a digital radiographic system from an edge image. *Med. Phys.* (Cited on page 27).

Butts, J. J. and Katz, R. (1967). Theory of rbe for heavy ion bombardment of dry enzymes and viruses. *Radiation research, 30.* (Cited on pages 51 and 89).

Cormack, A. M. and Koehler, A. M. (1976). Quantitative proton tomography: preliminary experiments. *Phys. Med. Biol. 21.* (Cited on page 12).

Crowe, K. M., Budinger, T. F., Cahoon, J. L., Elischer, V. P., Huesman, R. H., and Kanstein, L. L. (1975). Axial scanning with 900 mev alpha particles. *IEEE Trans. Nucl. Sci. 22.* (Cited on page 12).

Deasy, J. (1994). Icru report 49, stopping powers and ranges for protons and alpha particles. *Medical Physics, Volume 21, Issue 5.* (Cited on page 53).

Depauw, N. and Seco, J. (2011). Sensitivity study of proton radiography and comparison with kv and mv x-ray imaging using geant4 monte carlo simulations. *Phys. Med. Biol. 56.* (Cited on page 13).

Donetti, M. et al. (2006). A method for the inter-calibration of a matrix of sensors. *Phys.Med.Biol. 51 (3).* (Cited on page 40).

Elsaesser, T. and Scholz, M. (2007). Cluster effects within the local effect model. (Cited on page 5).

Engelke, J. (2009). Analysis of computed tomography imaging with respect to heavy ion therapy planning. Master's thesis. (Cited on page 2).

Ewert, U. (2002). Upheaval in industrial radiology. *NDT Int.* (Cited on page 22).

Ferrari, A., Sala, P., Fasso, A., and Ranft, J. (2005). Fluka: a multi-particle transport code. (Cited on page 35).

Fujita, H. et al. (1992). A simple method for determining the modulation transfer function in digital radiography. *IEEE Trans. Med. Imaging.* (Cited on page 26).

Gammex (2004). *Electron Density CT Phantom.* (Cited on pages 29 and 30).

Goitein, M. (1972). Three-dimensional density reconstruction from a series of two-dimensional projections. *Nucl. Instrum. Methods 101.* (Cited on pages 11 and 13).

Goldmann, L. W. and Yester, M. V. (2004). Specifications, performance evaluation, and quality assurance of radiographic and fluoroscopic systems in the digital era. *Medical Physics Publishing, 153:175.* (Cited on page 25).

Greer, P. (2005). Correction of pixel sensitivity variation and off-axis response for amorphous silicon epid dosimetry. *Med.Phys. 32*. (Cited on page 40).

Gross, K. and Pavlovic, M. (1998). Proposal for a dedicated ion-beam facility for cancer therapy. *Joint Proposal of University of Heidelberg, German cancer research centre and GSI Darmstadt*. (Cited on page 18).

Haberer, T. et al. (2004). The heidelberg ion therapy center. *Radiother. Oncol.* (Cited on page 17).

Haettner, E., Iwase, H., and Schardt, D. (2006). Experimental fragmentation studies with ^{12}c therapy beams. *Rad. Prot. Dos. 122, 485*. (Cited on page 11).

Han, B., Xu, X. G., and Chen, G. T. Y. (2011). Proton radiography and fluoroscopy of lung tumors: A monte carlo study using patient-specific 4dct phantoms. *Med. Phys. 38 (4)*. (Cited on page 13).

Hanson, K. M., Bradbury, J. N., Cannon, T. M., Hutson, R. L., Laubacher, D. B., Macek, R., Paciotti, M. A., and Taylor, C. A. (1978). The applications of protons to computed tomography. *IEEE Trans. Nucl. Sci. 25*. (Cited on page 13).

Hanson, K. M., Bradbury, J. N., Cannon, T. M., Hutson, R. L., Laubacher, D. B., Macek, R., Paciotti, M. A., and Taylor, C. A. (1982). Computed tomography using proton energy loss. *Phys. Med. Biol. 27*. (Cited on page 13).

Hartmann, B. (2010). Quality assurance in ion beam therapy: Investigation towards new detectors. Master's thesis. (Cited on pages 18 and 99).

Hartmann, B., Telsemeyer, J., Huber, L., Ackermann, B., Jäkel, O., and Martišíková, M. (2012). Investigations of a flat-panel detector for quality assurance measurements in ion beam therapy. *Phys. Med. Biol. 57 51*. (Cited on pages 37, 59, 89, 90, and 99).

Heimann, E. (1998). *Radiation Image Detector RID 256-L*. (Cited on page 23).

Heyes, G. and Mill, A. (2004). The neoplastic transformation potential of mammography x rays and atomic bomb spectrum radiation. *Radiation research, 162:120-7*. (Cited on page 70).

Heyes, G., Mill, A., and Charles, M. (2009). Mammography- oncogenecity at low dose. *J. Radiol. Prot. 29 A123-A132*. (Cited on page 70).

Highland, V. (1975). Some practical remarks on multiple scattering. *Nucl. Instrum. Methods 129*. (Cited on page 9).

Horn, J. (2011). Charakterisierung eines halbleiterdetektors und implementierung in die qualitätssicherung der ionenstrahl-therapie. Master's thesis. (Cited on pages 89, 90, and 103).

Huber, L. (2011). Patient position verification in ion beam therapy using silicon detectors and ion beams. Master's thesis. (Cited on pages 17, 26, 36, and 57).

Huenemohr, N. (2011). Improvement of ion therapy planning by the use of dual energy computed tomography. Master's thesis. (Cited on page 31).

Jacob, C. (1997). Reichweite CT-Zahl Beziehung von Phantommaterialien und Messungen mit einer neuentwickelten multisegmentierten Ionisationskammer zur Dosisverifikation bei Schwerionenbestrahlung. PhD thesis, Ruperto-Carola University of Heidelberg. (Cited on page 8).

Jäkel, O. et al. (2001). Relation between carbon ion ranges and x-ray CT numbers. *Med.Phys.28.* (Cited on pages 1, 30, and 97).

Jäkel, O. and Reiss, P. (2007). The influence of metal artefacts on the range of ion beams. *Phys.Med.Biol.* (Cited on page 1).

Jakubek, J., Granja, C., Hartmann, B., Martišíková, M., Jäkel, O., and Opalka, L. (2011). Imaging with scattered or secondary radiation in hadron therapy beams with the 3d sensitive voxel detector. *IEEE MIC Abstract Book.* (Cited on page 104).

Kagadis, G. and Langer, S. (2011). *Imaging in Medical Disgnosis and therapy: Informatics in Medical Imaging.* (Cited on pages 95 and 103).

Kalender, W. (2000). *Computed Tomography.* (Cited on page 34).

Karg, J., Speer, S., Schmidt, M., and Mueller, R. (2010). The monte carlo code mcptv-monte carlo dose calculation in radiation therapy with carbon ions. *Phys. Med. Biol. 55 3917-3936.* (Cited on page 10).

Karger, C. P., Jäkel, O., Palmans, H., and Kanai, T. (2010). Dosimetry for ion beam radiotherapy. *Phys. Med. Biol. 55 (21).* (Cited on pages 96 and 100).

Kasap, S. and Rowlands, J. A. (2002). Direct-conversion flat-panel x-ray image detectors. *IEE Proc.-Circuits Devices Syst., Vol 149, No. 2.* (Cited on page 39).

Kim, J.-M., Kim, H., Cheong, M., Cho, M., Shon, C.-S., and Hwy Lim, C. (2006). Investigation of scintillation screens for x-ray imaging. *Key Engineering Materials Vols. 321-323 pp 1056-1059.* (Cited on page 37).

Koehler, A. M., Schneider, R. J., and Sisterson, J. M. (1975). Range modulation for proton and heavy ions. *Nucl. Instrum. Methods 131.* (Cited on page 13).

Köhler, A. (1968). Proton radiography. *Science, 160:303 304.* (Cited on page 11).

Köhler, A. et al. (1965). Range of protons in human skullbone. *Radiat. Res.* (Cited on page 8).

Körner, M. et al. (2007). Advances in digital radiography: Physical principles and system overview. *RadioGraphics.* (Cited on page 22).

Krämer, M. et al. (2000). Treatment planning for heavy-ion radiotherapy: physical beam model and dose optimization. *Phys.Med.Biol.45.* (Cited on pages 7, 20, and 38).

Kuo, Y. (2004). *Thin Film Transistors, Materials and Processes, Volume1: Amorphous silicon thin film transistors.* (Cited on page 23).

Lazarev, V. et al. (2011). Technical overview of the siemens particle therapy accelerator. *Proceedings of IPAC 2011.* (Cited on page 18).

Leo, W. R. (1994). *Techniques for nuclear and particle physics experiments: a how-to approach.* (Cited on page 6).

Llopart, X., Ballabriga, R., Campbell, M., Tlustos, L., and Wong, W. (2007). Timepix, a 65k programmable pixel readout chip for arrival time, energy and/or photon counting measurements. *NIM A 581, 485-494.* (Cited on page 103).

Mairani, A. (2007). PhD thesis, Ruperto-Carola University of Heidelberg. (Cited on page 11).

Marshall, N. et al. (2011). Image quality assessment in digital mammography: parti. technical characterization of the systems. *Phys.Med.Biol. 56.* (Cited on page 93).

Martišíková, M. (2010). Two-dimensional fluence measurements for ion beam plan verification. *PTCOG 50, abstract book, p. 1.* (Cited on pages 24, 89, and 99).

Martišíková, M., Brons, S., Hesse, B., and Jäkel, O. (2012a). Patient plan verifications in carbon ion beam therapy by 2d fluence measurements. *to be published.* (Cited on pages 33 and 37).

Martišíková, M. et al. (2011). Test of an amorphous silicon detector in medical proton beams. *Nucl. Instrum. Meth. A.* (Cited on pages 24 and 37).

Martišíková, M., Hartmann, B., Hesse, B., Brons, S., Ackermann, B., and Jäkel, O. (2012b). Characterization of a flat-panel detector for ion beam spot measurements. *Phys. Med. Bio. 57 485-497.* (Cited on pages 25, 37, 89, and 91).

Medipix (2012). (Cited on page 103).

Mestres, M., Cabalin, M., Barrios, L., Ribas, M., and Barquinero, J. (2008). Rbe of x-rays of different energies: A cytogenetic evaluation by fish. *Radiation Research 170 (1)*. (Cited on page 70).

Mevion (2011). Compact superconducting synchrocyclotron. (Cited on page 95).

Molière, G. (1947). Theorie der streuung schneller geladener teilchen i und ii. *Z. Naturforschung 2a and 3a*. (Cited on page 9).

Mumot, M., Algranati, C., Hartmann, M., Schippers, J. M., Hug, E., and Lomax, A. J. (2010). Proton range verification using a range probe: definition of concept and initial analysis. *Phys. Med. Biol. 55*. (Cited on page 12).

Muraishi, H., Nishimura, K., Abe, S., Satoh, H., Hara, S., Hara, H., Takahasi, Y., Mogaki, T., Kawai, R., Yokoyama, K., Yasuda, N., Tomida, T., Ohno, Y., and Kanai, T. (2009). Evaluation of spatial resolution for heavy ion ct system based on the measurements of residual range distribution with himac. *IEEE Transaction on Nuclear Science 56 (5)*. (Cited on pages 2, 15, and 93).

Murashi, H. (2011). personal communication. *IEEE Nuclear Science Symposium MIC Poster Presentation*. (Cited on page 14).

Murashi, H., Nishimura, K., Abe, S., Satoh, H., Takahashi, Y., Hara, S., Kawai, R., Yokoyama, K., Yasuda, N., Tomida, T., Ohno, Y., and Kanai, T. (2007). Heavy ion ct system based on the measurement of residual range distribution: Improvement of the optical detector system. *IEEE Nuclear Science Symposium Conference Record*. (Cited on pages 14, 32, and 97).

Nishimura, K., Satoh, H., Inada, T., Abe, S., Futami, Y., Matsufuji, N., Higashi, A., Kekeno, M., and Tazawa, S. (1999). Heavy ion ct by measuring residual range distribution. *NIRS-M (Natl Inst Radiol Sci), No. 133*. (Cited on page 13).

Ohno, Y., Kohno, T., Matsufuji, N., and Kanai, T. (2004). Measurement of electron density distribution using heavy ion ct. *Nuclear Instruments and Methods in Physics Research A 525*. (Cited on pages 2, 14, and 15).

Paganetti, H. et al. (2002). Relative biological effectiveness (rbe) values for proton beam therapy. *Int. J. Radiation Oncology Biol. Phys. 53 (2)*. (Cited on page 70).

Partridge, M., Hesse, B., and Müller, L. (2002). A performance comparison of direct- and indirect-detection flat-panel imagers. *Nucl. Instrum. Meth. A 484 351-363*. (Cited on pages 2, 23, 25, and 91).

Penfold, S. N., Schulte, R. W., Censor, Y., and Rosenfeld, A. B. (2010). Total variation superiorization schemes in proton computed tomography image reconstruction. *Med. Phys. 37 (11)*. (Cited on page 13).

Poole, B., Blackfield, D., and Nelson, S. (2007). Particle simulations of a linear dielectric wall proton accelerator. *2007 Particle Accelerator Conference*. (Cited on page 95).

Rinaldi, I. (2012). *Investigation of novel imaging methods using therapeutic ion beams*. PhD thesis, Ruperto-Carola University of Heidelberg. (Cited on pages 2, 14, and 15).

Ryu, H., Song, E., and Lee, J. (2008). Density and spatial resolutions of proton radiography using a range modulation technique. *Phys.Med.Biol. 53*. (Cited on pages 2 and 15).

Sadrozinski, H. F.-W., Bashirov, V., Colby, B., Coutrakon, G., Erdelyi, B., Fusi, D., Hurley, F., Johnson, R. P., Kashiguine, S., McAllister, S., Martinez-McKinney, F., Missaghian, J., Scaringella, M., Penfold, S., Rykalin, V., Schulte, S., Schubert, K., Steinberg, D., and Zatserklaniy, A. (2011). Detector development for proton computed tomography. *IEEE Nuclear Science Symposium*. (Cited on page 15).

Sadrozinski, H.-W. et al. (2003). Issues in proton computed tomography. *Nuclear Instruments and Methods in Physics research A 511*. (Cited on pages 2 and 15).

Schneider, U., Besserer, J., and Pemler, P. (2004). First proton radiography of an animal patient. *Med.Phys. 31 (5)*. (Cited on pages 3 and 13).

Schneider, U. et al. (1996). The calibration of ct hounsfield units for radiotherapy treatment planning. *Physics in Medicine and Biology*. (Cited on pages 1 and 20).

Schneider, U. and Pedroni, E. (1995). Proton radiography as a tool for quality control in proton therapy. *Med.Phys. 22 (4)*. (Cited on pages 10, 12, and 46).

Schulte, R., Bshkirov, V., Klock, M. C. L., Li, T., Wroe, A. J., Evseev, I., Williams, D. C., and Satogat, T. (2005). Density resolution of proton computed tomography. *Med.Phys. 32(4)*. (Cited on page 13).

Seco, J. and Depauw, N. (2011). Proof of principle study of the use of a cmos active pixel sensor for proton radiography. *Med.Phys. 38(2)*. (Cited on page 15).

Shinoda, H., Kanai, T., and Kohno, T. (2006). Application of heavy-ion ct. *Phys. Med. Biol. 51*. (Cited on page 14).

Shrimpton, P., Billier, M., Lewis, M., and Dunn, M. (2003). Doses from computed tomography (ct) examinations in the uk- 2003 review. (Cited on pages 93 and 96).

Sigmund, P. (2005). Icru report 73, stopping of ions heavier than helium. *Journal of the ICRU, Vol. 5 No. 1.* (Cited on page 53).

Sokup, P., Jakubek, J., and Vykydal, Z. (2011). 3d sensitive voxel detector of ionizing radiation based on timepix device. *Journal of Instrumentation 6, C01060.* (Cited on page 104).

Sommer, F. et al. (1978). Heavy-ion radiography: Density resolution and specimen radiography. *Investigative Radiology Vol.13 No.2.* (Cited on pages 2 and 12).

Sommerer, F., Parodi, K., Ferrari, A., Poljanic, K., Enghardt, W., and Aiginger, H. (2006). Investigating the accuracy of the fluka code for transport of therapeutic ion beams in matter. *Phys.Med.Biol. 51 (17).* (Cited on page 35).

Steward, V. W. and Koehler, A. M. (1972). Proton radiography as a diagnostic tool. *AAPM Winter Meeting, AAPM Bulletin 6, no.4, 194.* (Cited on page 11).

Tao, S., Karim, K., Servati, P., Lee, C.-H., and Nathan, A. (2003). Large area digital x-ray imaging. *Sensors Update, Volume 12, Issue 1, pages 3-49.* (Cited on page 37).

Tick, T. and Campbell, M. (2011). Tsv processing of medipix3 wafers by cea-leti: a progress report. *Topical Workshop on Electronics for Particle Physics 2011.* (Cited on page 104).

Tobias, C. et al. (1980). Biological and medical with accelerated heavy ions at the bevelac. *Report LBL.* (Cited on page 8).

Tripathi, R. et al. (1997). *NASA Technical Paper 3621.* (Cited on page 10).

Tubiana, M., Dutreix, J., and Vambersie, A. (1920). *Introduction to radiobiology.* (Cited on page 5).

Urie, M., Goitein, M., Holley, W., and Chen, G. (1986). Degradation of the bragg peak due to inhomogeneities. *Phys. Med. Biol. 31 1-15.* (Cited on pages 9 and 10).

Vykydal, Z., Jakubek, J., Holy, T., and Pospisil, S. (2005). A portable pixel detector operating as an active nuclear emulsion and its application for x-ray and neutron tomography. *Proceeding of the 9th ICATPP Conference.* (Cited on page 103).

Williams, T. (1999). *The Optical Transfer Function of Imaging Systems.* (Cited on page 41).

Wilson, R. R. (1946). Radiological use of fast protons. *Radiology, 47: 487-491.* (Cited on pages 2 and 11).

Ziegler, J. (1999). Stopping of energetic light ions in elemental matter. *Journal of Applied Physics*. (Cited on page 4).

Zygmanski, P., Gall, K. P., Rabin, M. S. Z., and Rosenthal, S. J. (2000). The measurement of proton stopping power using proton-cone-beam computed tomography. *Phys. Med. Biol. 45*. (Cited on pages 13 and 32).